Ultra-High-Q Planar Microcavities and Applications

Thesis by

Deniz Armani

In Partial Fulfillment of the Requirements for the

Degree of

Doctor of Philosophy

CALIFORNIA INSTITUTE OF TECHNOLOGY

Pasadena, California

2005

(Defended May 6, 2005)

© 2005

Deniz K. Armani

All Rights Reserved

To My Mom& Dad, Prof. Vahala, Andrea and the Two Monkeys

Acknowledgement

In hindsight, it may seem as though the road that I took to reach the point where I am was a series of well timed and perfectly executed maneuvers. Having been through it, I can tell you that this is definitely not the case. The truth lies somewhere in a mix of discipline, luck, and hard work, but most importantly the help of a few key people. By "help" I don't necessarily mean to suggest something simple, such as help in class or financial aid. Instead I was given help that was much more profound and truly life-changing. There are a handful of people who deserve my utmost thanks for this "help" and for making my tenure as a graduate student at Caltech a time that I will remember as the most fun I will probably ever have.

First, to all my group members:

> Sean, I thank you for your diligence and patience, you have a tremendous mind and intense focus, I learned a great deal from you.
>
> Tobias, your love of UHQ microcavities is contagious, without your vigor the microtoroid would have had a difficult childhood.
>
> Bumki, you're a research machine, if you weren't doing a computer simulation you were working in the cleanroom. Your diligence and brilliance are admirable.
>
> Lan, thank you for teaching me about sol-gel and all of its application. I will remember my lessons for my entire career.
>
> Hossein, thanks for all the laughs.

For Jersey the cat and Corky the dog, I say thank you for the comic relief and the face licks.

To my Mom and Dad and I would like to say thank you. Two people who have made such a profound impact on my life that the only way that I could do justice conveying their parental skill is by writing a very, very long book. Suffice it to say that they sacrificed a great deal to make sure that I was always in an environment in which I could achieve well beyond my potential. More importantly though I have to thank them for instilling within me the thrill of learning and the love of science from a young age that still drive me to this very moment. Lastly, they taught me via their own actions that courage, honor, virtue and honesty are the most important things in life, without holding true to those ideals anything I may achieve in my life is meaningless.

My deepest gratitude to my Grandfather Col. M. Emin Varol and Grandmother Ruhiye Varol, I will never forget your steady guidance, wisdom and support and for teaching me what the truly important things in life are.

To the best uncle ever, Sertac Varol, thank you for having me apply to the U of I, without your insistence this whole journey would have never begun.

To Andrea Martin. My soul-mate and the best research partner I have ever had. Thank you for teaching me the benefits of patience, discipline, hard work and true love. You are the light of my life.

Professor Kerry Vahala, a truly remarkable research advisor and mentor and above all a fair person. Only with the help of his theoretical and experimental insights did I finally begin to learn how to see forest through the trees. I can honestly say that I did

not know how lucky I was to be accepted to his group 5-years ago, but I quickly realized what a unique and elite group I had the fortune of working with shortly thereafter. Never once did he act like my boss nor did he ever treat me like an employee. He never looked over my shoulder to make sure I was working, yet he was always only one door away whenever I needed advice (experimental or otherwise). I always knew that he recognized and appreciated my hard work and he rewarded it accordingly with more responsibility and flexibility. Likewise, when I did not perform well or made a mistake he always sat down with me and provided feedback rather than simply admonishing me.

Professsor Oskar Painter, I was truly fortunate to have your experimental and theoretical advice, I appreciated and deeply valued every moment of our discussions. I will always envy you for your amazing grasp of theory and device fabrication. More importantly you have been a valued friend, I thank you for the friendship you extended to me.

To Prof. Yaser Abu-Mostafa, I will never be able to thank you enough for allowing me to work in your lab while I was in high school. The opportunity you granted me and the value of the experience that I received is difficult to put into words, nonetheless, thank you for everything.

Last, but not least, I would like to extend my deepest gratitude to my Uncle Kadri Vural, also a fellow Caltech Ph.D. He was always there to remind me of his cardinal rule of graduate school: “Finish as fast as you can!”. Moreover, he has always steadfastly supported my goals and aspirations and has been an extremely loyal friend to myself and my family through good times and bad.

In closing, when I started at Caltech I did not truly understand the significance of a doctoral degree. I knew that it was meant to signify a demonstrated level of competence and skill of being able to work without constant supervision, however after being under Prof. Vahala's tutelage and with the support my Parents and Andrea I realize that there is much more to the degree. I can now say with confidence that I have learned how to be an effective researcher, a reliable collaborator, a skilled experimentalist, a project manager, but most importantly, I have become a scientist.

Abstract

Ultra-high-Q (UHQ) silica microspheres have found research applications in diverse fields ranging from telecommunications to nonlinear optics to biological and chemical sensing. However, despite having quality factors greater than 10^8, the silica microsphere has not moved to an industrial setting because of several major drawbacks. The most hindering is the manual fabrication technique used that makes tight process control difficult and integration with other optical or electrical components impossible. Despite the strong desire to fabricate an integrated UHQ microresonator on a planar substrate, the highest quality factor achieved for any micro-fabricated planar micro-cavity (at the time of my first publication) was over 4 orders of magnitude lower than for silica microspheres. In this thesis, a process for creating planar micro-cavities with Q factors in excess of 400 million on silicon wafers is demonstrated. The advantage of these planar ultra-high-Q (UHQ) microtoroid resonators is that they successfully overcome the previously mentioned drawbacks of silica microsphere resonators while maintaining nearly identical, if not better, performance characteristics. Additionally, due to the planar nature of these new devices, functionality has been integrated in-situ while maintaining coupling control, and low-threshold lasing.

Table of Contents

Acknowledgement .... **iv**
Abstract .... **viii**
Table of Contents .... **ix**
Table of Figures .... **x**
Chapter 1 – Introduction **1**
  1.1 Why Are Integrated Ultra-High-Q Microresonators Necessary? 1
  1.2 Why Is Ultra-High-Q On-A-Chip Necessary? 2
  1.3 Roadmap to This Thesis 3
Chapter 2 - Planar Microtoroid Resonators **4**
  2.1 Fabrication 4
    2.1.1 Bulk Silicon Etchants 5
    2.1.2 Laser Activated Reflow 7
  2.2 Characterization of the Microtoroid 8
  2.3 Characterization of the Microdisk 11
  2.4 Raman Lasing 12
  2.5 Conclusion 12
Chapter 3 - Electrical Thermooptic Tuning of Microtoroid Resonators **26**
  3.1 Introduction 26
  3.2 Fabrication 27
  3.3 Characterization 29
  3.4 Conclusion 31
Chapter 4 - Microtoroid Resonator with Integrated MEMS Positioner **40**
  4.1 Introduction 40
  4.2 Fabrication 41
  4.3 Device Release 47
  4.4 Device Control and Characterization 48
  4.5 Conclusion and Outlook 50
Chapter 5 - Replica Molded Polymer Microtoroid Resonators **63**
  5.1 Introduction 63
  5.2 Fabrication 63
  5.3 Characterization 65
  5.4 Conclusion 68
Chapter 6 - Surface Functionalization of Microtoroid Resonators with Erbium-Doped Sol-Gel **77**
  6.1 Introduction 77
  6.2 Fabrication 77
  6.3 Characterization 79
  6.4 Conclusion 80
Chapter 7 - Outlook **85**
Bibliography **86**
Vita **94**

Table of Figures

Figure 2-1: Four step fabrication flow of the microtoroid resonators. A: Photolithographically define photoresist disks. 14

Figure 2-2: A scanning electron micrograph of a microtoroid resonator undercut using EDP as the silicon etchant: note the non-circular shaped pillar and irregular toroid. 15

Figure 2-3: A schematic diagram of the xenon difluoride etch system (top). A picture of the actual system in the Vahala lab cleanroom (bottom). 16

Figure 2-4: CO_2 laser system for the microtoroid reflow process. The sample is imaged simultaneously while the laser activated reflow process takes place. 17

Figure 2-5: A scanning electron-micrograph of the microtoroid resonator. Inset: A scanning electron-micrograph of the microdisk resonator (prior to the reflow process). 18

Figure 2-6: Transmission spectra of a toroidal resonator. The free spectral range (defined as the wavelength spacing between modes with successive angular mode number) is 5.65-nm, which corresponds to a torus approximately 94-μm in diameter. The inset shows what we believe to be the two lowest-order radial modes (based on modeling of a microdisk resonator). Additional subsidiary peaks are attributed to other radial or azimuthal modes. 19

Figure 2-7: Ringdown measurement of a 90-micron-diameter toroid microcavity at the critical-coupling point. The measured lifetime of τ_{crit}=43 ns corresponds to an intrinsic quality factor of Q=1.25×10^8. 20

Figure 2-8: SEM micrograph of a 120-μm-diameter microdisk resonator (2-μm thick oxide disk). The inset shows an optical micrograph of a resonator coupled to a tapered optical fiber. 21

Figure 2-9: Transmission (normalized with respect to the launched fiber power) and reflection properties versus taper-disk gap distance. The inset shows the transmission versus frequency near the critical point. The off-resonant loss was less than 5%. 22

Figure 2-10: Mode spectrum of a 114-μm-diameter resonator for TE and TM polarizations. The circles and diamonds represent the first- and second-order radial modes, based on modeling. 23

Figure 2-11: Broadband frequency generation in a microtoroid. 24

Figure 2-12: Raman emission spectrum of a toroid microcavity 25

Figure 3-1: Four-step fabrication process flow of the tunable microtoroid resonators. A: Standard photolithography is performed in order to define the oxide disk and contact hole. B: Metal lift-off is performed in order to define the ohmic contact. C: XeF_2 is used to undercut the silica disk. D: CO_2 laser radiation is used to reflow the silica and create the microtoroid. 33

Figure 3-2: Scanning electron-micrograph of the tunable microdisk prior to laser-activated reflow. 34

Figure 3-3: Scanning electron-micrograph of the tunable microtoroid. 35

Figure 3-4: A side-view optical micrograph of the tunable microtoroid resonator during testing. Both the tungsten contact probe and the fiber taper waveguide can clearly be seen. 36

Figure 3-5: A top view optical micrograph of the tunable microtoroid resonator during testing. The aluminum ohmic contact and the fiber taper waveguide can clearly be seen. 37

Figure 3-6: Resonant frequency shift versus voltage^2. The quadratic coefficient is 85.56 GHz/V^2. 38

Figure 3-7: The frequency response of the tunable microtoroid resonators in both air and helium ambient atmospheres. Inset: A rendered depiction of the tunable microtoroid device coupled to a tapered optical fiber while being contacted by a metal probe. 39

Figure 4-1: The first two masks used in the fabrication of the MEMS devices. Mask 1 is used to define and isolate the electrical contact area as well as define the silica disk and alignment mark. Mask 2 is used to define the sacrificial PR layer upon which the nickel is later electroplated. 52

Figure 4-2: These are the three process steps associated with the first mask. A: The oxide wafer is degreased. B: PR is spin coated and patterned. C: The silica is patterned and the PR removed. 53

Figure 4-3: These are the two process steps associated with the second mask. A: The thick PR layer is spin coated and patterned; this layer will act as a sacrificial layer during later processing. B: A thin layer of chrome and gold are evaporated across the entire wafer; the metal will be used as the seed layer during electroplating. 54

Figure 4-4: These are the three process steps associated with the third mask. A: The final PR layer is spin coated and patterned; this layer is used as a mold during

the nickel electroplating process. B: The PR mold is carefully removed using acetone and DI water. C: The exposed regions of the chrome/gold seed layer are removed, the sacrificial PR layer is rinsed away, and the entire chip is etched using XeF_2 in order to release the micropositioning arm. 55

Figure 4-5: A schematic representation of the nickel electroplating setup. 56

Figure 4-6: The nickel electroplating setup currently used in the Vahala cleanroom. 57

Figure 4-7: A compound optical micrograph taken from the top view of the MEMS device. The serpentine arms are used as a heating element to tune the disk as well as a mechanical stabilizer ensuring that movement is horizontally restricted. The center fork is used to move the disk, to which the disk is attached by a single beam. 58

Figure 4-8: Close up top view of the microdisk and MEMS positioning arm. 59

Figure 4-9: Scanning electron-micrograph of the MEMS positioning system. 60

Figure 4-10: Close up of the microdisk; note the stress induced warping of the device. 61

Figure 4-11: Frequency tuning response of the microdisk. The tuning is the result of ohmic heating from the serpentine whiskers attached to the microdisk. 62

Figure 5-1: Replica molding process flow: a) ultra-high-Q microtoroid master array is fabricated and silanated with TCMS to aid in the release of the master from the mold; b) master is coated with PDMS to form PDMS mold, which is subsequently exposed to an oxygen plasma and filled with PDMS/Vicast to

form c) PDMS/Vicast replica polymer microtoroid array. d) Optical micrograph of a PDMS microtoroid. 69

Figure 5-2: Cross-section of the PDMS mold, note the outline of the pillar as well as the toroid ring. 70

Figure 5-3: Scanning electron-micrograph of the first polymer microtoroid replica fabricated from PDMS. 71

Figure 5-4: Side view of a Vicast microtroid replica shown while coupled to a tapered optical fiber. 72

Figure 5-5: Transmission spectrum for a 45-micron diameter Vicast polymer microtoroid. The Free Spectral Range (FSR) of the polymer high Q microtoroid is in agreement with the theoretical prediction of 11.5 nm. 73

Figure 5-6: Intrinsic Q for PDMS (red circles) and for Vicast (purple squares) replicated microresonators measured in 980 nm band; the theoretical Q in PDMS (blue triangles) is also plotted. Data points are connected by curves as a guide to the eye. 74

Figure 5-7: Intrinsic Q for PDMS (red circles) and for Vicast (purple squares) replicated microresonators measured in 1300 nm band, the theoretical Q in PDMS (blue triangles) is also plotted. Data points are connected by curves as a guide to the eye. 75

Figure 5-8: Intrinsic Q for PDMS (red circles) and for Vicast (purple squares) replicated microresonators measured in 1550 nm band, the theoretical Q in PDMS (blue triangles) is also plotted. Data points are connected by curves as a guide to the eye. 76

Figure 6-1: Illustration showing a microchip laser consisting of an 81

Figure 6-2: Emission spectrum of a microtoroid laser with approximate diameter of 80 µm. 82

Figure 6-3: (a) Laser emission spectrum from Er-doped sol-gel thin-film coated microtoroid laser. (b) Reference laser emission spectrum from a 1550 nm single-mode laser with short-term linewidth of 300 kHz. Both spectra were measured using a high finesse scanning Fabry–Perot spectrometer. 83

Figure 6-4: Measured laser output power plotted versus absorbed pump power for a microtoroid laser with a diameter of 80 µm. 84

Chapter 1 – Introduction

1.1 Why Are Integrated Ultra-High-Q Microresonators Necessary?

Re-circulation of light within small dielectric volumes enables the storage of optical power near specific resonant frequencies and is important in a wide range of fields such as cavity quantum electrodynamics[1, 2], photonics[3, 4], nonlinear optics[5-7], and sensing[8, 9]. The performance of these structures is strongly dependent upon the surface quality. With a nearly atomic-scale surface finish, dielectric micro-cavities formed by surface tension are superior to all other micro-resonant structures by many orders of magnitude when comparing photon lifetime (cavity Q). Droplets and solid spheres or spheroids[10-13] (formed from droplets) are so far the only known examples of surface-tension, induced micro-cavities (STIM); in particular, silica based microsphere resonators have attained Q values in excess of 9 billion. Despite their unique properties and successful application in diverse fields, their physical characteristics are not easily controlled during fabrication nor does the fabrication process lend itself to batch methods. Dielectric resonators created as planar disk structures by micro-lithography are preferable to sphere or droplet structures when consistency of Q and integration is necessary. Wafer-based processing[14] of resonators offers a way to both miniaturize and achieve process parallelism and control – all of which are of increased interest in experimental work. Moreover, only through planar fabrication of these devices can additional functionality be integrated into or along-side these devices.

1.2 Why Is Ultra-High-Q On-A-Chip Necessary?

The best Q factor achieved for any micro-fabricated planar micro-cavity (at the time of publication of our work) was over 4 orders of magnitude lower[15] than for STIMs. Here, we demonstrate a process for creating planar micro-cavities with Q factors in excess of 400 million on silicon wafers. In addition to providing an ultra-high-Q cavity that avoids the objectionable properties of droplets and spheres, this process introduces wafer-scale control and parallelism to fabrication of ultra-high-Q (UHQ) micro-cavities.

This was achieved by successfully combining the beneficial aspects of two distinct microresonator classes, the ultra-low material loss of silica and the minimal scattering loss of microspheres while maintaining the ability to produce the devices in an integrated manner. Aside from the numerous advantages now available to laboratory based experiments, by successfully merging the beneficial aspects of these two distinct classes of resonators, it is now possible for the first time to think of moving UHQ optical resonators into real-world applications. More importantly, the number of potential applications for UHQ devices will increase now that it is possible to envision fully integrated systems-on-a-chip. Lastly, as will be discussed later in this thesis, additional functionality will be pursued in order to integrate active frequency and positioning in-situ via a MEMS based system.

1.3 Roadmap to This Thesis

The flow of this thesis is as follows. In Chapter 2 the development, fabrication and characterization of the microtoroid resonator is explained. This chapter also covers the Q measurement of silica microdisk resonators and concludes with a discussion about one non-linear optics application, stimulated Raman lasing, that was observed in the UHQ microtoroid resonators. In Chapter 3, the integration of resonant frequency tuning into the microtoroid and the fabrication outline is discussed; both tuning rate and the frequency response are also reported. Chapter 4 covers recent developments that have been made towards the integration of MEMS based on chip micropositioning using the microdisk resonators. Chapters 5 and 6 respectively cover work performed on fabricating polymer replica microtoroids and erbium-doped sol-gel coated microlasers on-a-chip. The thesis is concluded in Chapter 7 with a brief summary and outlook towards future developments.

Chapter 2 - Planar Microtoroid Resonators

2.1 Fabrication

The devices were fabricated using a silicon wafer with a 2-micron layer of thermally grown silicon dioxide (SiO_2). The silicon\silica material system was specifically chosen for two reasons. The primary reason was the low optical absorption of silica in the visible and near-infra-red (IR) wavelengths. Secondly, thermally grown silica is of much higher quality than oxides deposited using lower temperature chemical vapor deposition processes; namely there fewer hydroxide molecules (which strongly absorb in the 1550-nm band)[16]. The fabrication process flow of the microtoroid resonators (Figure 2-1) is simply composed of four steps: photolithography, pattern transfer into the silicon dioxide layer, selective gas etch of the exposed silicon, and selective reflow of the patterned silica.

The process details are as follows. First, photolithography is performed to create disk-shaped photo-resist (PR) pads (160 microns in diameter) on a <100> prime grade silicon substrate with 2-microns of thermally grown oxide. The wafers are first thoroughly degreased using acetone, isopropyl alcohol (IPA), and deionized (DI) water, and next blow dried with nitrogen, and then baked for two minutes at 130°C in order to dehydrate the surface. After the wafers are allowed to cool for two minutes, they are placed into a chamber with liquid hexamethyldisilizane (HMDS) for two minutes, which allows a layer of only a few molecules to condense on the surface of the substrate. The HMDS is used

as an adhesion promoter between the subsequent PR coating and the silicon wafer surface. The wafer is then removed from the HMDS coating chamber and placed directly on the PR spin coater. The wafer is partially coated with Shipley 1813 PR, and spun at 2000 rpm for 1 minute, and then baked at 90°C in order to harden the PR by evaporating off the solvent. Next, using a MJB-3 Karl-Suss mask aligner, the wafers were exposed to UV light through a light-field mask that contains an array of circles (150-micron diameter circles were the first to be made). The wafer is then immersed in MIF-319 developer for approximately 30 seconds, rinsed with DI water, and blow dried with nitrogen. Following the development procedure an additional bake at 115°C for 1 minute is used in order to further harden the PR and reflow the edges in the process. This reflow step successfully smoothes out micron scale roughness along the edge of the PR pads, further improving the overall resolution of the lithographic process. The circular PR disks now act as an etch mask during immersion in buffered HF acid solution at room temperature. Once the exposed silica is etched, acetone is used to remove residual PR and organic contamination. The remaining SiO_2 disks now act as etch masks during exposure to XeF_2 gas at 3 Torr. XeF_2 was specifically chosen for the purpose of isotropic selective removal of silicon[17, 18].

2.1.1 Bulk Silicon Etchants

It should be noted that other liquid silicon etchants were first used before XeF_2 was finally selected. Initially both KOH[19] and EDP[20] were used to undercut the silica disks. Both of these etchants are anisotropic and therefore non-circular shaped pillars

resulted when <100> oriented silicon wafers were used. KOH also had the additional drawback of rapidly etching silica at the rate of 50 nanometers per hour, therefore it was not used. Although EDP was initially exclusively used in the preparation of the microtoroid resonators, it quickly became apparent that an isotropic etchant was necessary. The non-circular shaped pillars resulted in non-circular microtoroid after the laser induced reflow process and as a result limited the Q factors to the low millions, Figure 2-2. While this was a significant improvement over previous work, by simply changing to an isotropic etchant, it was theorized that the quality factor could be improved even further. Based on the results of the anisotropic etchants, two isotropic silicon etching techniques were evaluated, HNA (liquid etchant) and XeF_2 (gas). HNA could not be used because it etches silica[21] and, as a result, XeF_2 was investigated. XeF_2 etching is performed via a pulsed process in which solid XeF_2 crystals are allowed to sublime to a pressure of 3 Torr inside an evacuated chamber (Figure 2-3). Once the pressure inside the chamber reaches 3 Torr, the XeF_2 gas is allowed to enter a chamber containing the samples to be etched. Each etch pulse removes approximately 1-2 microns of silicon both vertically and laterally. The gas is allowed to etch the silicon samples for approximately 2-minutes at which point the chamber containing the samples is evacuated again. This process is repeated until the pre-determined amount of silicon is etched. Once etching is finished, the edges of the SiO_2 disks are equally undercut leaving circular silicon pillars supporting larger SiO_2 disks. As the optical trajectories of interest reside at the periphery of the silica disk, the removal of the higher index silicon below a portion of the periphery is required to inhibit power leakage into the substrate.

2.1.2 Laser Activated Reflow

The process flow as described thus far leaves lithographic blemishes, visible in an optical microscope, at the disk periphery. These blemishes are what have limited the quality factors of previous planar resonator structures. Therefore an additional processing step was pursued to achieve the surface finish characteristic of STIM structures (rms roughness of several nanometers or less)[13].

A processing step is introduced to selectively heat and reflow the undercut SiO_2 disks without affecting the underlying silicon support pillar. An undercut SiO_2 disk is surface-normal-irradiated using a CO_2 laser (10.6-micron wavelength), similar to techniques proposed for integrated circuit planarization[22] (Figure 2-4). The beam intensity profile follows an approximate Gaussian distribution and is focused to a circular spot approximately 200 microns in diameter. The resulting beam intensity can be varied by electronic control of the laser power, but is typically 100 MW/m^2 during reflow. Due to the strong temperature dependence of the silica optical extinction coefficient near 10.6 microns[23] as well as the thermal isolation of the undercut SiO_2 disk, melting of the disk occurs along the periphery, and not over the silicon pillar. In addition to having a far weaker optical absorption at 10.6 microns, silicon is 100 times more thermally conductive than silica[23, 24]. The silicon pillar therefore remains significantly cooler and physically unaffected throughout the silica reflow process, serving as a heat sink to the selectively absorbed optical power in the silica layer. As the disk diameter shrinks, the effective cross-section available to absorb laser power decreases and shrinkage is

observed to terminate when a toroid-like silica structure has formed. Beyond this point, continued laser treatment at the same intensity results in no observable change of the structure. The process is therefore self-quenching with the final diameter of the molten disk rim controlled by lithography and chemical etch steps. It should be noted that it is possible to interrupt the reflow prior to quenching thereby producing a toroid with a diameter intermediate to the initial disk diameter and terminal diameter.

To summarize this process step, surface tension both smoothes the surface and collapses the silica disk to a toroid shape with self-limiting dimensions defined by the support pillar and the initial thickness of the silica layer. Micrographs showing disks both before and after the laser-activated selective reflow process are shown in Figure 2-5. In these micrographs, the overall disk diameter was reduced to 120-microns as silica was consumed to form a 7-micron thick toroid-shaped perimeter.

2.2 Characterization of the Microtoroid

The mode structure and quality factor of the toroidal cavities were characterized in the optical telecommunication band (1500-nm wavelength band). Tapered optical fibers connected to a single-mode, tunable, external-cavity laser were used to efficiently excite whispering gallery modes of the resonators. Tapered waveguides were positioned on a 20-nm resolution stage and could be moved freely over the silicon sample to individually couple to each of the toroid-shaped microresonators. Dual microscopes were used to simultaneously image disk resonators and fiber tapers from the side and the top. Proper alignment required the taper axis to reside in the equatorial plane of the toroidal cavity with minimal tilt angle. Briefly, optical tapered fibers are fabricated by stretching a

standard optical fiber (SMF-28) while simultaneously heating it using a hydrogen flame[25]. By observing the adiabatic condition, the tapered fibers exhibit low fiber-to-fiber insertion loss (typically <10%). Taper waist diameters are typically several microns, adjusted to properly phase-match to the resonator. Critical coupling[26] (the resonant transfer of all optical waveguide power into the resonator) was achieved by appropriately adjusting the taper-resonator gap. Non-resonant loss was observed to be low (<5%).

Figure 2-6 shows the transmission spectra through a taper in close proximity (on the order of hundreds of nanometers) to a 94-micron-diameter toroidal microresonator. The observed free spectral range corresponds to the equatorial mode number (l-index). Inspection of the data shows that the resonator supports very few radial and azimuthal (m-index or transverse) modes. This is in contrast to spheres, which support (2l+1) azimuthal modes. The quality factor or Q of the resonators was measured in two ways. First, the full-width half-maximum of the Lorentzian-shaped resonance in the undercoupled regime was directly measured by scanning a single-mode laser (short-term linewidth about 300 kHz) through a resonance. Low input power levels (typically less than 5 microwatts) were used to avoid thermally-induced distortion of the line shape due to resonant-field buildup within the cavity. Repeated measurements on samples fabricated with various radii (80-120 micron) and torii thickness (5-10 micron) yielded Q values in excess of 100 million (10^8). This is a record value for a planar device and constitutes an improvement by nearly 4 orders of magnitude over all previous planar microresonators fabricated by wafer-scale processing (the highest values[15, 27] reported at the time of the publication in Nature were far less, $\sim 2\times10^4$).

As an independent and more precise measurement of quality factor, the photon lifetime was directly measured by cavity ringdown. This was done by repeatedly scanning the laser into resonance with a mode that was critically coupled to the taper. As the laser scanned into resonance, power transfer increased until maximal "charging" of the resonant mode was attained. At this moment, the laser input was gated "off" by use of a high-speed, external modulator and cavity ringdown is observed as the resonant power discharges. Because the resonator is by necessity loaded during this measurement, the observed ringdown time yields the cavity lifetime at the critical point, $\tau_{crit,}$ and the loaded Q-factor (not the intrinsic quality factor, Q_0). Data from a typical ringdown measurement is shown in Figure 2-7. At time t=0 in the figure, a signal is applied to "gate" the laser off. When the laser input is fully off, the detected power is due entirely to the cavity discharge field. The solid line represents an exponential fit as expected for decay of a single cavity mode. The inset shows a logarithmic plot to infer the cavity lifetime. The loaded lifetime in this structure was 43 ns. As a further check on this time constant, after gating of the pump laser, the waveguide power has dropped to 80% of its predicted maximal value based on extrapolation of data to t=0. This value is in agreement with the gating delay of the ringdown setup ($\Delta t \cong 8$ ns). In particular, using the observed mode-lifetime of τ_{crit}=43 ns yields $\exp(-\Delta t/ \tau_{crit})=0.83$.

As noted, to infer the intrinsic cavity Q it is necessary to correct for loading by the taper waveguide. In addition it is necessary to take into account excitation of the counter-propagating mode due to scattering centers intrinsic to the resonator (described by a dimensionless intermode coupling parameter Γ). The techniques used to measure this parameter in ultra-high-Q taper-coupled resonators are described elsewhere[28]. For the mode of Fig. 2-7 the intermode coupling was measured to be approximately 1, giving rise to a weak counter-propagating wave excitation (17% of the cavity buildup field is stored

in the counter-propagating mode at critical coupling). In the presence of intermode coupling the relationship between the critically-coupled lifetime and the intrinsic (unloaded) cavity quality factor, is given by,

$$Q_0 \equiv \omega\tau_0 = \omega\tau_{crit}(1+\sqrt{1+\Gamma^2})$$

This yields an intrinsic cavity Q of 1.25×10^8 inferred from cavity ringdown. This value agrees with the measurements of the frequency line shape described above.

2.3 Characterization of the Microdisk

In order to fully characterize the improvement in Q factor that results from the laser induced reflow, the quality factors of the microdisk were measured prior to the treatment (Figure 2-8). Using the previously mentioned coupling techniques, the Q factors of WG resonances were inferred by linewidth measurements, using a 300-KHz external-cavity diode laser to excite the resonances in the 1550-nm band. Q factors above 1 million were consistently observed, the highest observed value being 3.2×10^6 (Figure 2-9 and 2-10). We attribute the high Q factor, despite the lithographic roughness, to the wedge-shaped feature noted earlier. The wedge is believed to induce modal isolation from the disk edge, where the etch blemishes are most pronounced.

2.4 Raman Lasing

Nonlinear processes in silica microtoroids were also observed when the toroid microcavities were pumped at high power levels. One optical nonlinear effect that was investigated using these devices was stimulated Raman scattering. By use of an erbium-doped fiber amplifier to boost the external-cavity pump wave to power levels of 25 mW, a highly nonlinear emission spectrum is produced with a 53-μm-diameter microtoroid (Figure 2-11). The spectrum consists of frequency redshifted stimulated Raman modes as well as blueshifted modes that are due to Raman-assisted four-wave mixing. It is important to note that all the participating modes in this nonlinear process are single azimuthal modes, spaced by the free spectral range of the cavity (10 nm). The generated radiation spans nearly 35 THz, and the highest fiber-coupled power of individually oscillating modes is nearly 2.5 mW (see the inset of Fig. 2-11). This was the first demonstration of a chip-based Raman laser. The microlasers exhibit ultralow threshold, high efficiency, and single-mode emission. Also, they are coupled with high ideality by use of tapered optical fibers. The lasers are fabricated with standard silicon processing techniques, allowing integration of Raman microlasers with complementary optical, mechanical, or electrical functionality.

2.5 Conclusion

In summary ultra-high-Q planar cavities on a chip have been fabricated for the first time. Toroid-shaped microcavities were formed using a combination of lithography, dry

etching, and a novel selective reflow process. Self-limited collapse of a molten silica disk enables the dimensional control typical of wafer-scale processing while providing the surface finish (and hence cavity Q) typical of a spherical resonator. Q values obtained by this process are typically 4 orders of magnitude higher than previous wafer-based resonators. The planar nature of the toroid microcavity and the large transparency window of silica suggest that these devices will find a wide range of applications in photonics as well as in fundamental studies. As an indication of the possibilities for these structures, in the course of this work nonlinear optical effects have been observed with characteristics comparable to recent studies on spherical ultra-high-Q cavities: in particular Raman lasing thresholds as low as 75 microwatts of pump power were demonstrated.

As standard processing techniques are used, the addition of optical functionality by techniques such as doped coatings is possible and will be discussed later in this thesis. Likewise, electrical functionality is also introduced to integrate control functions such as dynamic tuning and micropositioning with the ultra-high-Q microcavities. More generally, this work provides a new functional element that is synergistic with recent demonstrations of basic experimental physics on a chip. For example, by combining the present results with techniques recently demonstrated to integrate atomic traps on a chip[29] it would be possible to achieve chip-scale integration of cQED experiments and related devices. Finally, there is great interest in improving the sensitivity of biological and chemical sensors. Proposals for high-sensitivity sensors based upon optical resonators have already benefited from the ability to attain ultra-high-Q on a chip.

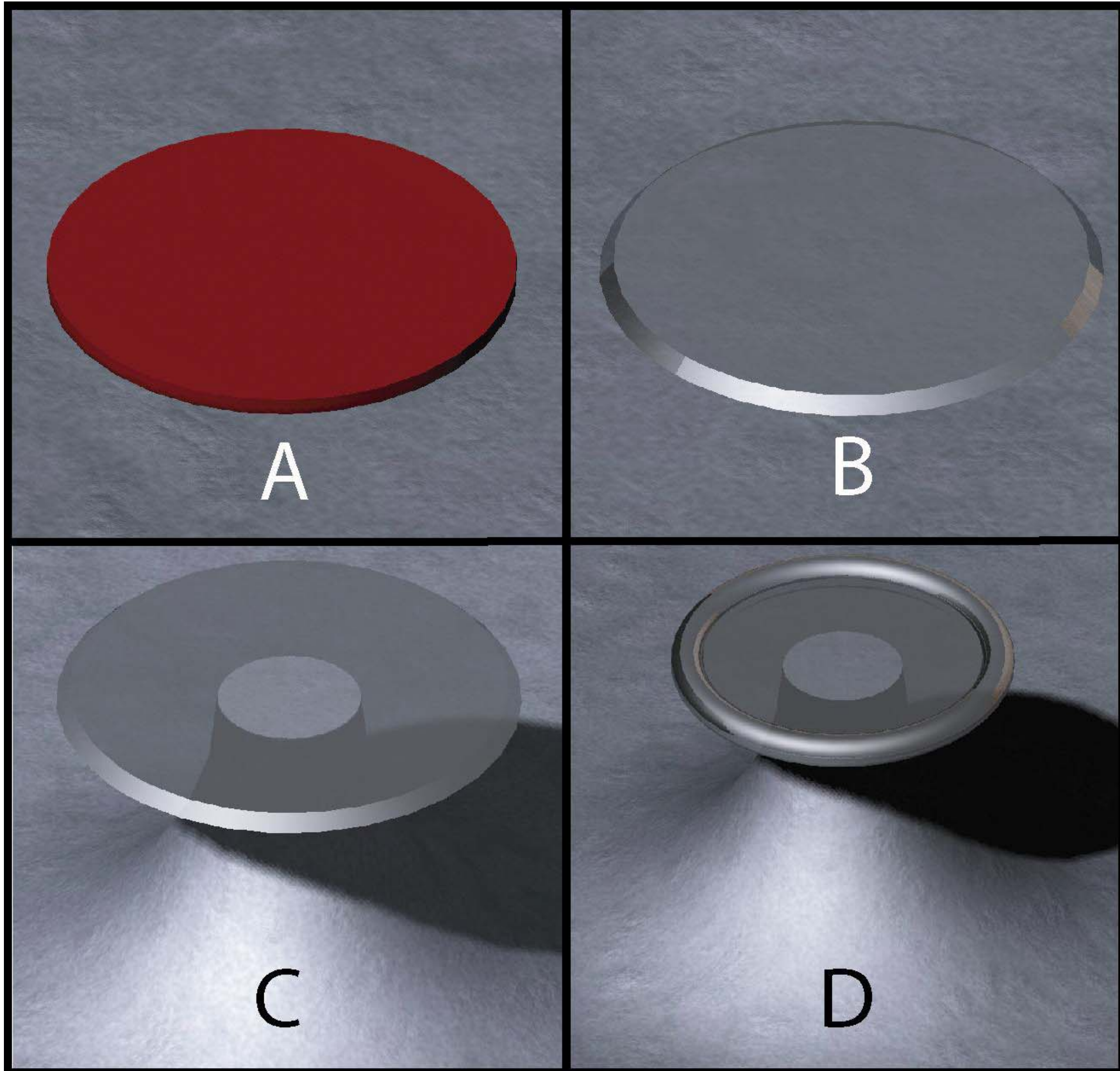

Figure 2-1: Four step fabrication flow of the microtoroid resonators. A: Photolithographically define photoresist disks. B: Using buffered HF-acid, etch the silica and remove the photoresist leaving circular silica disk. C: Undercut the disks using XeF_2 to istropically etch the silicon. D: Perform laser activated reflow using a CO_2 in order to form the microtoroid resonators.

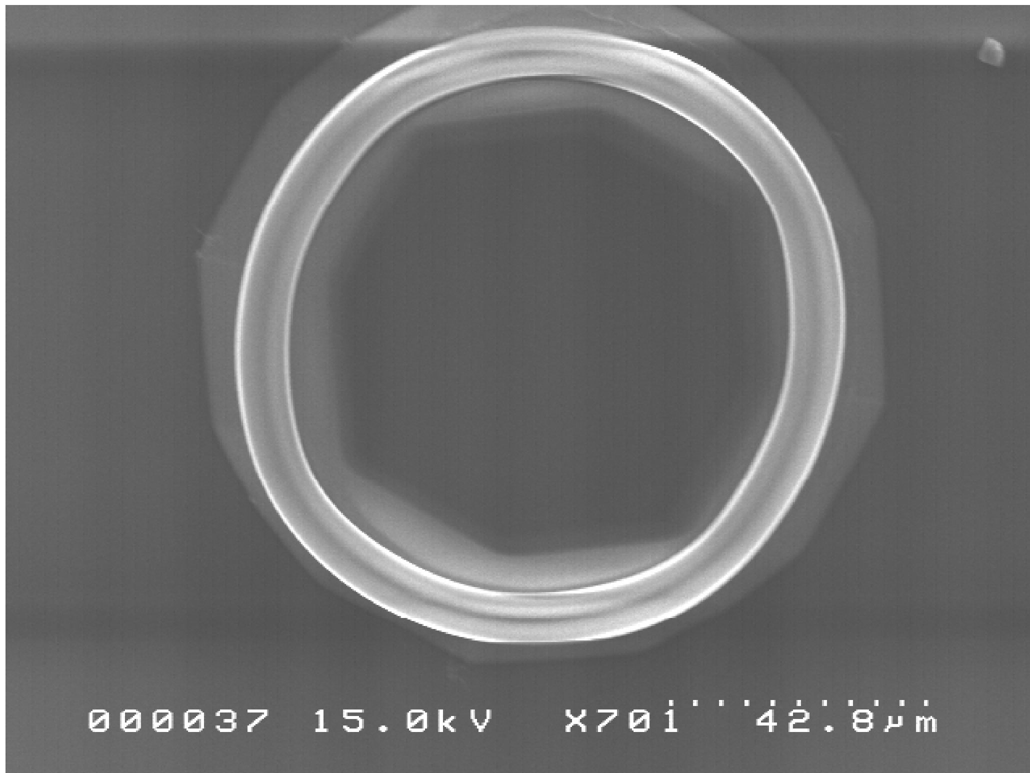

Figure 2-2: A scanning electron micrograph of a microtoroid resonator undercut using EDP as the silicon etchant: note the non-circular shaped pillar and irregular toroid.

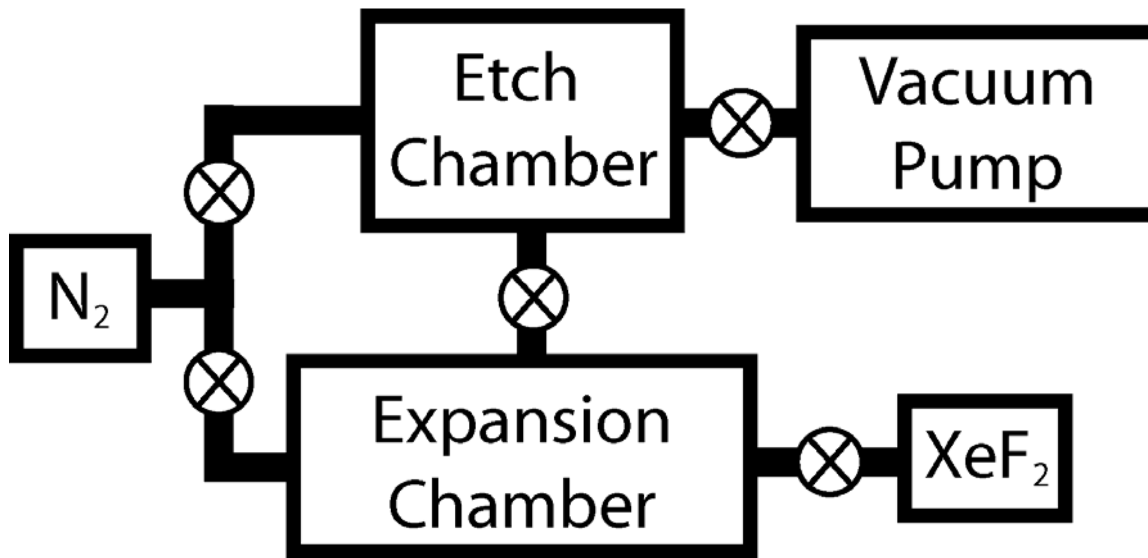

Figure 2-3: A schematic diagram of the xenon difluoride etch system (top). A picture of the actual system in the Vahala lab cleanroom (bottom).

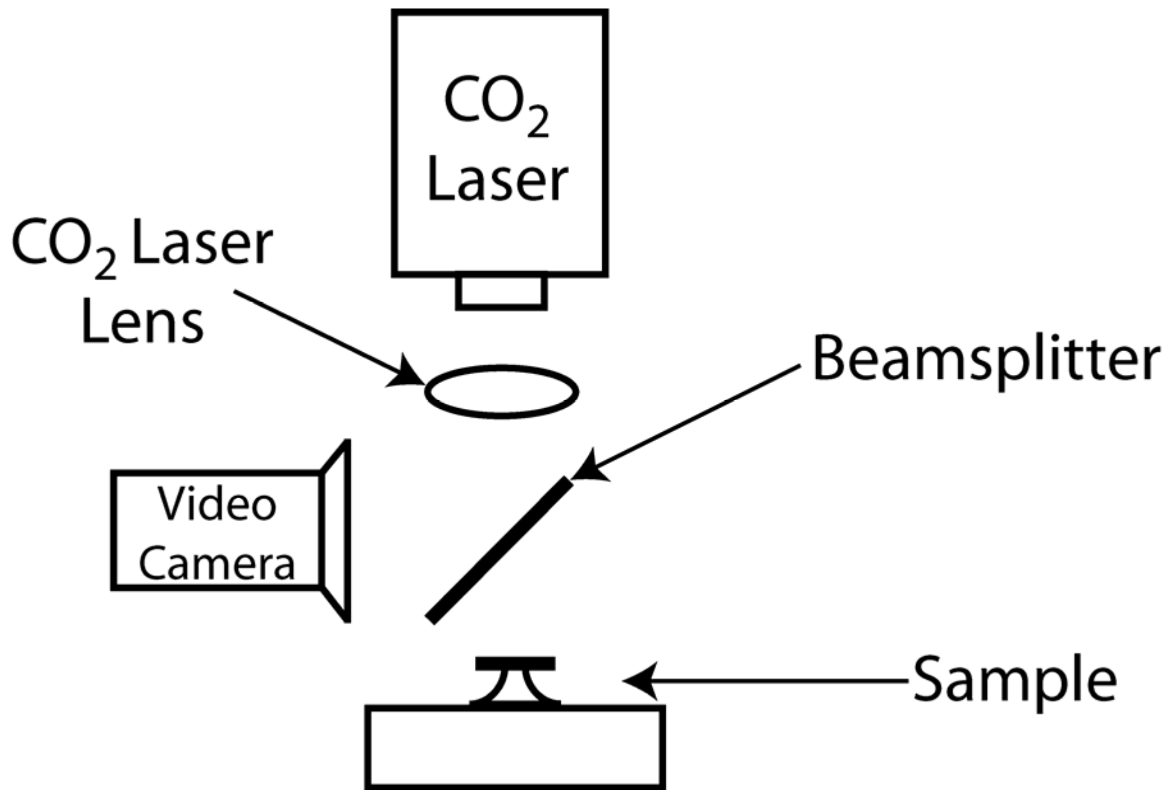

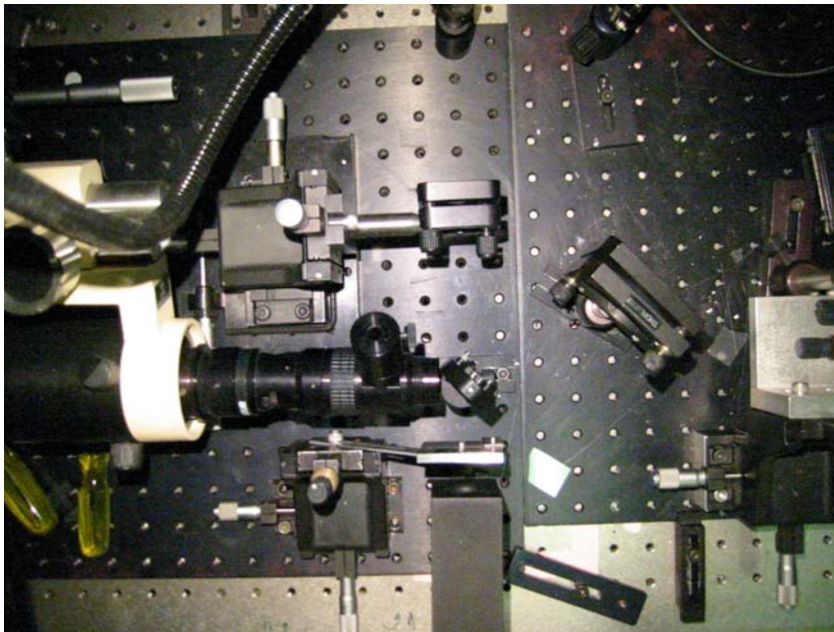

Figure 2-4: CO_2 laser system for the microtoroid reflow process. The sample is imaged simultaneously while the laser activated reflow process takes place.

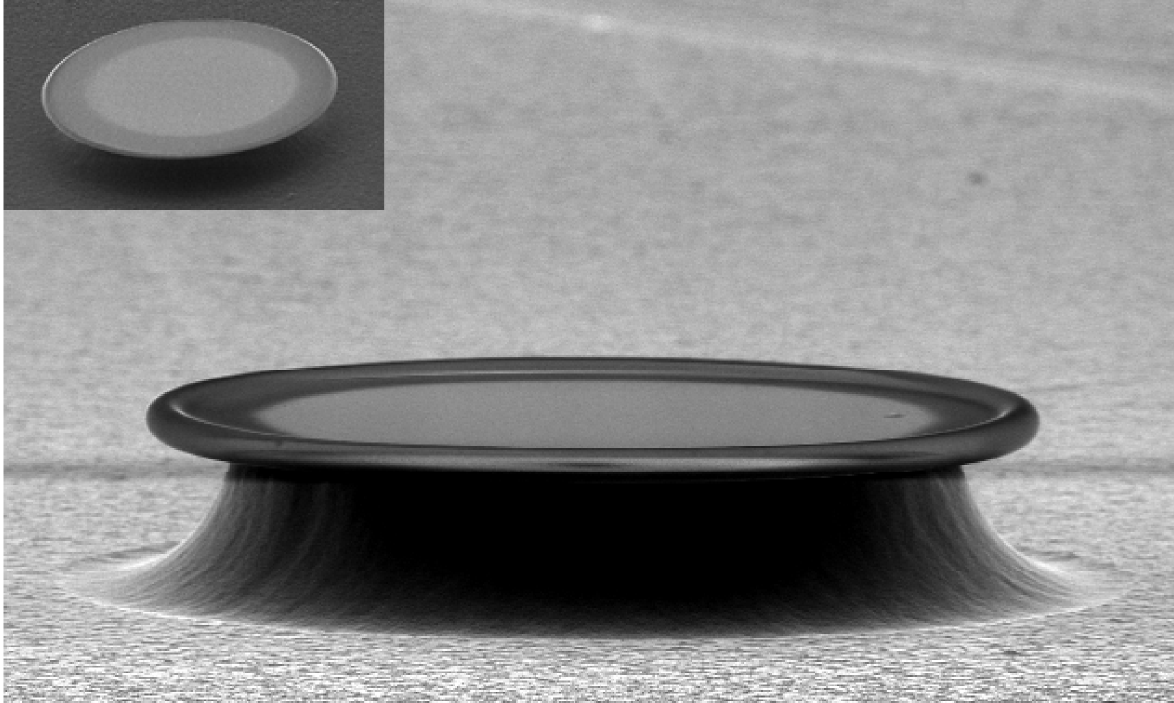

Figure 2-5: A scanning electron-micrograph of the microtoroid resonator. Inset: A scanning electron-micrograph of the microdisk resonator (prior to the reflow process).

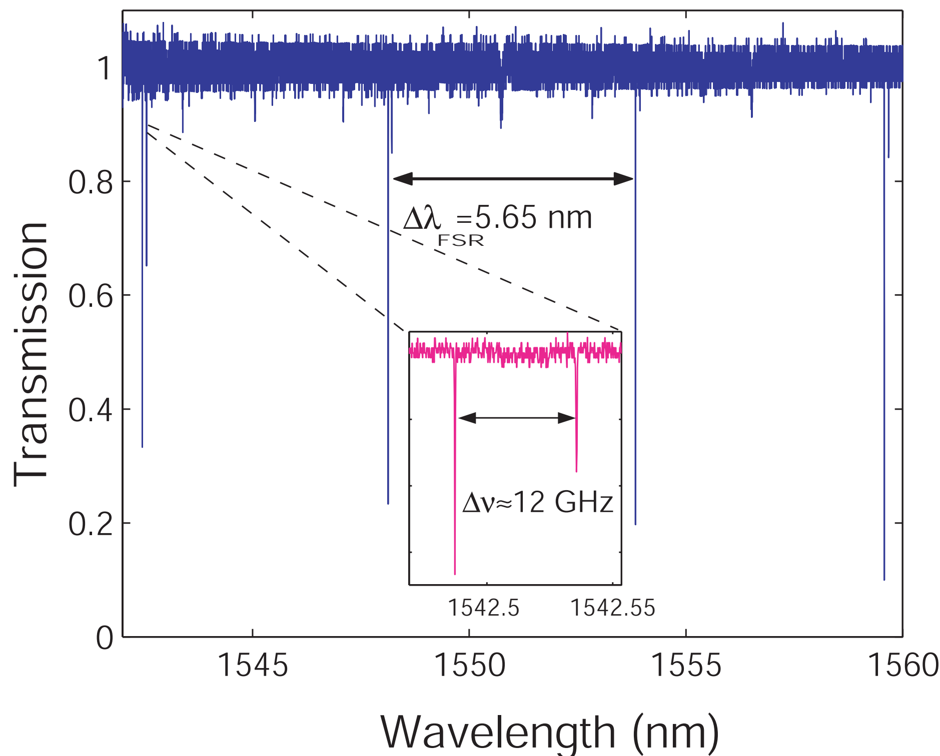

Figure 2-6: Transmission spectra of a toroidal resonator. The free spectral range (defined as the wavelength spacing between modes with successive angular mode number) is 5.65-nm, which corresponds to a torus approximately 94-μm in diameter. The inset shows what we believe to be the two lowest-order radial modes (based on modeling of a microdisk resonator). Additional subsidiary peaks are attributed to other radial or azimuthal modes.

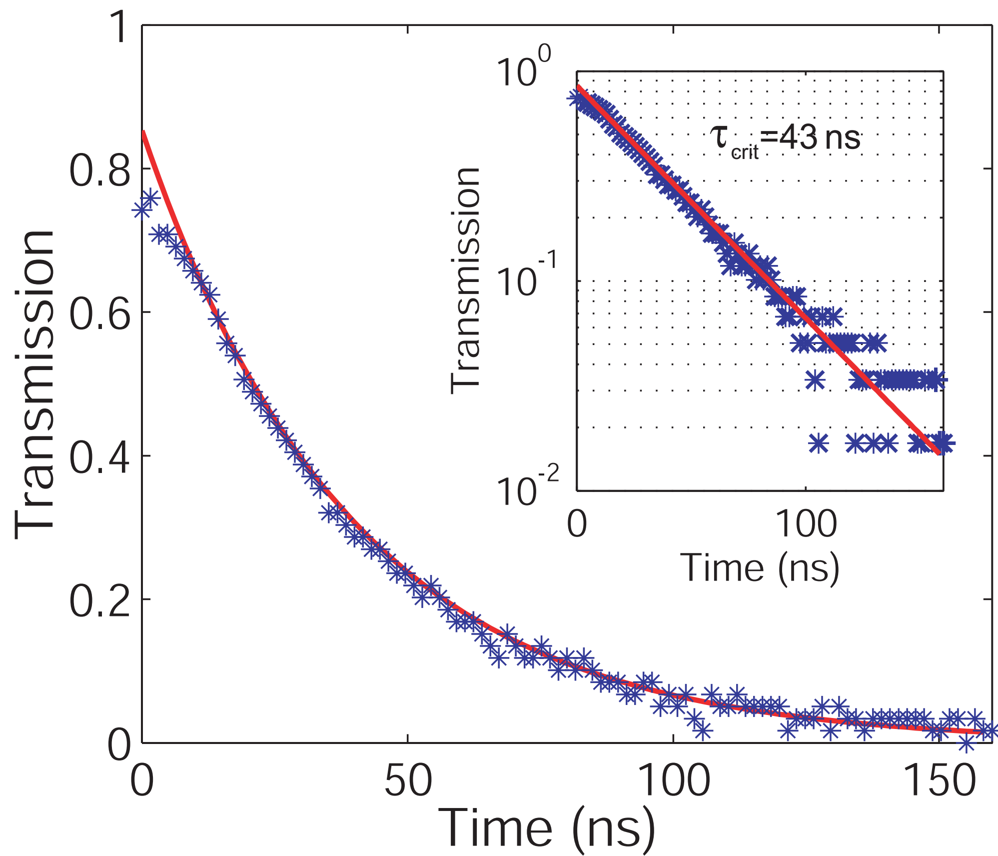

Figure 2-7: Ringdown measurement of a 90-micron-diameter toroid microcavity at the critical-coupling point. The measured lifetime of τ_{crit}=43 ns corresponds to an intrinsic quality factor of $Q=1.25\times10^{8}$.

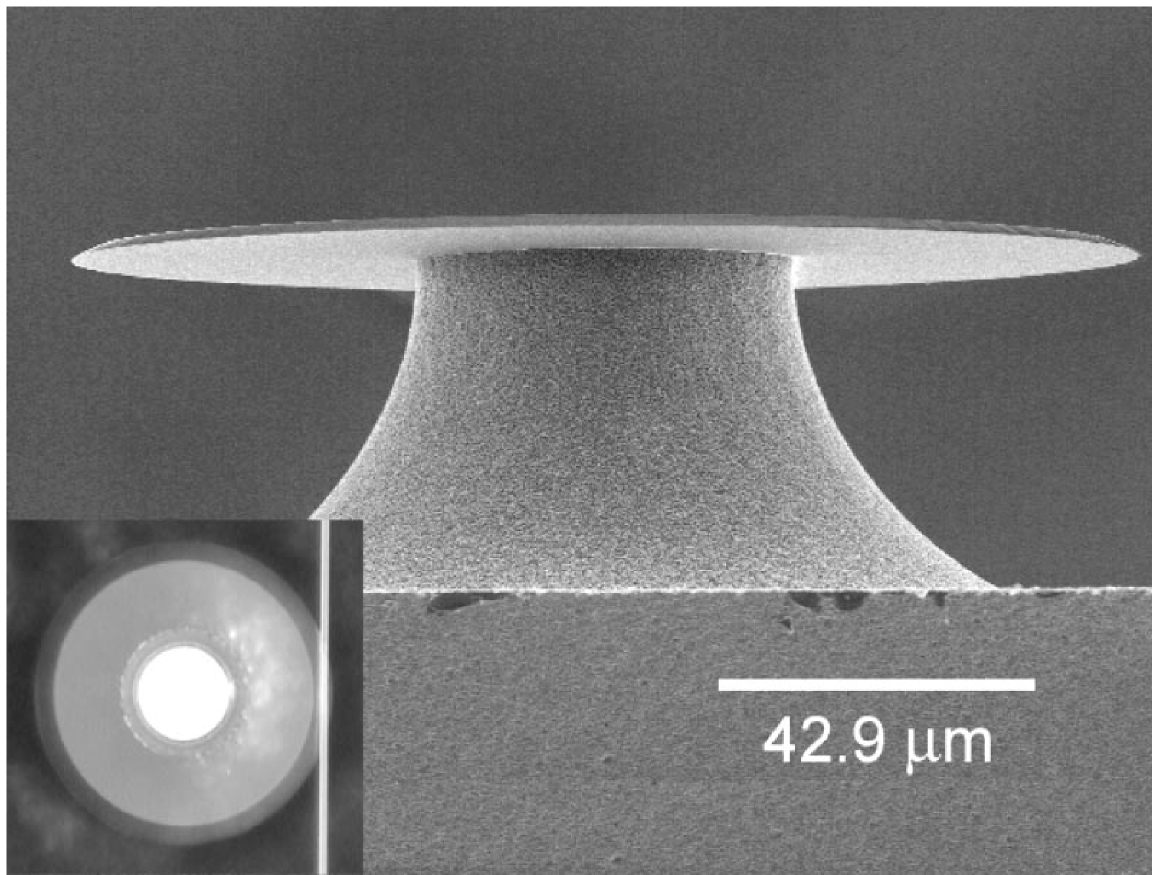

Figure 2-8: SEM micrograph of a 120-µm-diameter microdisk resonator (2-µm thick oxide disk). The inset shows an optical micrograph of a resonator coupled to a tapered optical fiber.

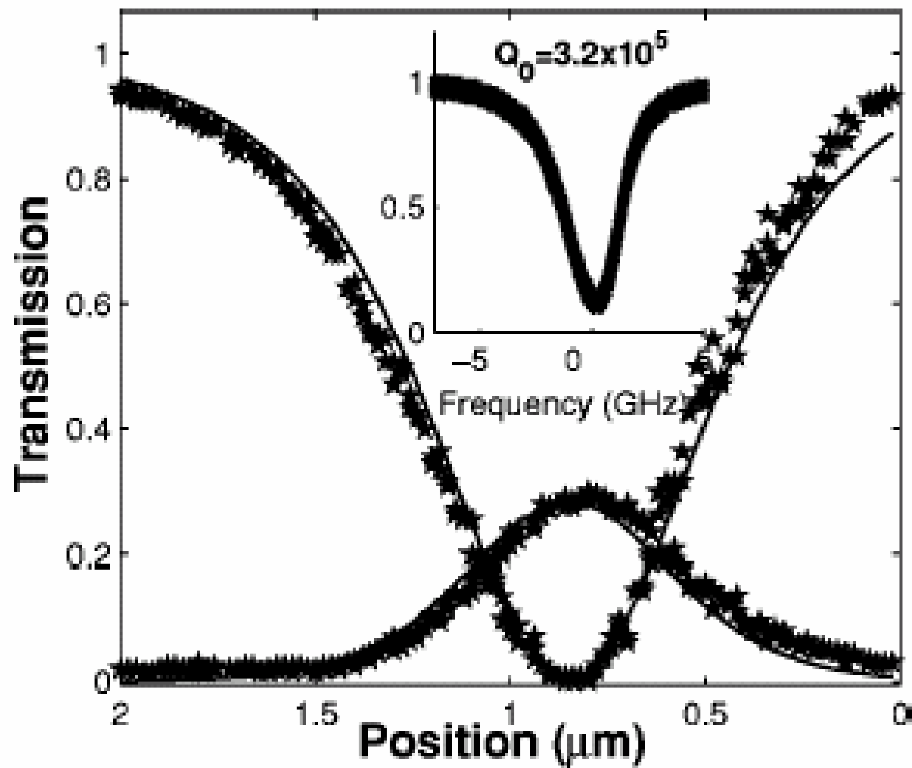

Figure 2-9: Transmission (normalized with respect to the launched fiber power) and reflection properties versus taper-disk gap distance. The inset shows the transmission versus frequency near the critical point. The off-resonant loss was less than 5%.

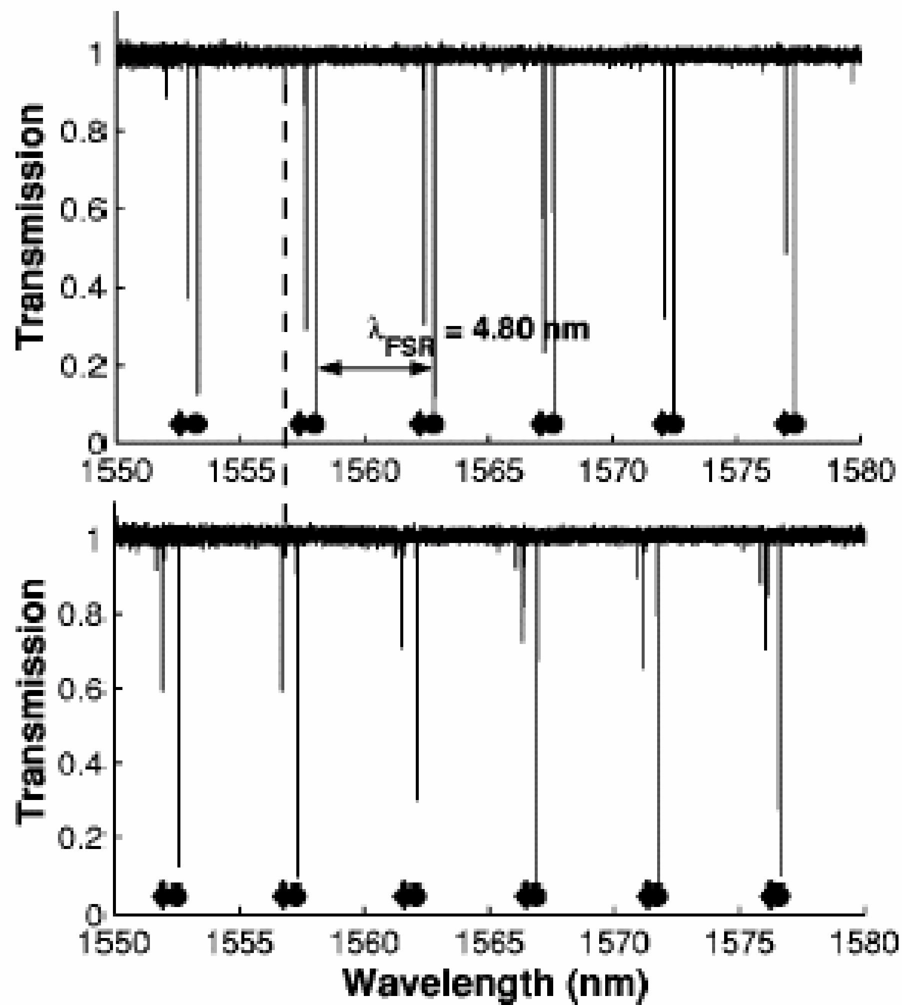

Figure 2-10: Mode spectrum of a 114-μm-diameter resonator for TE and TM polarizations. The circles and diamonds represent the first- and second-order radial modes, based on modeling.

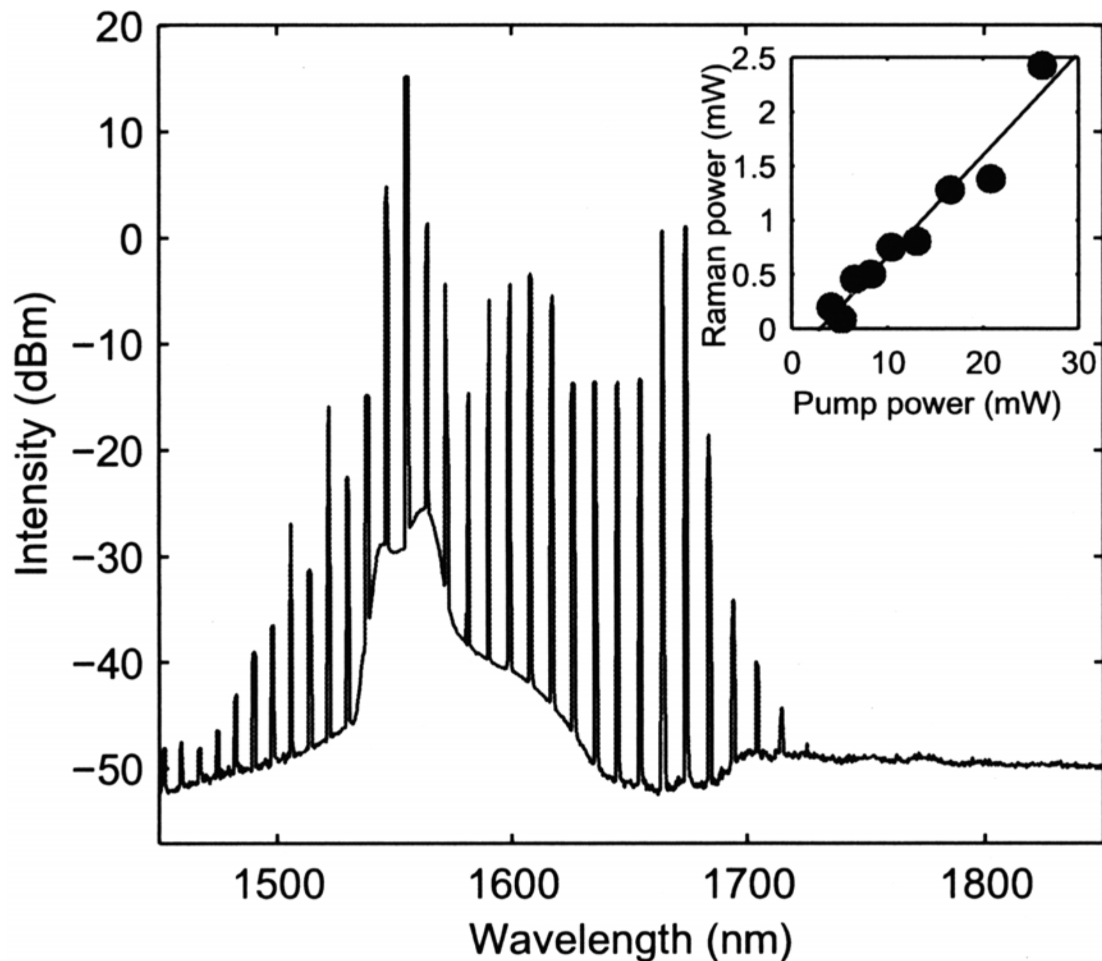

Figure 2-11: Broadband frequency generation in a microtoroid. Raman laser pumped far above threshold at 1550-nm wavelength. Inset, 2.5 mW of output power from a single Raman emission wavelength near 1680 nm. The modes are spaced with the free spectral range of the cavity.

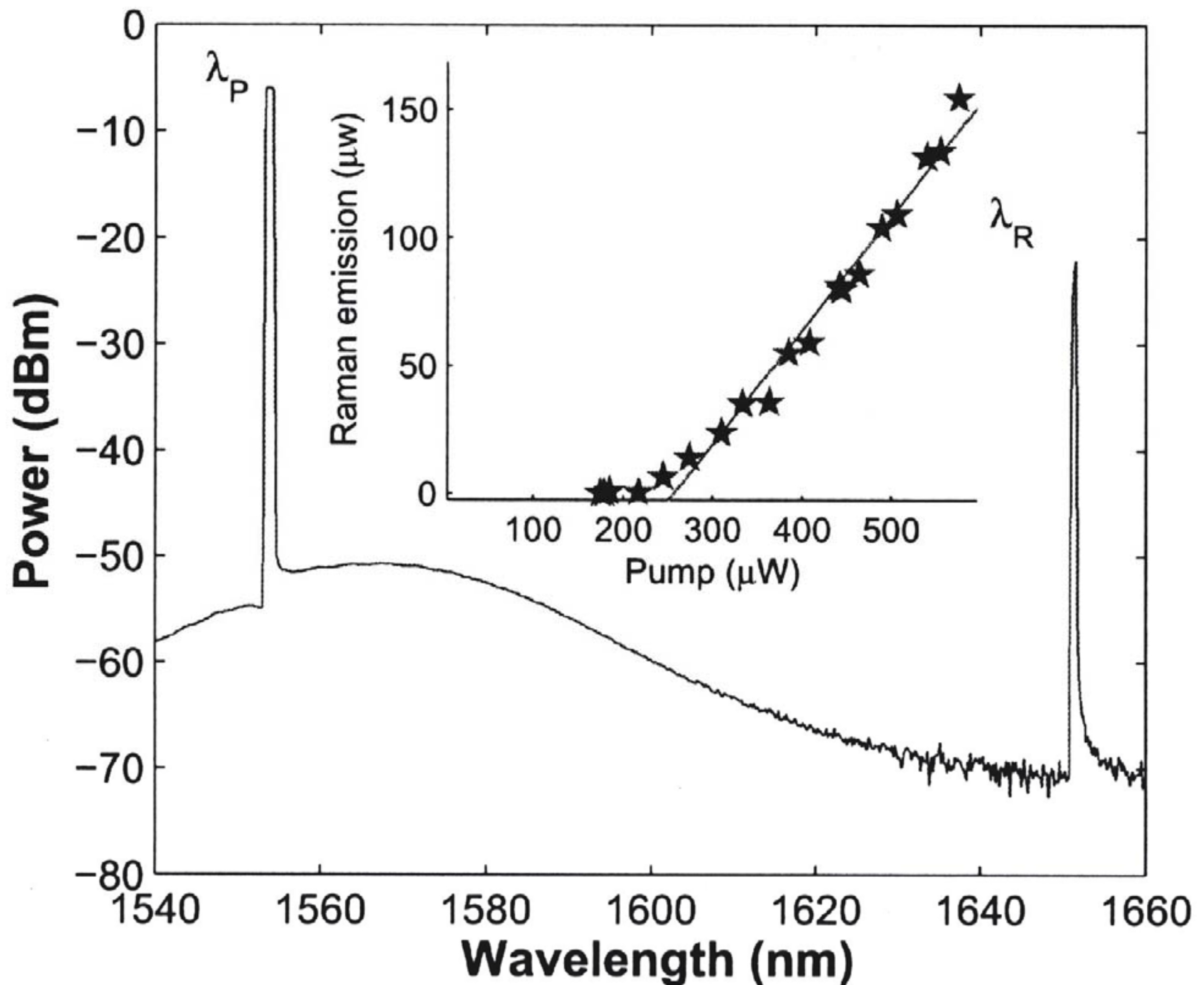

Figure 2-12: Raman emission spectrum of a toroid microcavity showing single-mode oscillation. The pump is located at 1550 nm, and the Raman emission is shifted 12.5 THz into the 1650-nm band. Inset, bidirectional Raman emission as a function of pump power for a 58-mm-diameter toroid microcavity Q=$.6\times10^{8}$ at the critical point. The threshold is 250 μW, and the bidirectional conversion efficiency is ~45%.

Chapter 3 - Electrical Thermooptic Tuning of Microtoroid Resonators

3.1 Introduction

The ability to tune resonant frequency in optical microcavities is an essential feature for many applications. Integration of electrical-based tuning as part of the fabrication process has been a key advantage of planar microresonant devices. Until recently, the combination of these features has not been available in devices that operate in the ultra-high-Q regime where device quality factors (Q) can exceed 100 million. In this chapter an electrically tunable resonator on-a-chip with ultra-high quality factors is demonstrated. Futhermore, the devices have demonstrated tuning rates in excess of 85 GHz/V^2 and are capable of tuning more than 300 GHz.

Ultrahigh-Q (UHQ) optical microresonators represent a distinct class of microcavities[30] with applications ranging from optical communications and biosensing[8] to fundamental studies of nonlinear optical effects[6] and cavity quantum electrodynamics (CQED)[2]. Although wafer-scale tuning control has been available for devices operating in the Q regime below 100,000, such methods have not been available in the UHQ regime, where Q can exceed 100 million. Nonetheless, there remains keen interest in finding more practical ways to implement tuning control in this regime[31, 32]. In this chapter electrical control of resonant frequency in an ultra-high-Q microtoroid by thermooptic tuning is demonstrated. The significance of this result is that this represents an example of a UHQ microresonator with “integrated” electrical tuning.

By including only two additional processing steps (lithography and metallization) into the prior fabrication process for the UHQ microtoroids, electrical control is implemented. The end result is a highly reproducible process through which chip-based electrically tunable microtoroids with Q factors in excess of 100 million are fabricated. Furthermore, since the devices themselves are produced on a silicon substrate and significant tuning range at sub-volt levels is demonstrated, the integration of CMOS control circuitry with the devices is also possible. In addition to characterizing the static tuning characteristics of these devices, dynamic response was determined with the use of a helium ambient atmosphere to isolate the specific source of the tuning time constant.

3.2 Fabrication

The fabrication process is similar to the microtoroid process flow with the addition of another mask and lithography step as well as the deposition of a metal layer. The process flow is described here in detail and proceeds as follows (see Figure 3-1). First, (Shipley) S1813 photoresist is spin coated onto a highly p-doped (.001-.006 Ω-cm) silicon wafer with a 2-μm thick thermal oxide. The resist is exposed to the first mask, that is used to define the oxide disks as well as an electrical contact hole. The mask used is similar to the one used for the microtoroids with the addition of a concentrically located hole, which will serve as the ohmic contact after metallization. Following UV exposure, the wafer is immersed in MF-319 (Shipley) developer. Once fully developed, the wafer is rinsed with DI water and blow dried. It should be noted that care must be taken to ensure that the backside of the wafer remains free of PR in order to ensure that the oxide is

completely removed during later processing steps. The unexposed photoresist (PR) is used as an etch mask during immersion in buffered HF, which etches the silicon oxide. These two steps define oxide disks of 100-μm diameter with a 25-μm wide contact hole concentrically located on the disk. All oxide on the backside of the wafer is also removed. The remaining PR is rinsed away using acetone, IPA, and water and then blow dried.

Photolithography is performed again using the same processes mentioned above. The mask used in this step is used to define the metal lift-off mask; as a result nearly all of the PR remains except for the central contact area of each silica disk that is exposed. One-thousand angstroms of aluminum are thermally evaporated on both sides of the wafer in sequential deposition steps. The wafer is then immersed in acetone overnight releasing the excess aluminum and leaving aluminum contacts in the center of the oxide disks as well as on the backside of the wafer. Ohmic contacts are formed by annealing the wafer in a tube furnace at 500°C in a nitrogen ambient. The remaining oxide disks act as etch masks during exposure to xenon difluoride (XeF_2) gas at 3-torr. Xenon difluoride isotropically etches the silicon substrate leaving the perimeter of the silica disk isolated from the higher index silicon (Figure 3-1C,3-2). To eliminate lithographic blemishes along the perimeter of the oxide, each microdisk is orthogonally exposed to a CO_2 laser beam resulting in surface tension induced reflow and formation of the microtoroid[33]. During this process the central region of the pillar is unaffected, and therefore the aluminum contact remains pristine. The resulting device possesses a surface finish with near atomic roughness in addition to integrated metal contacts (Figure 3-1D, 3-3).

3.3 Characterization

The tuning range and frequency response of the tunable microtroid resonators were measured in the optical telecommunication band (1550-nm). To create a low resistivity electrical path, the substrate (now containing an array of microtoroids on one side) was placed on a metal, electrically-grounded platform mounted to a three-axis stage with a 100-nm step resolution. The stage allowed the substrate to move freely so that the taper waveguide could couple to a single microtoroid. Two microscopes were used to simultaneously image the microtoroid from both the top and side. Optical power was coupled to the microtoroid using a tapered fiber waveguide[25]. The tapered fiber was formed by stretching a standard optical fiber (SMF-125) while heating it with a hydrogen flame. As the adiabatic condition is maintained during the stretching process, the resulting tapered fiber exhibits losses typically less than 5%. Further details regarding tapered fiber fabrication and properties are provided elsewhere[26, 34]. It should be noted that during characterization of both tuning range and frequency response the microtoroid and fiber taper waveguide were in contact to prevent any thermally-induced loading variations.

With the taper and microtoroid in contact, the aluminum pad in the center of the microtoroid is electrically contacted using a tungsten probe tip (Figure 3-4, 3-5), and voltage is applied while the silicon substrate is grounded. The typical electrical resistance of the devices was consistently less than 10-Ω. The induced ohmic heating and rise in temperature that occurred in the silicon pillar was thermally conducted to the silica

microtoroid, subsequently increasing the temperature of the silica in the path of the optical whispering gallery mode. This temperature increase resulted in a frequency shift of the resonant frequencies.

The tuning rate and tuning range were determined by scanning a single-frequency, external-cavity laser (coupled to the tapered fiber waveguide) across a frequency span of approximately 50 GHz and in the spectral vicinity of a high-Q resonance. Transmission power through the taper was monitored on an oscilloscope during scanning to measure tuning. With the laser continuously scanning, voltage was incrementally applied to the microtoroid resonator. Figure 3-6 shows an example of a typical tuning curve for a microtoroid resonator with a resistance of 7-Ω and tuning rate of 85 GHz/V^2. The tuning is plotted against V^2 in order to stress the dependence of tuning on applied electrical power (V^2/R).

The frequency response characteristics were measured by first tuning the laser near a resonance, and simultaneously a function generator was used to apply a small-signal sinusoidal modulation voltage. A lock-in analyzer was set up to detect the modulation induced in the optical power transmission and was referenced to the modulation frequency of the function generator. The frequency response of the tunable microtoroid resonators in both air and helium was measured and is plotted in Figure 3-7. The measured frequency response contains features consistent with the existence of a single, low-frequency pole.

There are several possible cooling mechanisms that could account for this single, low frequency pole. The authors postulate that the primary cooling mechanism is thermal conduction to the ambient. Therefore this cooling mechanism should exhibit a dependence on the coefficient of thermal conduction of ambient atmosphere around the resonator. To confirm this hypothesis, the frequency response was measured while helium gas was introduced into the testing chamber. As can be seen in Figure 3-7 the corner frequency doubled in the presence of helium, a result of helium being five-times more thermally conductive than air.

3.4 Conclusion

In summary we have demonstrated the ability to electrically tune ultra-high-Q microresonators on-a-chip. Furthermore, tuning ranges as large as 300 Ghz have been observed. The corner frequency of the tuning process was measured to be 330 Hz in air and is attributed to thermal dissipation to the ambient. Moreover an understanding of the cooling processes associated with the corner frequency was demonstrated by introducing helium into the air ambient and by observing the resulting increase in corner frequency. While not suitable for high-speed applications, such a device has several important applications. The ability to tune nearly one full free spectral range makes the tunable microtoroids ideal for use as a tunable optical filter or as a tunable laser source[35-38] based on the UHQ properties. Tuning is also an essential feature in application of UHQ devices to cQED[2]. Additionally, the ability to detect small changes in its ambient surroundings can lead to applications in both biosensing and gas detection. Finally,

tunable microtoroid resonators would be well suited for the realization of CROW devices[39].

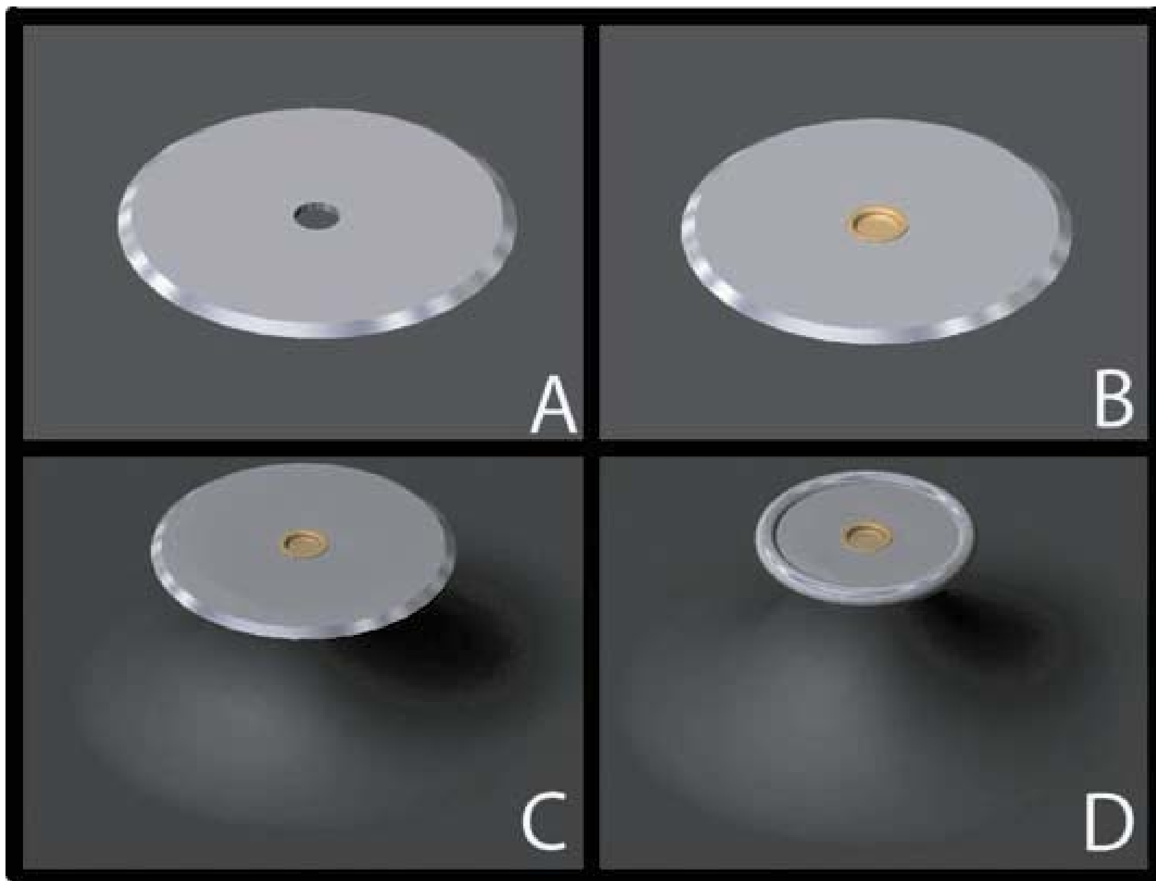

Figure 3-1: Four-step fabrication process flow of the tunable microtoroid resonators. A: Standard photolithography is performed in order to define the oxide disk and contact hole. B: Metal lift-off is performed in order to define the ohmic contact. C: XeF_2 is used to undercut the silica disk. D: CO_2 laser radiation is used to reflow the silica and create the microtoroid.

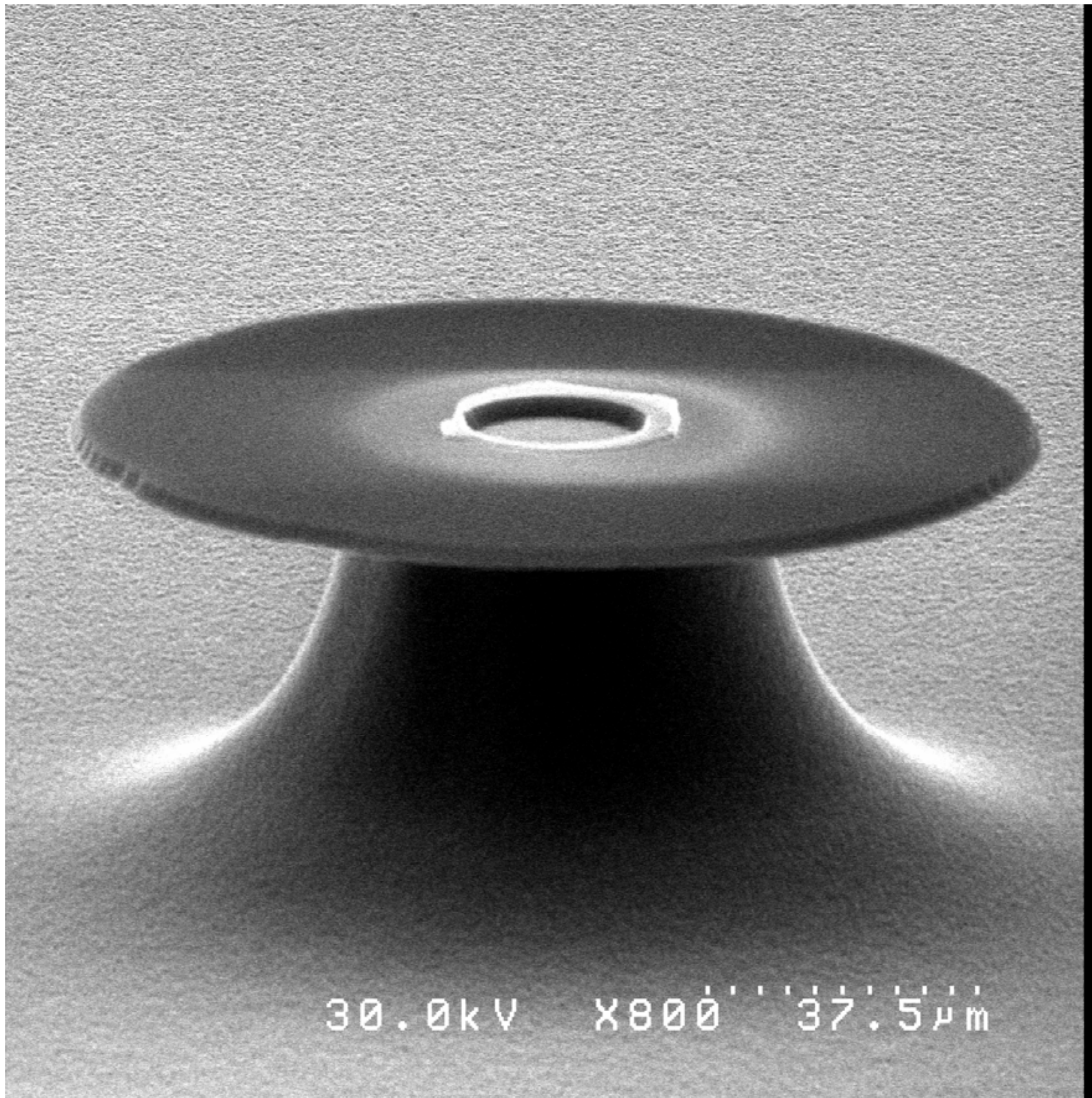

Figure 3-2: Scanning electron-micrograph of the tunable microdisk prior to laser-activated reflow.

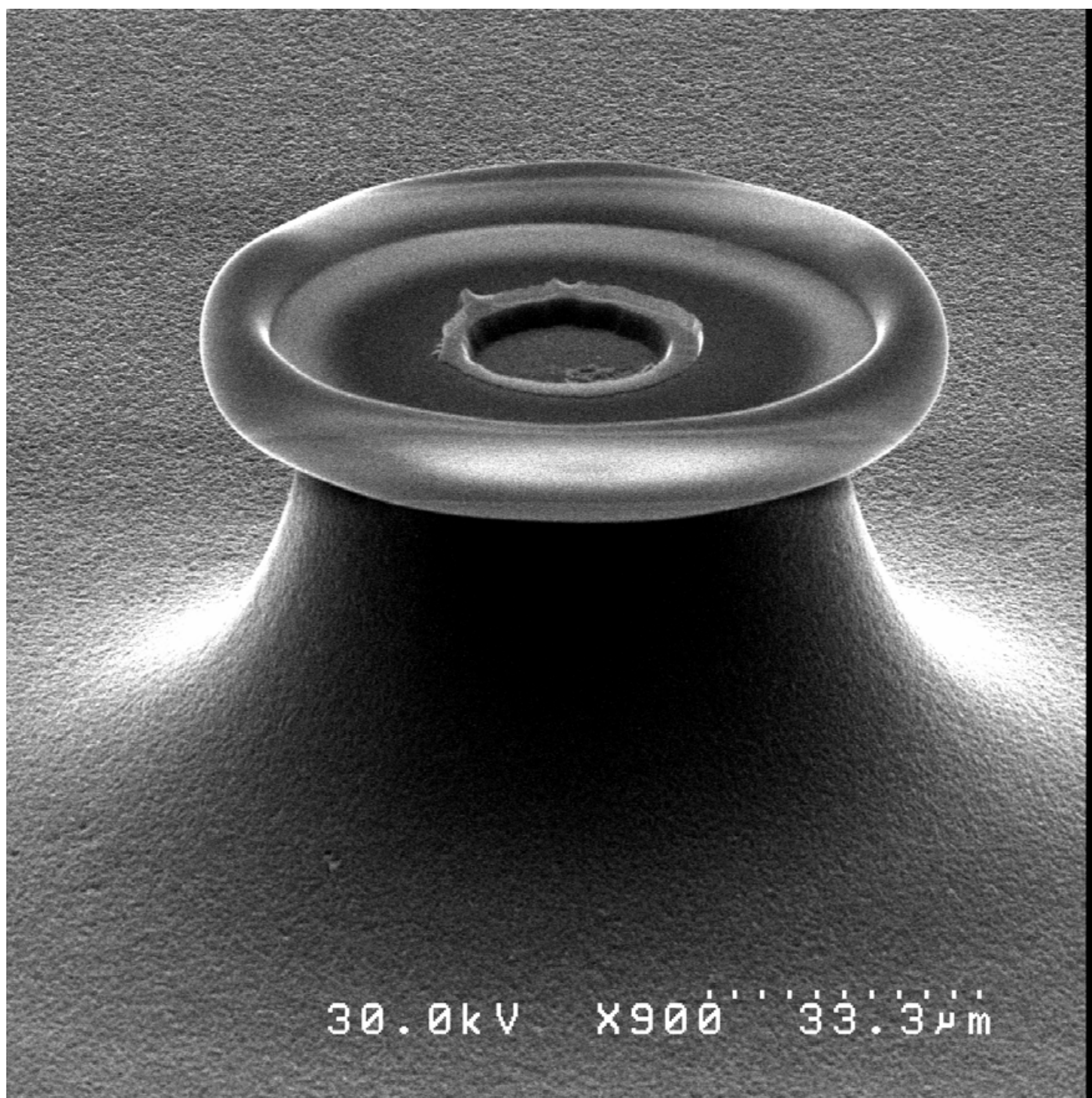

Figure 3-3: Scanning electron-micrograph of the tunable microtoroid.

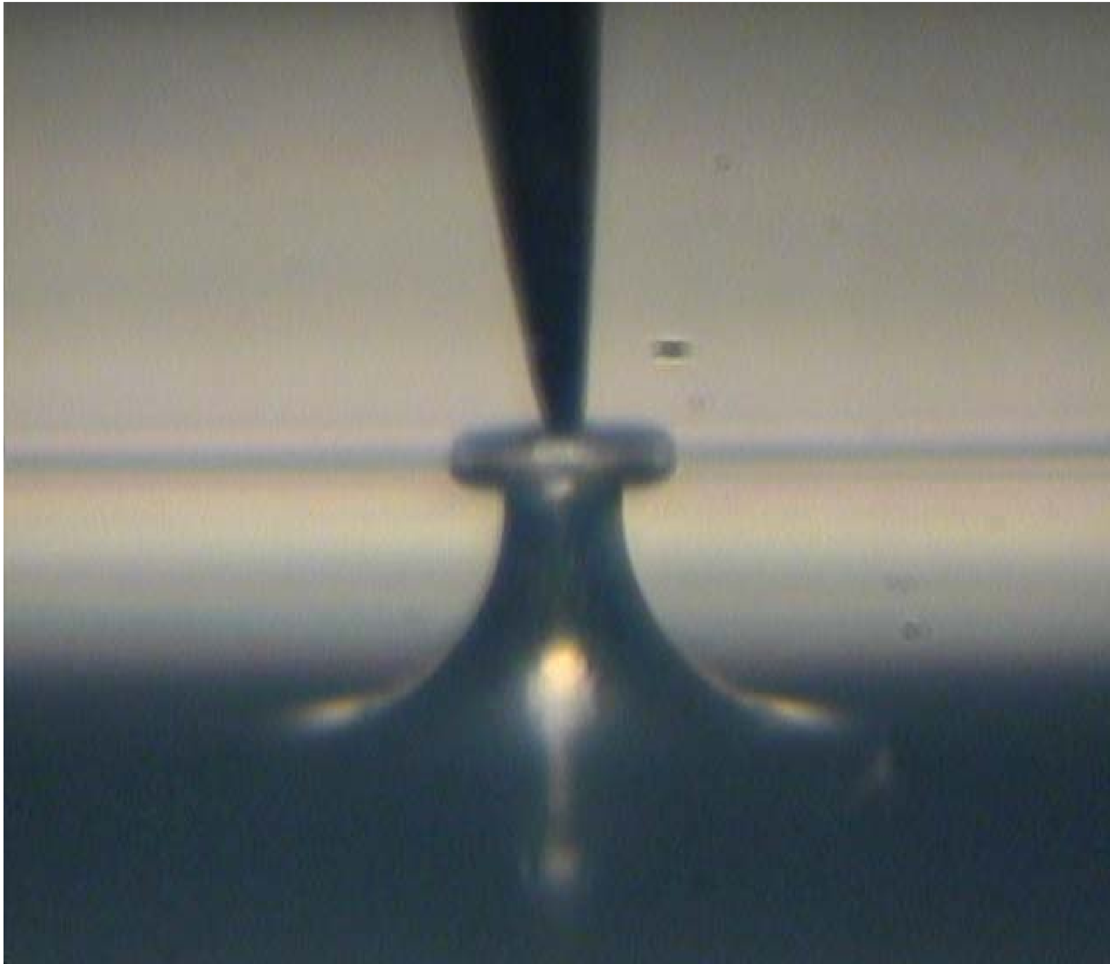

Figure 3-4: A side-view optical micrograph of the tunable microtoroid resonator during testing. Both the tungsten contact probe and the fiber taper waveguide can clearly be seen.

Figure 3-5: A top view optical micrograph of the tunable microtoroid resonator during testing. The aluminum ohmic contact and the fiber taper waveguide can clearly be seen.

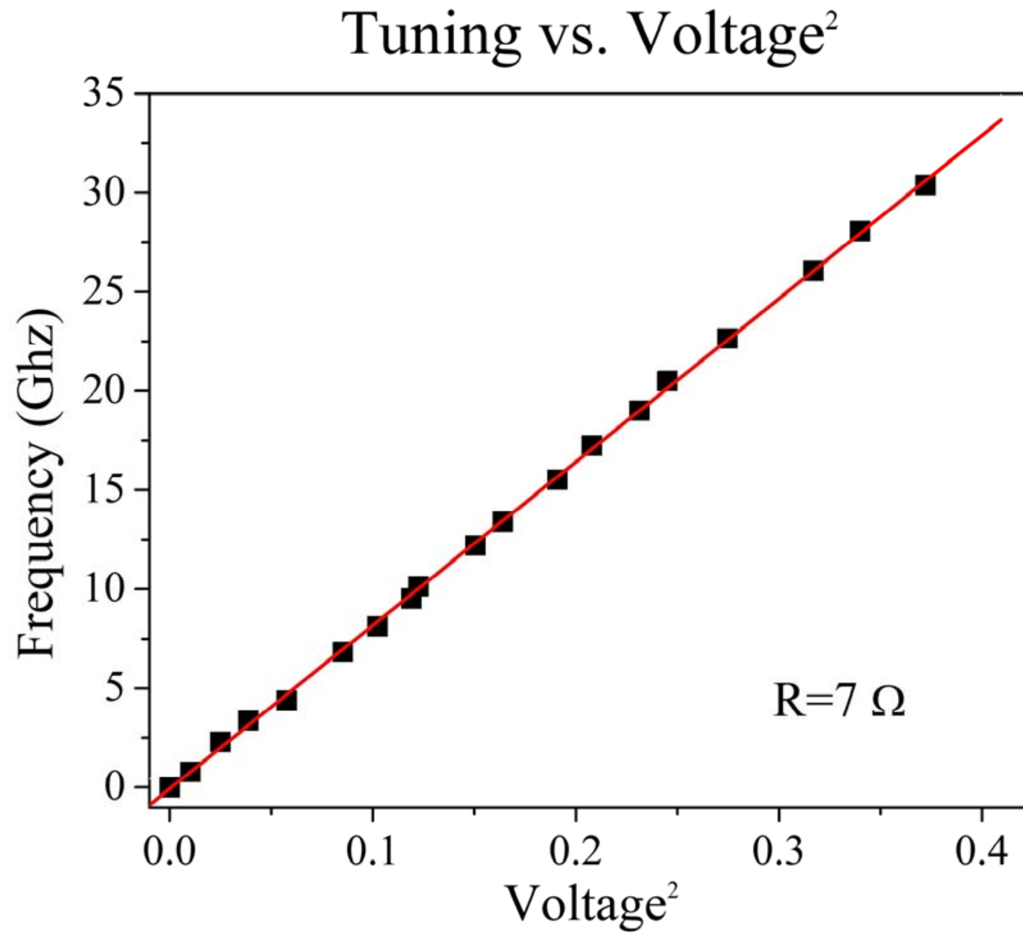

Figure 3-6: Resonant frequency shift versus voltage^2. The quadratic coefficient is 85.56 GHz/V^2.

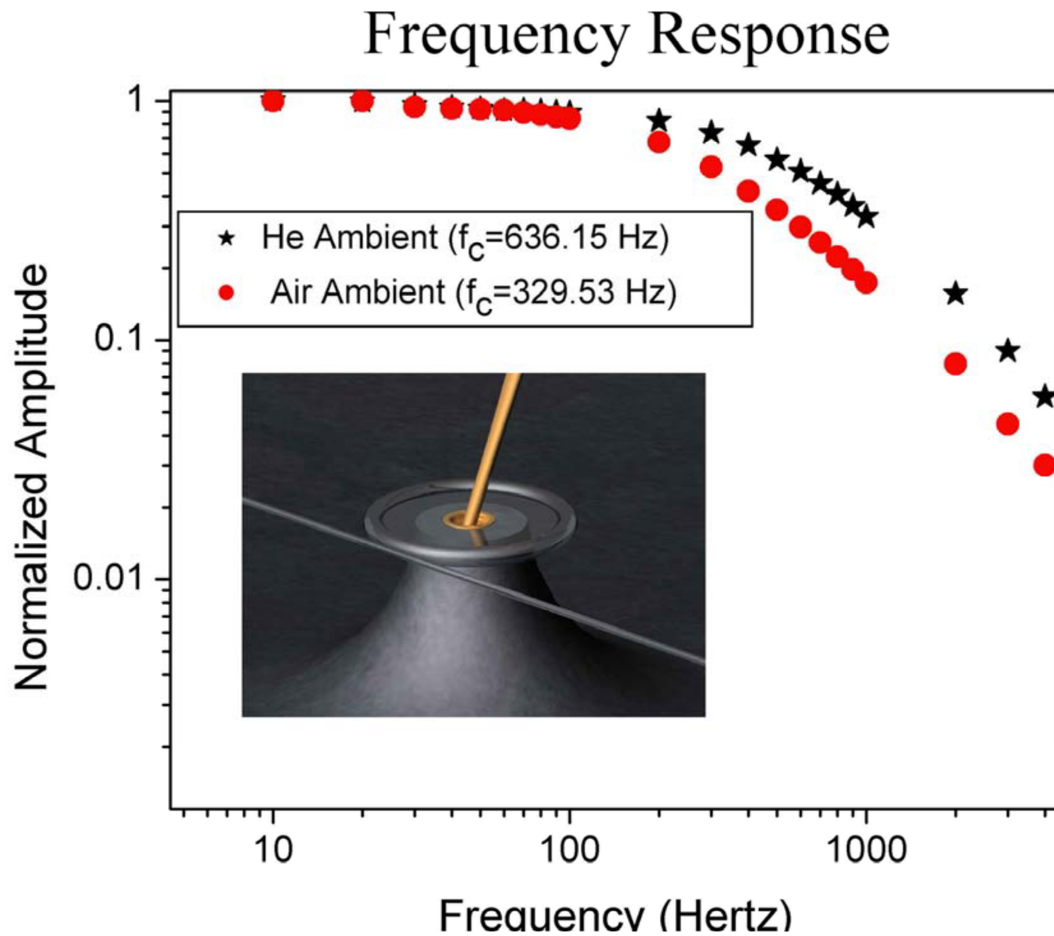

Figure 3-7: The frequency response of the tunable microtoroid resonators in both air and helium ambient atmospheres. Inset: A rendered depiction of the tunable microtoroid device coupled to a tapered optical fiber while being contacted by a metal probe.

Chapter 4 - Microtoroid Resonator with Integrated MEMS Positioner

4.1 Introduction

With the successful demonstration of both UHQ on-a-chip as well as integrated tuning, an integrated positioning system is the last major hurdle to achieving a fully integrated microresonator system. Currently large electromechanical X-Y-Z stages with nanometer resolution are used to control coupling between the taper and microtoroid. The envisioned device is one in which an active MEMS based control system would dynamically control the position of a tunable microtoroid resonator to a static tapered optical fiber. The motivation behind this work is twofold. The first is to achieve a "turnkey" UHQ device that avoids the difficulties and costs typically associated with experiments in the UHQ domain. The second is a key application perfectly suited for such a device, namely a single-pole optical filter in which the filter bandwidth and frequency could be dynamically controlled.

Although the device described in this chapter has evolved over the course of more than a year, it should be noted that this work is still actively being pursued and most likely will yield its most significant results well after this thesis is submitted. The reason associated with the long development time has to do with optimizing the various complex inter-related mechanical, electrical, and optical device parameters. In addition to the difficulties associated with finalizing the device characteristics in all three individual domains previously mentioned, major problems were encountered due to process yield

issues. Put simply, with so many individual parameters to optimize in such a device, it is necessary to have a sufficient quantity in order to properly test and verify.

In this chapter, a detailed fabrication process flow will be outlined for thermally tunable high-Q microresonators with an integrated MEMS based electro-thermal micro-positioning system. Briefly, the device is a tunable silica microdisk resonator attached to a nickel beam. When a DC voltage is applied to the two terminals of the device, the resulting current heats and lengthens the nickel arm. The electrically controlled thermal expansion allows dynamic in-situ control of the taper-microresonator gap. Another set of terminals exist in order to only heat the microresonator and thermooptically tune in a similar manner as demonstrated in Chapter 3. This chapter is concluded with a description of the characterization of the entire system, performance of the device, and an outlook for the future.

4.2 Fabrication

The devices are fabricated on top of <100> oriented silicon wafers that are 100 mm in diameter and only 200-microns thick. The wafer dimensions were specifically selected for two reasons. First, they are an ideal size for the mask aligner used in the Vahala Lab, a MJB-3 with an 80-mm diameter exposure. Second, later in the process it will be necessary to etch through the entire wafer using XeF_2, and a thin wafer is necessary if long etch times are to be avoided. A two-micron thick layer of silicon-oxide was also

grown on the wafers, this thickness was again selected due to the fact that it has been successfully used for making devices in the past.

The wafers were first degreased with an acetone, IPA, DI rinse, blow dried using nitrogen, and then baked at 160ºC for 2 minutes. After baking they were placed in a chamber with liquid HMDS for 2 minutes in order to improve the adhesion between the PR and the silica surface of the wafer. The wafer was then placed on the PR spin-coater and Shipley S1813 PR was poured in approximately the center half of the wafer and set to spin at 1500 RPM for one minute (resulting in a 2-micron thick PR layer). Once the spin-coating process was completed, the wafer was placed on a hot-plate set at 90ºC for one minute. The wafer was then placed in the mask aligner (MJB-3) and exposed to the first mask, similar to that in Figure 4.1.

In this mask step, three critical features are defined, the disk resonator, a pad of insulating silica, and two marks by which mask 2 (Fig. 4.1) will be aligned. The disk resonator in this particular device was 300 microns in diameter and extended beyond the edge of the insulating silica pad by more than a millimeter (please note that Fig. 4.1 is not drawn to scale). The two circles used as alignment marks are essentially two holes etched into the oxide. The last critical feature defined in this mask is the large silica pad upon which all the subsequent electrical contacts will be electroplated. By electroplating directly on top of the silica, it allows the entire device to be electrically isolated from the rest of the wafer, thereby preventing accidental short circuits.

The wafer is exposed in the mask aligner for 30 seconds and then removed and placed in a dish containing MF-319 developer made by Shipley (Fig.4-2A). The exposed regions of the PR are developed away after one minute of submersion in the solution. Once the developing process is complete, the wafers are rinsed in DI water, blow dried using nitrogen, and baked a last time at 115ºC for two minutes. This baking step is important for two reasons: it evaporates any remaining solvent in the PR, further hardening it and making more it resilient in the buffered HF etchant. It also slightly reflows the PR, smoothing out some of the roughness visible in the periphery. When the baking is complete, the wafer is removed from the hotplate and allowed to cool for one minute, and is then placed in a Teflon beaker containing buffered HF etchant. The buffered HF etches the silica at a rate of approximately 1000 angstroms per minute; as a result the wafer must remain in the solution for 20 minutes until the exposed regions of silica are completely removed (Fig.4-2B). The wafer is then removed from the buffered HF solution, rinsed with DI water, and blow dried. Next, the remaining PR is removed from the surface of the wafer using a rinse of acetone, IPA, DI water and finally blow dried (Fig.4-2C). The wafers at this point are left in a nitrogen purged desiccator for 24 hours in order to dehydrate the surface. Baking the wafers in air at even a modest temperature of 100ºC will result in the growth of a thin native oxide, which will result in rough silicon etching later in the process.

After removal from the desiccator, the wafer is again placed on the PR spin coater, and AZ 4620 (Clarient) is poured in the center half of the wafer. The spin coater is set to a relatively slow speed of 750 RPM, and the wafer is spun for 1-minute. While the wafer is

spinning, a cleanroom wipe is used to remove the PR forming a bead along the outer edge of the wafer. The PR used in this step is used to form thick layers (up to 24 microns) and thus has a low viscosity, when combined with a slow spin speed it results in a thick edge bead unless manually removed. Edge bead is of particular concern in this process because it makes subsequent mask aligning difficult if not impossible due to the inability to come into direct contact with the wafer surface. When the spin coating is complete, the wafer is placed on a hot plate, and the PR is baked at 90ºC for 1 minute and then removed to cool for another minute. This mask step is used to define the PR sacrificial layer[40, 41], and the spin coating process creates a PR layer that is12 microns thick. A sacrificial layer is necessary in the overall process for the same reason that the silicon was removed from the periphery of the microtoroid resonators in Chapter 2. Later in the process, electroplated nickel will be deposited that will support the disk, and therefore the nickel must come into direct contact with the disk. However, the only region where the nickel can contact the disk without concern for deleteriously effecting Q factor is in the central region of the disk. Therefore, mask 2 in this process (Figure 4.1) will simply leave behind a square pad of PR. Aside from that it contains two alignment marks (circles at the bottom) that match two circles on the first mask as well as a central hole through which the electroplated nickel will make contact with the disk. Once this sacrificial layer of PR is removed, the nickel arms are suspended above the edges of the microdisk, only directly contacting it in the center, well away from the whispering gallery modes (Fig. 4-10).

Then, in order to define the sacrificial layer, the wafer is again placed in the mask aligner with mask 2 and carefully aligned to the previous pattern. Once successfully aligned, the

wafer is brought into contact and exposed for 9 minutes. The wafer is removed from the mask aligner and placed in a beaker containing AZ 400K developer for approximately 3 minutes while the exposed regions of the PR are rinsed away (Fig.4-3A). As soon as the development is complete, the wafer is immediately rinsed with DI water and blow dried using nitrogen. The PR is baked one last time at 130ºC, driving any remaining solvent out and slightly reflowing the pattern. Reflow of the PR is needed in this step (much like mask 1) for a different reason. While edge smoothness is not of critical importance, the profile of the top surface of the PR pad must be rounded in order to ensure that metal is evenly evaporated during the next metallization step. By reflowing the PR, the steep edges of the PR holes become smooth and rounded.

Before any electroplating can be performed, a metal seed layer must be deposited. This layer will then be covered by a final patterned PR layer that will be used as an electroforming mask, forming the nickel based MEMS system (Fig.4-3B). The metal seed layer is composed of 200 angstroms of chrome immediately followed by another 400 angstroms of gold, both of which are deposited via thermal evaporation at a rate of approximately 20 angstroms per second. It should be noted that the post-development bake for the sacrificial PR layer is critical to ensure that bubbles do not form in the PR under the metal, thus making subsequent lithography impossible.

The last photolithography step will be used to define the electroforming mask used during the nickel electroplating[42-44]. The thickness of the nickel that can controllably be electroplated into the mold is dictated by the thickness of the PR. Therefore, the same

type of PR used during mask 2 is utilized once again in order to form a 12 micron thick electroforming mold into which the metal will be electroplated. The same procedure as used during mask 2 is performed in order to spin coat, expose, and develop in order to pattern the third and final PR layer (Fig.4-4A). Once the development is complete, the entire wafer is placed in an oven at 80ºC for 5 minutes allowing the PR electroforming mold to harden. The wafer is now ready for the nickel electroplating process[45].

Electroplating was performed inside a beaker containing an anode, cathode, and aqueous-metal solution, and was connected to the power supply and current meter (Figure 4.6). In the simplified example shown in Figure 4.5, the sacrificial anode is made of nickel, the cathode is the wafer that is coated in gold, and the aqueous-metal solution consists of nickel (Ni^{2+}), hydrogen (H^{+}), and sulfate ions (SO_4^{2-}). Once voltage is applied, positive ions in the solution are attracted to the negatively biased cathode and nickel ions that reach the cathode, gain electrons, and are deposited or plated onto the surface of the cathode forming the electrodeposit. Nickel is also simultaneously being electrochemically etched from the nickel anode to replenish ions for the aqueous solution and electrons for the power supply. Hydrogen ions that also gain electrons from the cathode form bubbles of hydrogen gas[46, 47]. Formation of hydrogen gas is not desirable because it lowers the plating efficiency (i.e., only a fraction of the total current is used to form the electrodeposit), and the bubbles can obstruct the deposition of the intended electrodeposit. The electroplating bath used for device fabrication, Nickel "S" Sulfamate electroplating solution, is an industrial ready-to-use solution made by Technic Inc. All plating parameters, such as the plating current, were optimized for the sole purpose of

depositing a stress-free nickel layer. This was important in order to ensure that the micropositioning arms were as flat and horizontal as possible. Based on the recommended plating conditions provided by Technic, a current of 10 mA/cm^2 was used during the plating process. However, the plating was actually performed in a two-step process. When the wafer was first immersed into the plating solution, the current was set to 200 mA/cm^2 for 30 seconds in order to "strike" the nickel into the gold seed layer. This process allows for nickel ions to bury themselves within the first few atomic layers of the gold seed layer thereby dramatically improving the adhesion between the nickel and the seed layer. After the 30 seconds elapsed, the current density was reduced back to 10 mA/cm^2 over the course of one minute to ensure a stress free nickel deposition.

4.3 Device Release

In order to fully release the MEMS arms and prepare the device for characterization, a series of etch steps must be carefully followed. First, the PR mask used as the electroforming mold must be removed, this is done by soaking the wafer in acetone for approximately 30 seconds then rinsing with IPA and DI water and blow drying with nitrogen(Fig. 4.4B). The next step is to remove the gold and chrome seed layers; great care must be taken in selecting proper etchants in order to avoid unintended etching of the nickel structures. Based on recommendations from Transene Inc. (Danvers, PA) it was suggested that GE-8148 be used to remove the gold and CRE-473 for the chrome adhesion layer. The wafer was first soaked in the gold etchant for approximately one minute then rinsed clean using DI water and blow dried. Next, the wafer is placed in the

chrome etchant for an additional four minutes then rinsed and dried again. The second to the last step is to remove the sacrificial PR with another soak in acetone, followed by a rinse in IPA and DI water. The wafer is then blow dried and finally placed in the xenon difluoride etching system in order to undercut and fully release the nickel micropositioning arm (Fig. 4.4B).

4.4 Device Control and Characterization

Testing of the devices required measurement of a variety of different parameters that included mechanical, electrical, and optical. Before the devices were mounted for testing, wires were soldered to the electrical contacts on the chip in order to run the current needed for tuning and positioning. When the four wires necessary were soldered in place, the entire chip was placed on an X-Y-Z micrometer stage in order to bring it within close proximity of the taper waveguide. This had to be done for two reasons. First, the device does not currently have Z-positioning control on-chip, therefore it can not control the vertical distance between the microresonator and the taper. Second, the on-chip lateral control or X-positioning is limited to only a few microns and is meant to control coupling between the taper and microresonator with nanometer resolution. Once the device was properly positioned, current was run through the positioning arms while the laser scanned for resonances.

Although the micropositioning system functioned, there are slight issues that made it difficult if not impossible to measure coupling as a function of applied voltage, the details

of which will be explained later. However, the frequency response of the device was successfully measured to be approximately 10 Hz (Fig. 4-11). This was done by running current through the serpentine tuning arms that directly heated the microresonator (Fig. 4-7).

The highest Q factor measured for the devices was approximately 1 X 10^4, relatively low when compared to results described in Chap. 2 for microdisk resonators. The low Q factors are the result of two factors. First, the masks used in the MEMS fabrication process are printed using a laser plotter with a maximum resolution of only 20,000 DPI, in reality the smallest feature sizes are approximately 10-microns. Therefore, the microdisk resonators in the MEMS devices suffer from lithographic blemishes nearly a factor of ten greater then the microdisk resonators in Chap. 2 which were fabricated using a mask written with an electron beam. Second, the only means by which the sacrificial layer of PR can be removed is by acetone rinse. However a much better method to ensure that this layer is completely removed is using an oxygen plasma to ash off any remaining PR. Therefore, if an improved mask were used to define the oxide disks and if the sacrificial PR were more vigorously and thoroughly removed, Q factors as high as 3-million could be expected from future devices.

Finally, in the process of attempting to measure coupling versus applied voltage to determine the effectiveness of the micropositioning system it was determined that two effects were taking place making this measurement impossible. The nickel micropositioning arm is actuated by applying a voltage that in turn ohmically heats the

arm and as a result it expands[48, 49]. Therefore by varying the amplitude of the input voltage, it is possible to control the horizontal displacement of the arm. However, this type of thermal actuation has two major drawbacks when used in an optical device that employs silica. Inevitably heat from the nickel micropositioning arm will affect the silica disk and tune the resonances much like the device demonstrated in Chap. 3. As a result, the resonances of the microdisk shift as a function of displacement. Secondly, due to slight imperfections in the mechanical structure of the device, the thermally induced deflection is not perfectly horizontal. During testing it became apparent that the microdisk had a slight vertical deflection on the order of a few microns when current was applied. These two effects when coupled to one another made it impossible to measure coupling between the microdisk resonator and the tapered fiber waveguide as a function of applied voltage.

4.5 Conclusion and Outlook

Despite the inability to control coupling while simultaneously monitoring an optical resonance, the overall device remains a successful proof of concept. Namely, the fabrication procedures were successfully demonstrated, and a much better understanding of the necessary device mechanics and geometry was determined. Needless to say, however, major improvements will be incorporated in the next generation of devices that are to be fabricated shortly after the completion of this thesis. Aside from improving particular processing steps, major changes in the design of the positioning system will also be implemented. Rather than continuing with the thermal expansion of the nickel

arms to drive the positioning, comb-drives that utilize electrostatic forces[40] will instead be used. The primary benefit of the electrostatic drive mechanism is the lack of heat producing electric current[41, 46]. This will allow the device to position the microresonator without inadvertently tuning the microresonator due to stray heat. Lastly, it will further improve the resolution and range of the positioning system.

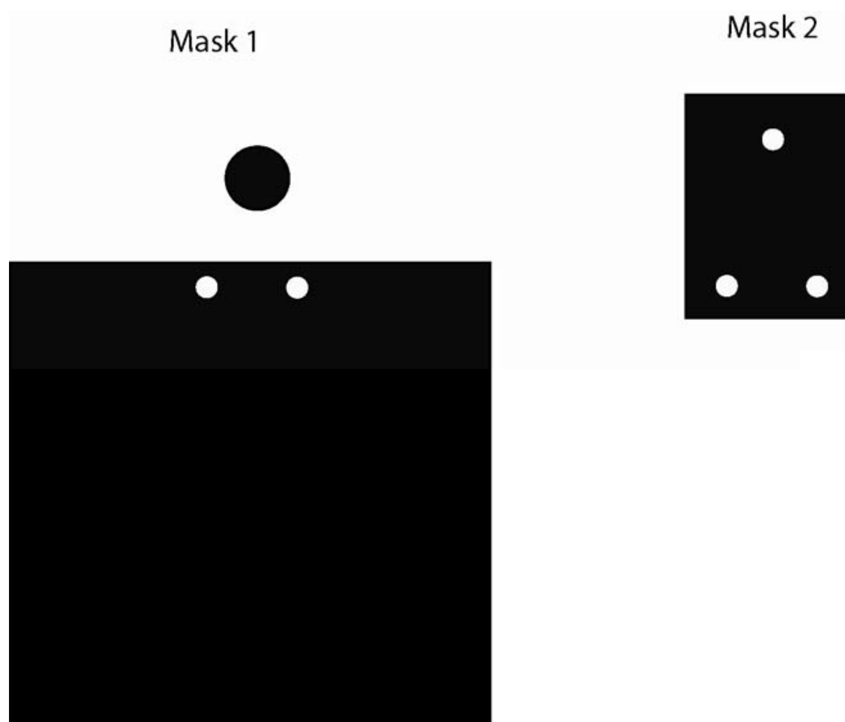

Figure 4-1: The first two masks used in the fabrication of the MEMS devices. Mask 1 is used to define and isolate the electrical contact area as well as define the silica disk and alignment mark. Mask 2 is used to define the sacrificial PR layer upon which the nickel is later electroplated.

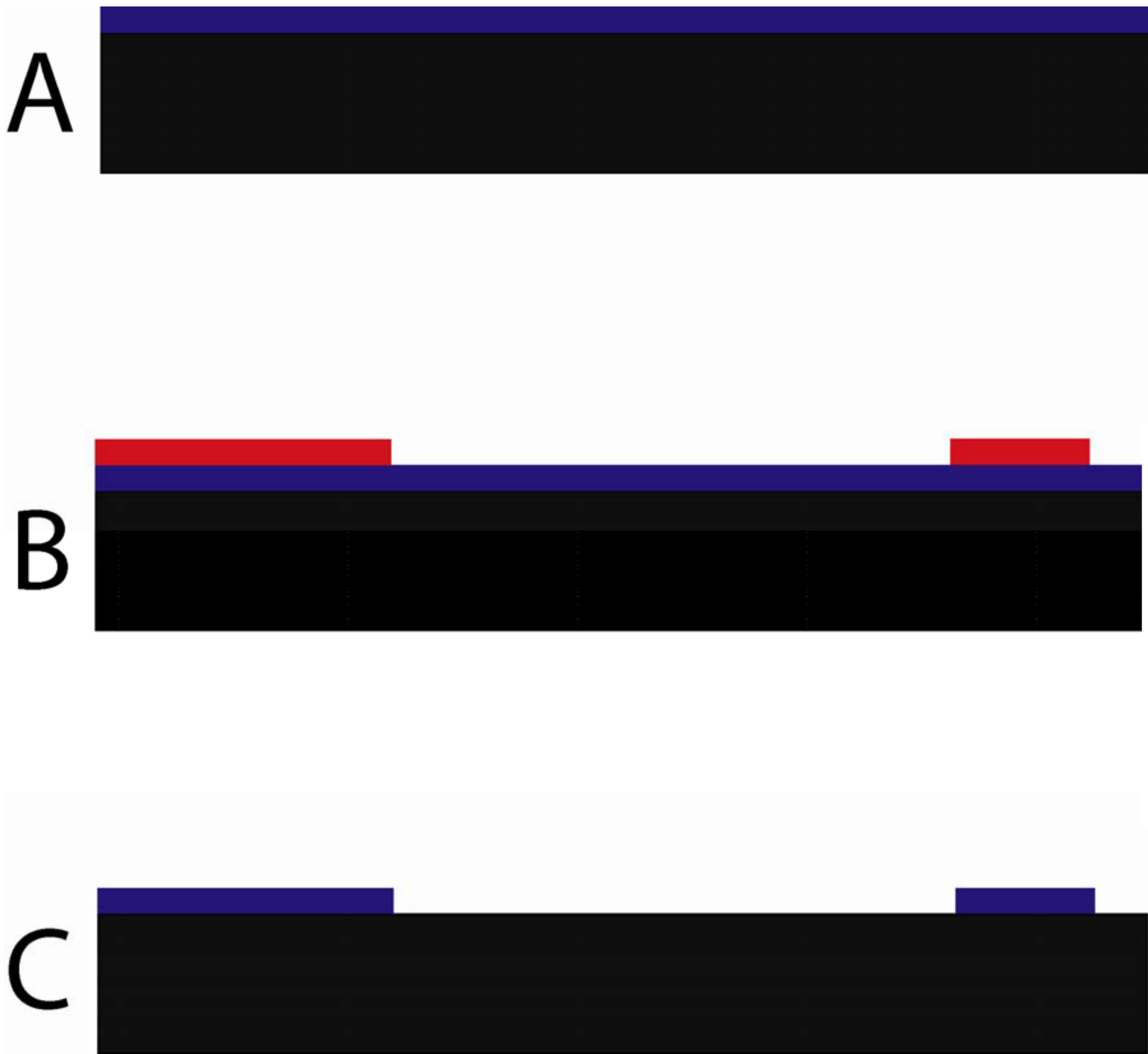

Figure 4-2: These are the three process steps associated with the first mask. A: The oxide wafer is degreased. B: PR is spin coated and patterned. C: The silica is patterned and the PR removed.

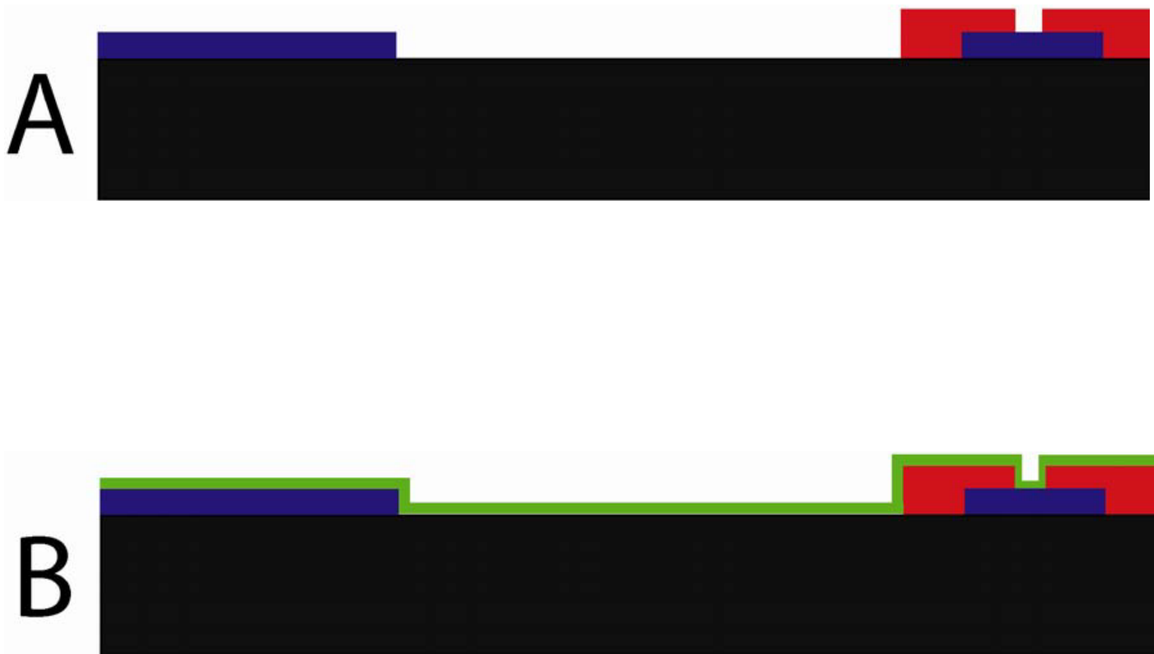

Figure 4-3: These are the two process steps associated with the second mask. A: The thick PR layer is spin coated and patterned; this layer will act as a sacrificial layer during later processing. B: A thin layer of chrome and gold are evaporated across the entire wafer; the metal will be used as the seed layer during electroplating.

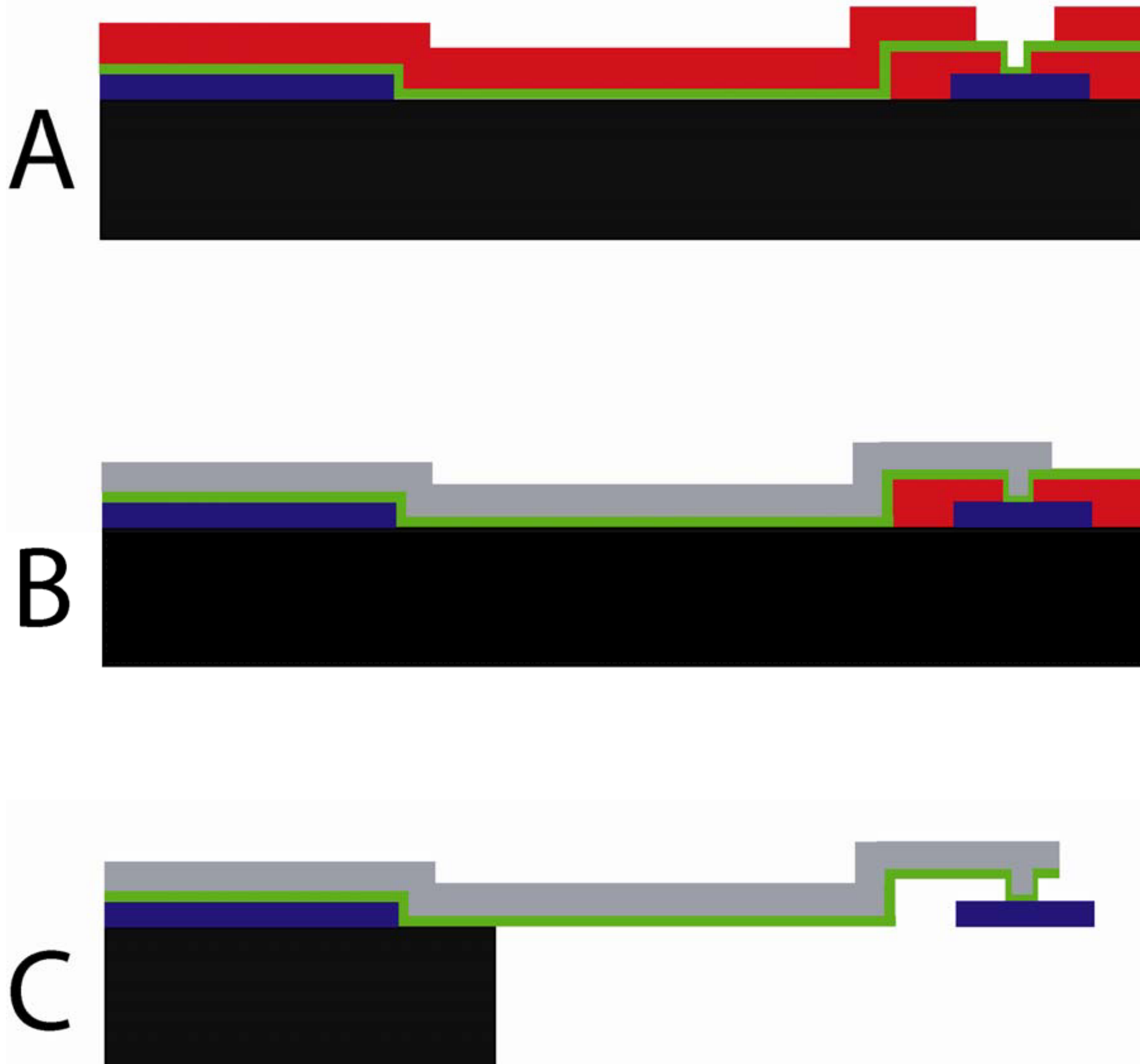

Figure 4-4: These are the three process steps associated with the third mask. A: The final PR layer is spin coated and patterned; this layer is used as a mold during the nickel electroplating process. B: The PR mold is carefully removed using acetone and DI water. C: The exposed regions of the chrome/gold seed layer are removed, the sacrificial PR layer is rinsed away, and the entire chip is etched using XeF_2 in order to release the micropositioning arm.

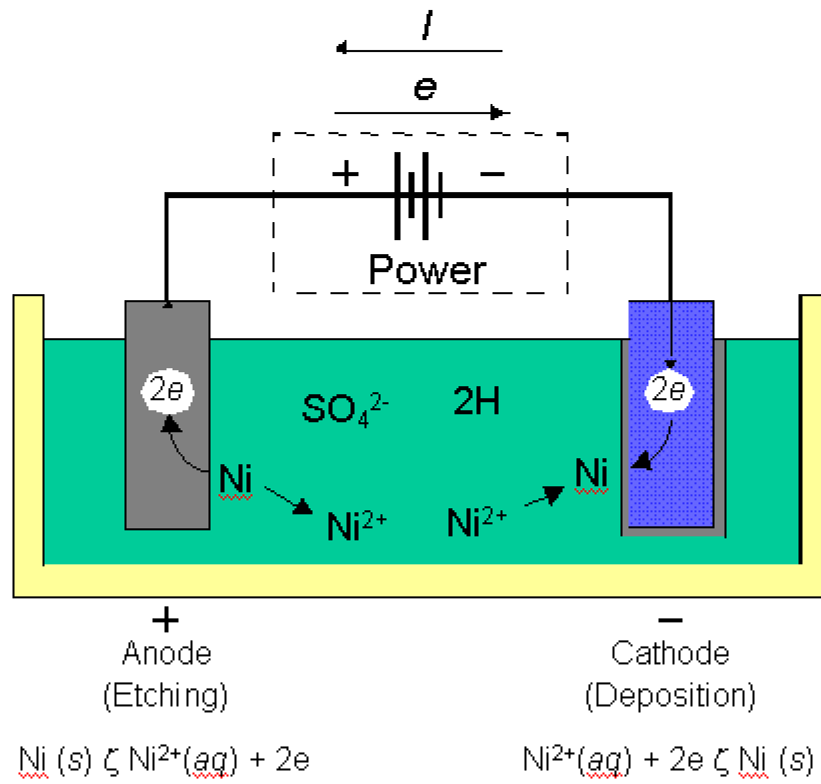

Figure 4-5: A schematic representation of the nickel electroplating setup.

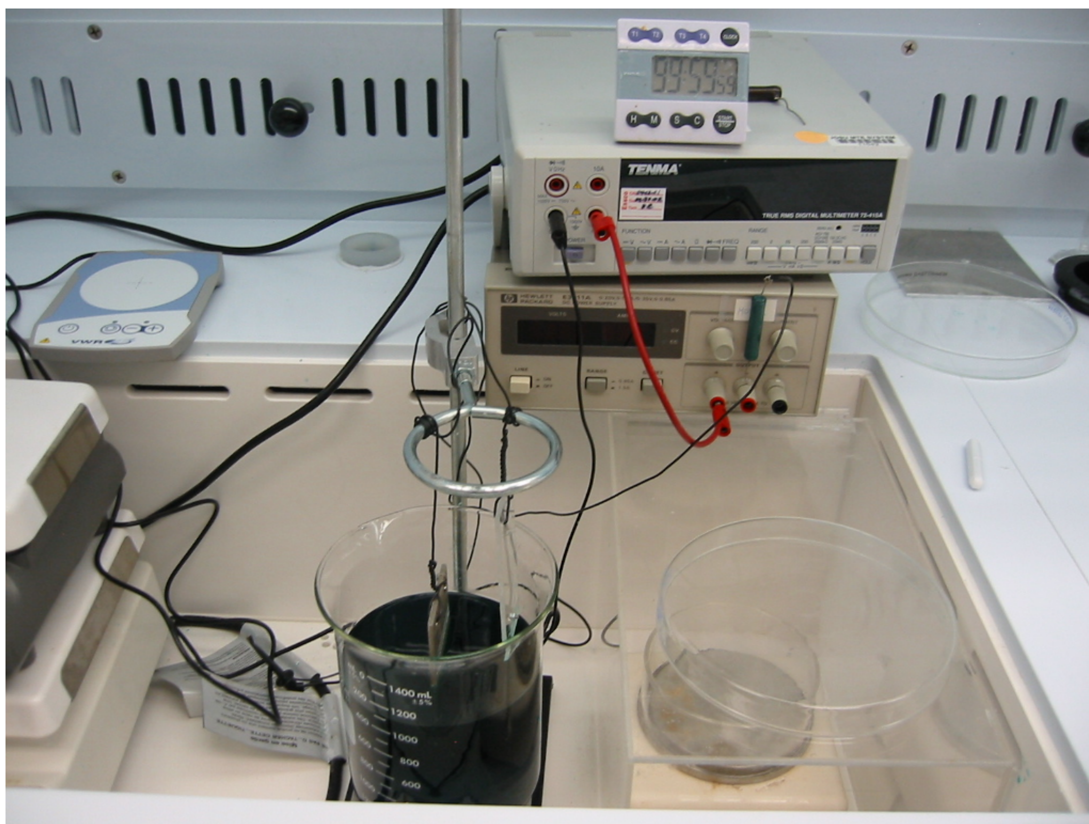

Figure 4-6: The nickel electroplating setup currently used in the Vahala cleanroom.

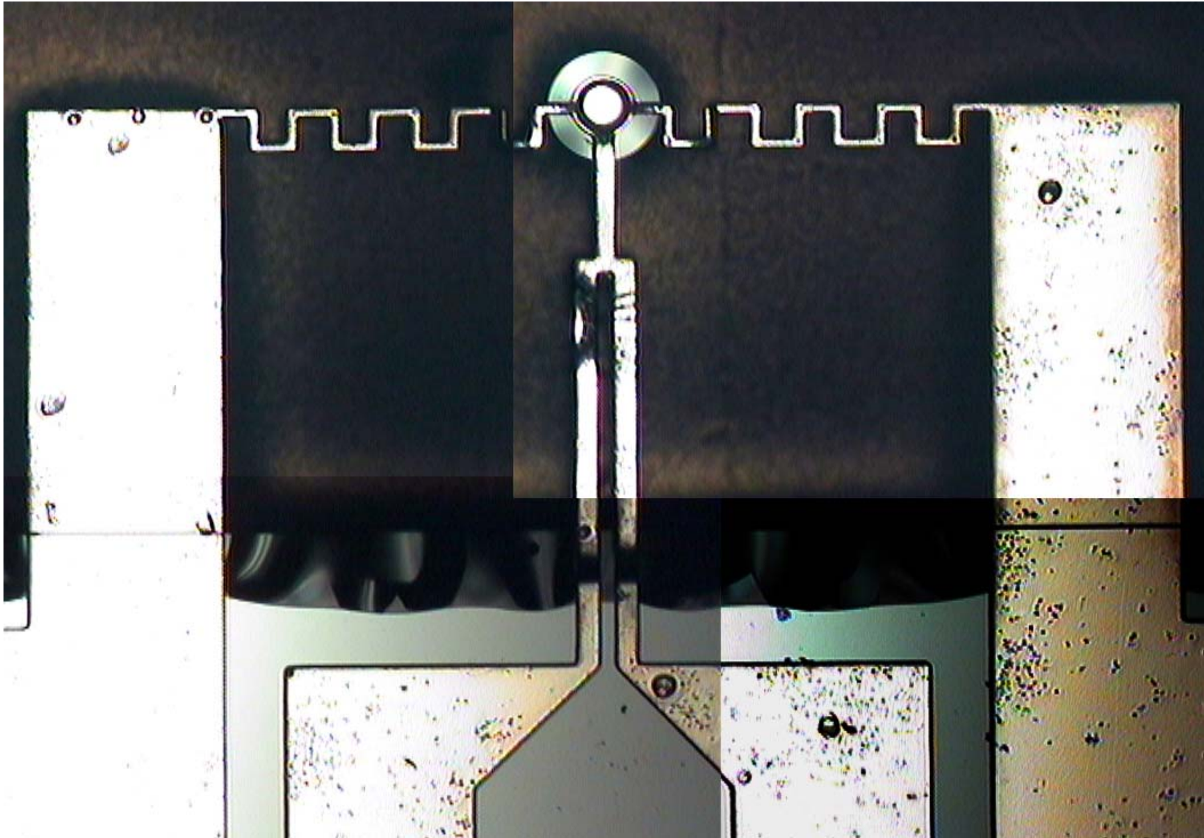

Figure 4-7: A compound optical micrograph taken from the top view of the MEMS device. The serpentine arms are used as a heating element to tune the disk as well as a mechanical stabilizer ensuring that movement is horizontally restricted. The center fork is used to move the disk, to which the disk is attached by a single beam.

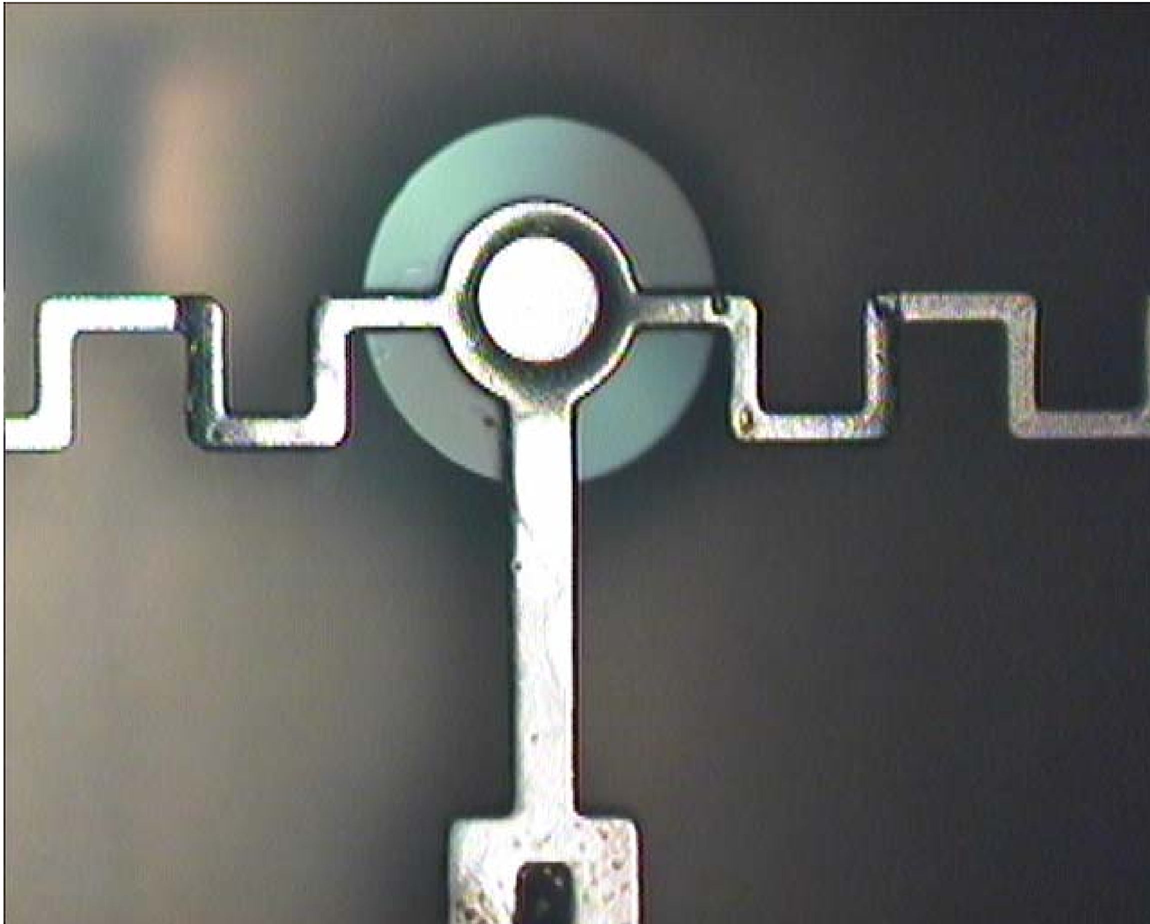

Figure 4-8: Close up top view of the microdisk and MEMS positioning arm.

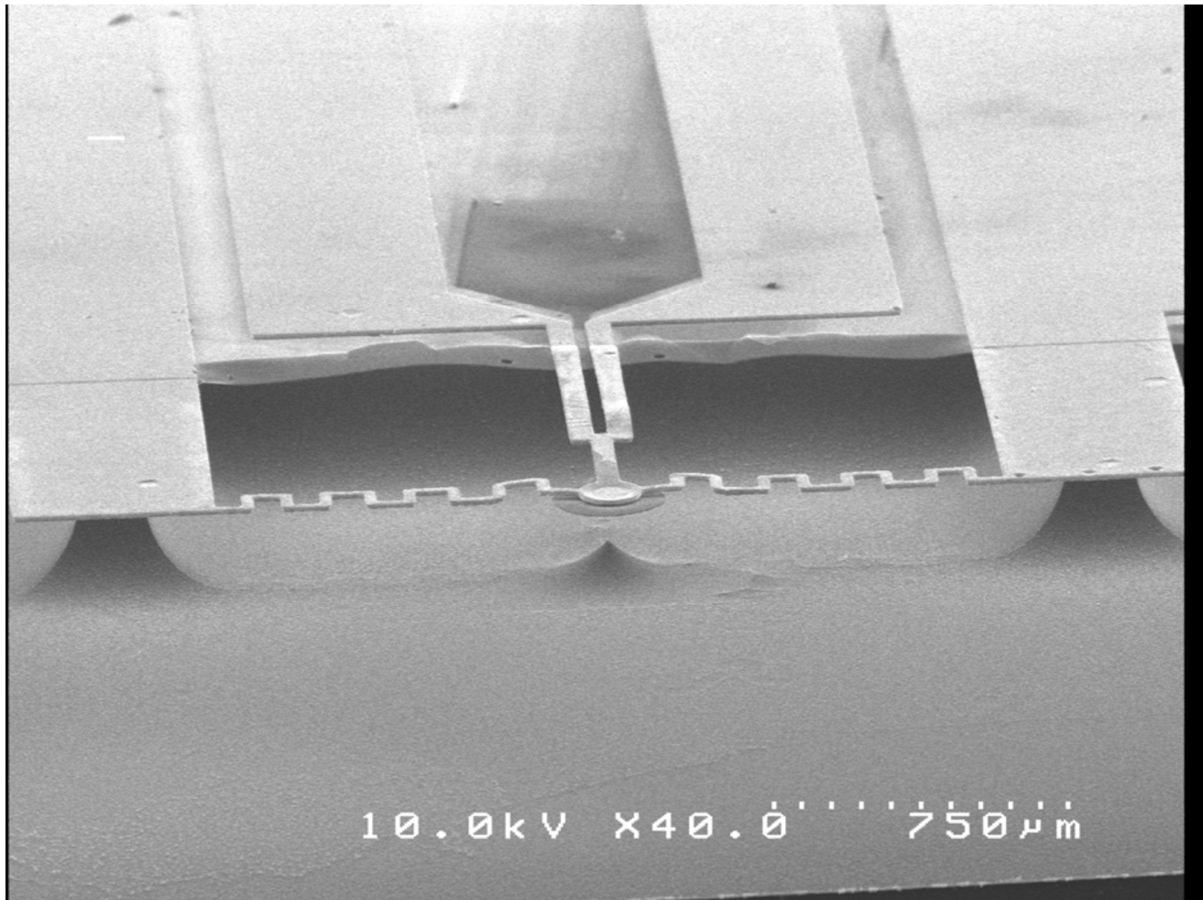

Figure 4-9: Scanning electron-micrograph of the MEMS positioning system.

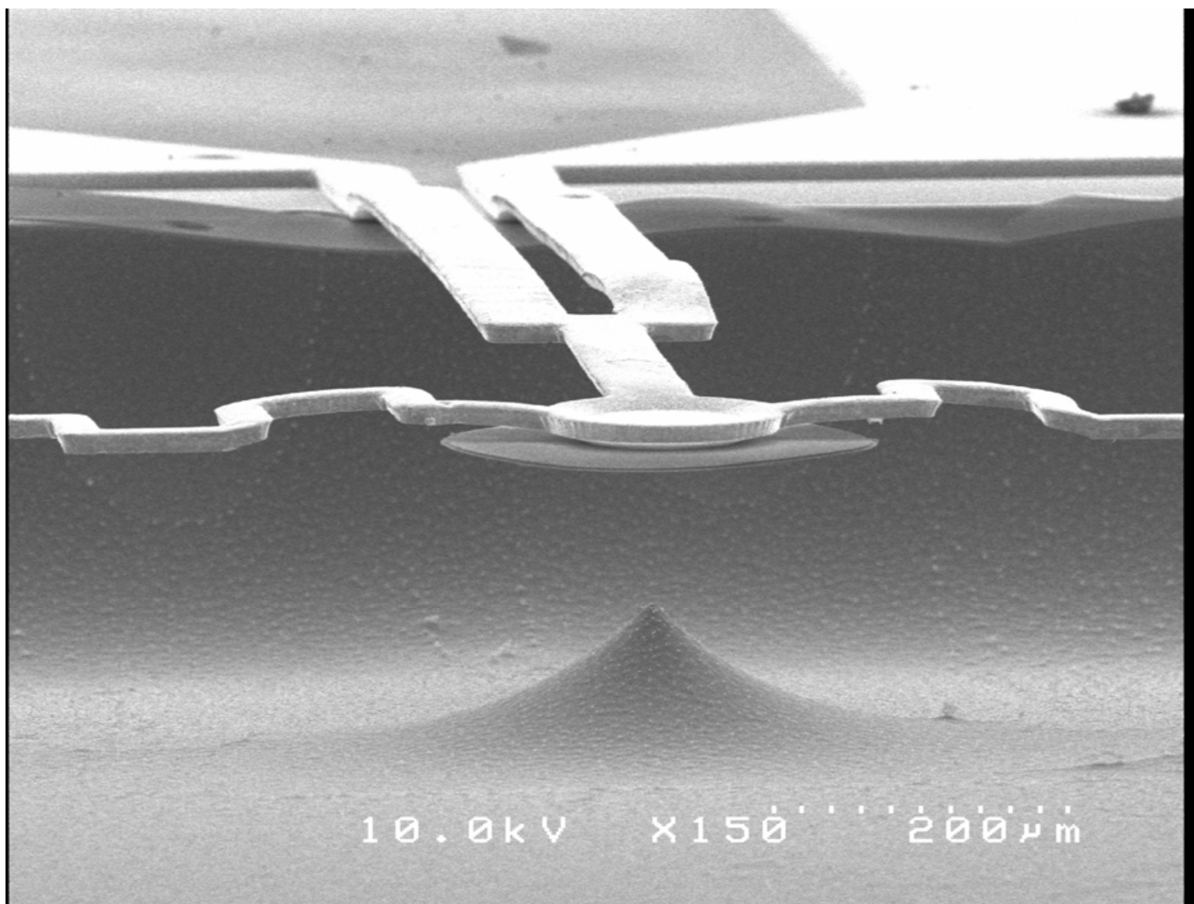

Figure 4-10: Close up of the microdisk; note the stress induced warping of the device.

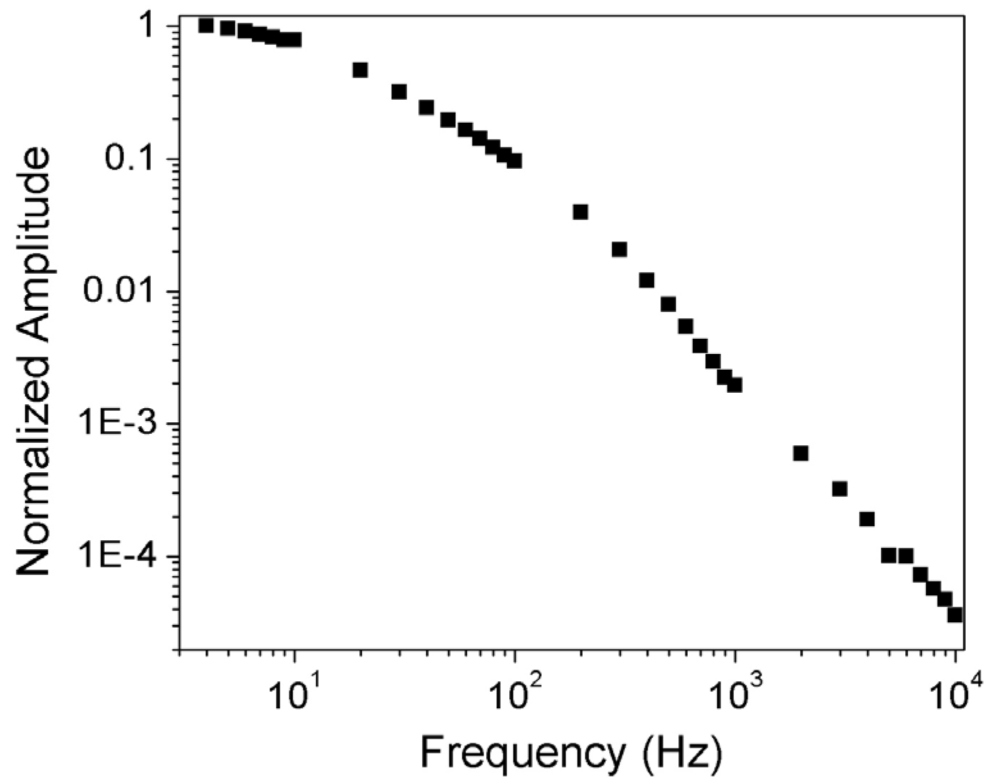

Figure 4-11: Frequency tuning response of the microdisk. The tuning is the result of ohmic heating from the serpentine whiskers attached to the microdisk.

Chapter 5 - Replica Molded Polymer Microtoroid Resonators

5.1 Introduction

Resonant microcavities have a variety of applications in fields such as nonlinear optics[6, 7] biosensing[8], and telecommunications[30]. However, the fabrication protocols for these devices, as is typical in all device microfabrication, are material specific. In this chapter, the ultra-high-Q whispering-gallery type microresonators[33] described in Chap. 2 are utilized as masters in a novel application of micromolding. In addition to being a fast and effective method of producing high-Q polymer microresonators, the process is capable of producing resonators that are material loss limited. As such, it has a secondary application for rapid evaluation of optical loss in previously untested polymers. To illustrate this application, both polydimethylsiloxane (PDMS) and Vicast (a polymer heretofore known only in household and consumer applications) are evaluated at several wavelength bands. In addition to producing record Q factors for polymer-based microresonators, Vicast is found to facilitate resonator storage in the mold until time of application.

5.2 Fabrication

The replica molding process consists of 3 major steps as shown in Figure 5-1. First an array of ultra-high-Q silica microtoroid masters is prepared according to the procedure described elsewhere[50]. A polydimethylsiloxane (PDMS) mold is then made of the

microtoroid array, and finally, PDMS or Vicast replicas are cast from the mold. The molding process is similar to that used in previous microfluidic[51-53] and photonic device work[25, 54]. Because the present structures feature a relatively large overhang (Figure 5-2) and contain both a silica and silicon surface, the negative-mold polymer must be both mechanically flexible and not adhere to either the silica or silicon. PDMS (RTV 184, Dow Corning 10:1), a silicone elastomer, was found to satisfy these requirements.

To prevent adhesion between the PDMS and the silica master toroids, the microtoroid master arrays are silanized with trichloromethylsilane (TCMS). After silanization, PDMS is poured onto the microtoroid master and de-aired at 200 mTorr for 30 minutes. Once the de-airing process is complete, the mold is cured for 60 minutes at 80ºC. To remove residue water or HCl from the PDMS surface and to complete the curing process, the mold is baked for 12 hours after release from the microtoroid master.

Replica resonators were cast using two different polymers, PDMS and Vicast (AOC, 100:1). Optical devices, such as waveguides, have been molded from PDMS previously. However, Vicast has never been used for optical device fabrication nor have its optical properties been characterized. While both polymers are optically transparent, the mechanical properties are significantly different. However, the flexibility of the PDMS mold allows for the rigid Vicast microtoroids to be cast.

In casting PDMS-based microtoroids, the mold is first treated with oxygen plasma for 20minutes to facilitate removal of the polymer microtoroid replica from the PDMS mold. After de-airing, the liquid PDMS is cured for one hour at 80ºC and released from the mold (Figure 5-3). The casting procedure for Vicast microtoroids omits the oxygen plasma treatment. However, Vicast must be cured for 12 hours at 75ºC and remain in the mold for an additional 48 hours at room temperature before release (Figure 5-4).

It should be noted that each step of the PDMS and Vicast polymer replica fabrication process is non-destructive. Microtoroid masters and the PDMS negative molds were used repeatedly and no degradation in quality (as inferred by measurement of resonator Q factor) was observed in the final polymer replicas. In addition, Vicast microtoroids have been stored for several weeks in-the-mold without adhering to the mold and exhibit Q factors comparable to Vicast microtoroids immediately released from their molds. Since high-Q microresonators can be sensitive to long term environmental exposure, this feature is an important means by which the “shelf-life” of disposable microresonators can be increased.

5.3 Characterization

Measurement of the resonator quality factor and analysis of the modal structure was performed at three wavelength bands (980 nm, 1300 nm, and 1500 nm). For testing purposes, a single-frequency, tunable external-cavity laser was coupled to a single-mode optical fiber containing a short, tapered section. The tapered section was used to couple

power into the “whispering gallery modes” of the PDMS and Vicast microtoroids. Tapered fibers are made by heating a standard, telecommunication, optical fiber with an oxyhydric torch while stretching the fiber[26]. They function as high-efficiency probes of microresonators and are described in more detail elsewhere[34, 55]. During testing, the polymer microtoroids were placed on a high-resolution translation stage (100-nm step resolution) and were monitored by two cameras (top and side view) simultaneously. With the taper waveguide in close proximity to the polymer microtoroid, optical laser power was launched and transmission spectra monitored. Figure 5-5 is a typical transmission spectrum. Since the refractive index of both PDMS and Vicast are similar to that of silica (PDMS:1.46 and Vicast:1.53 near 1300), both the modal structure and free-spectral-range of the polymer microtoroids are comparable to that of their silica master counterparts. Furthermore, the modal structure is dominated by principal transmission minima believed to be the fundamental transverse mode of the replica microtoroids.

The intrinsic Q factor for this mode was determined by scanning the laser (linewidth of 300 kHz) and measuring the transmission and the loaded linewidth (full-width-half-maximum) for several, waveguide-resonator, coupling conditions in the under-coupled regime14. The intrinsic modal linewidth (and intrinsic Q) was then computed using a simple coupling model. In order to minimize the effect of thermal distortion on the mode structure the optical input power was kept below 1-microwatt using an optical attenuator and the laser scan frequency was optimized so as to ensure that neither scan direction (increasing frequency vs. decreasing frequency) nor scan frequency had any observable impact on linewidth. The measured intrinsic Q factor (average of computed values

described above) for both Vicast and for PDMS in all wavelength bands tested is given in Figures 5-6, 5-7, and 5-8. Points in the plot are located at wavelengths corresponding to specific modes measured while the curves provide a guide to the eye. The data is specific to one device, but is representative of measurements on many distinct polymer resonators. Maximum quality factors of 5×10^{6} were measured for Vicast and 2×10^{6} for PDMS. Comparing these results to all other chip-based, microresonator Q values, the maximum Q factor measured for the Vicast microtoroids is bettered only by the silica microtoroid master and is nearly a factor of 40 greater than all prior polymer-based devices (highest Q previously reported in ref. [56]).

The material-limited maximum Q factors for PDMS are also presented in Figures 5-6, 5-7, and 5-8 and were inferred using available absorption spectra[57, 58]. Both the magnitude and the spectral dependence of the measured, intrinsic Q factors are consistent with the inferred curves for PDMS, indicating that cavity Q is dominated by material loss and not surface scattering. The PDMS and Vicast material loss was also measured at 1319 nm and 1550 nm using a Metricon system, a prism coupling measurement using planar waveguides. The Metricon PDMS absorption values were compared with the published PDMS absorption spectra and indicate that the measured loss was bulk absorption (not waveguide scattering) limited. The Metricon derived data point for Vicast gave a material-limited Q factor of 2.71×10^{6} at 1319 nm and 3.11×10^{6} at 1550 nm, which are consistent with the measured intrinsic Q factors. Since the master microtoroids exhibit Q factors in excess of 100 million, the highest measured Q factor (5 million) provides a lower bound on the replication-process-induced Q degradation.

5.4 Conclusion

In summary, we have demonstrated both rigid and flexible replica-molded microresonators using ultra-high-Q microtoroid masters. Their Q factors are material-loss limited and typically in excess of 1 million. Q values in this regime and the ability to functionalize polymers[59, 60] for analyte-specific detection make these devices well suited for application as biosensor transducers and also for photonic devices requiring low insertion loss[61]. The micro-molding process lends itself to rapid, large-scale reproduction of dense arrays of devices, and optically active dopants[62] can be added directly to the host material. Additionally, by using Vicast as the replica polymer, we have shown that storage in-the-mold is possible and is a potential method to extend the shelf-life of the device. In applications requiring pristine optical interfaces such as biosensing, this feature and the inherently “disposable” nature of devices produced by replica molding are attractive features. Certain polymers, such as PMMA[63], are known to exhibit even lower material losses at shorter wavelengths. Using such polymers, replicated devices with Q factors in excess of 100 million, i.e., comparable to their masters, could be molded and used to probe nonlinear optical and thermo-optic tuning effects.

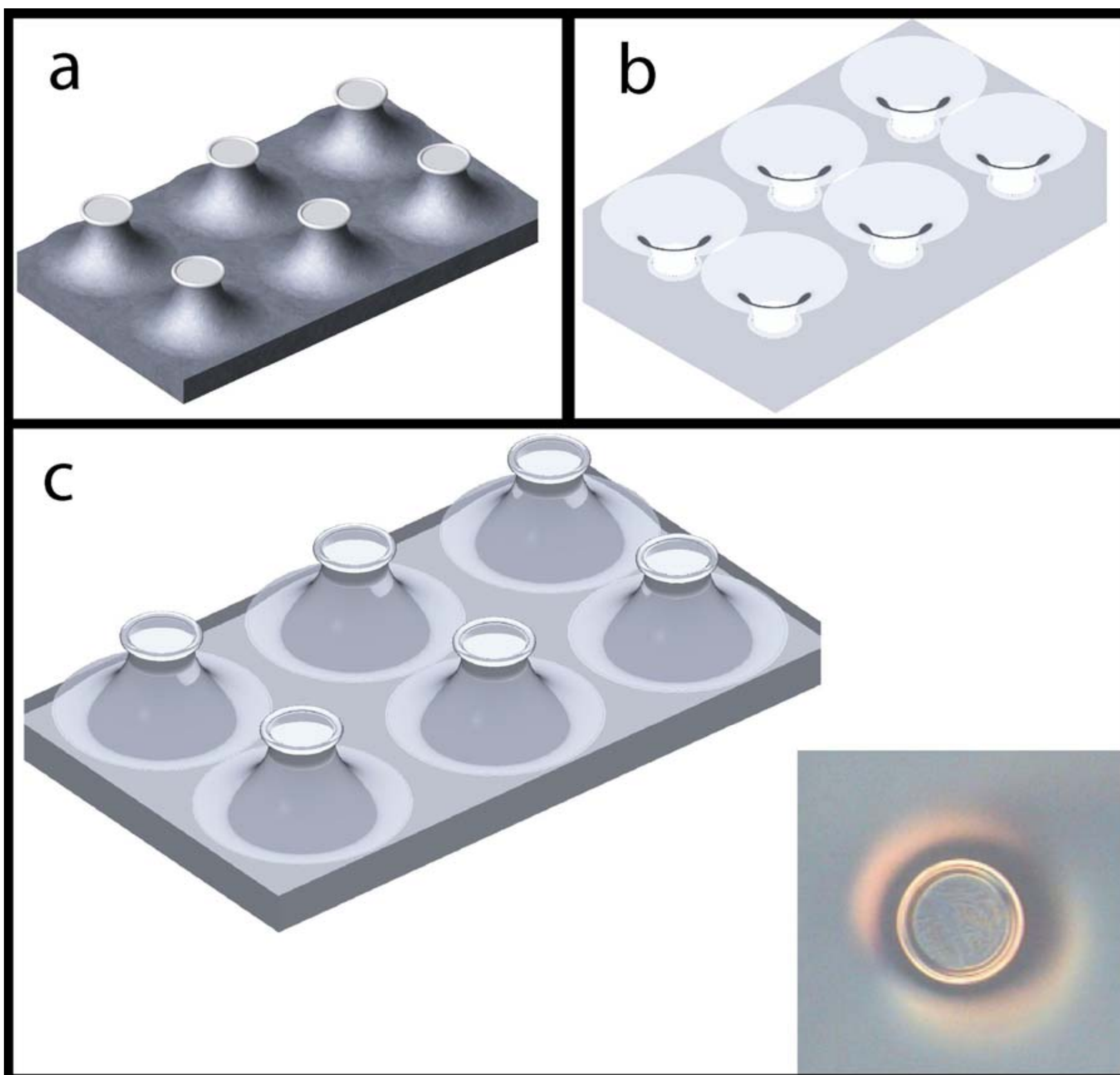

Figure 5-1: Replica molding process flow: a) ultra-high-Q microtoroid master array is fabricated and silanated with TCMS to aid in the release of the master from the mold; b) master is coated with PDMS to form PDMS mold, which is subsequently exposed to an oxygen plasma and filled with PDMS/Vicast to form c) PDMS/Vicast replica polymer microtoroid array. d) Optical micrograph of a PDMS microtoroid.

Figure 5-2: Cross-section of the PDMS mold, note the outline of the pillar as well as the toroid ring.

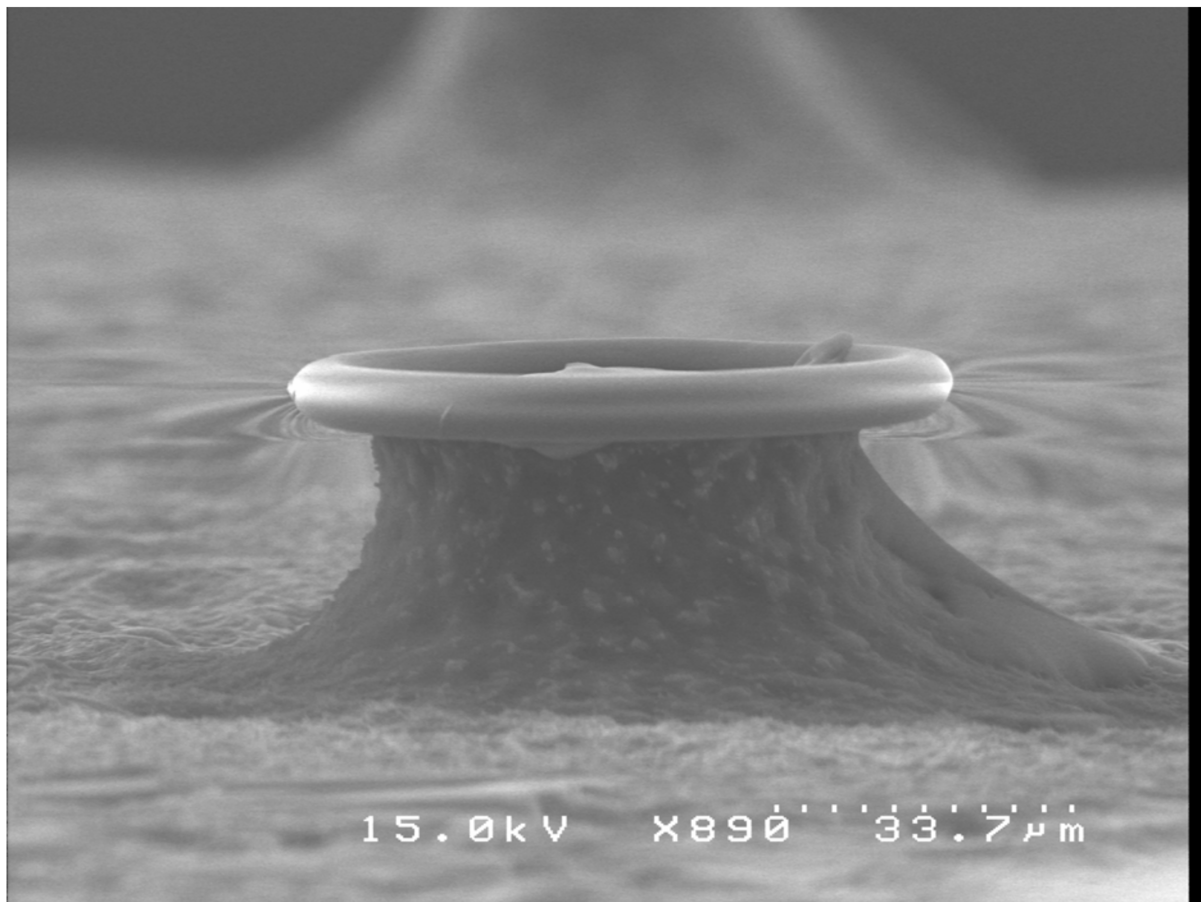

Figure 5-3: Scanning electron-micrograph of the first polymer microtoroid replica fabricated from PDMS.

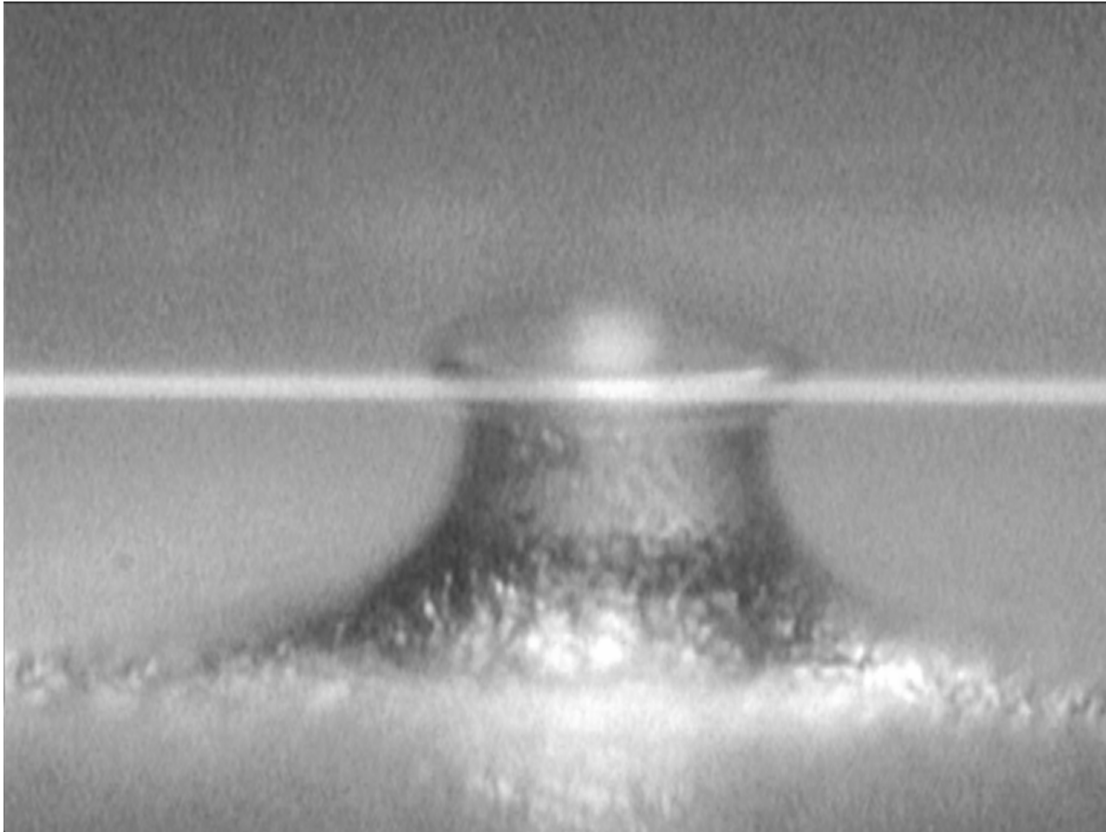

Figure 5-4: Side view of a Vicast microtroid replica shown while coupled to a tapered optical fiber.

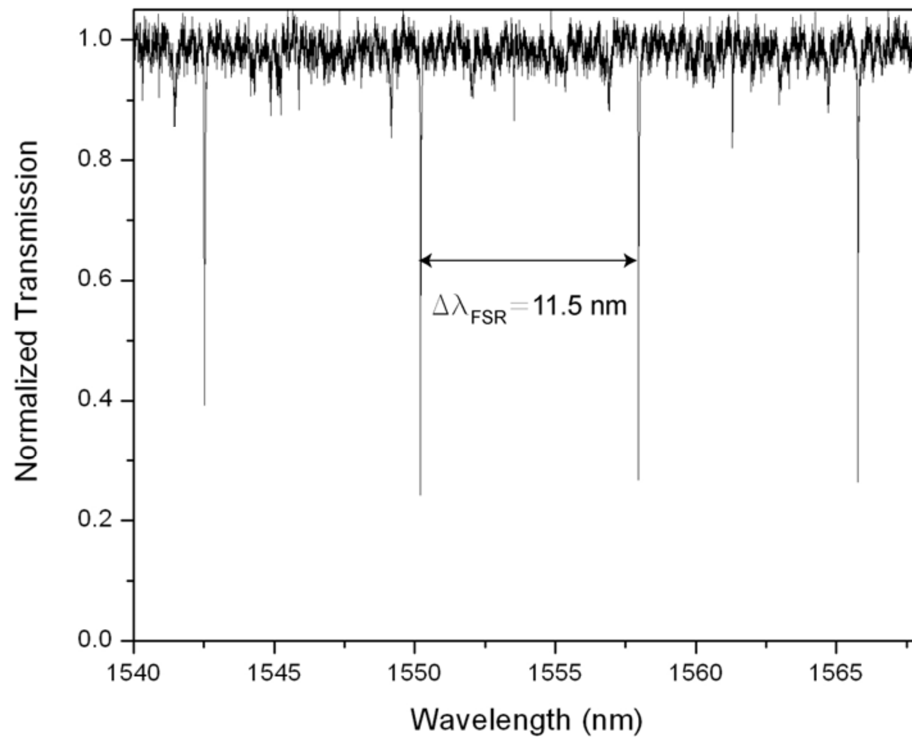

Figure 5-5: Transmission spectrum for a 45-micron diameter Vicast polymer microtoroid. The Free Spectral Range (FSR) of the polymer high Q microtoroid is in agreement with the theoretical prediction of 11.5 nm.

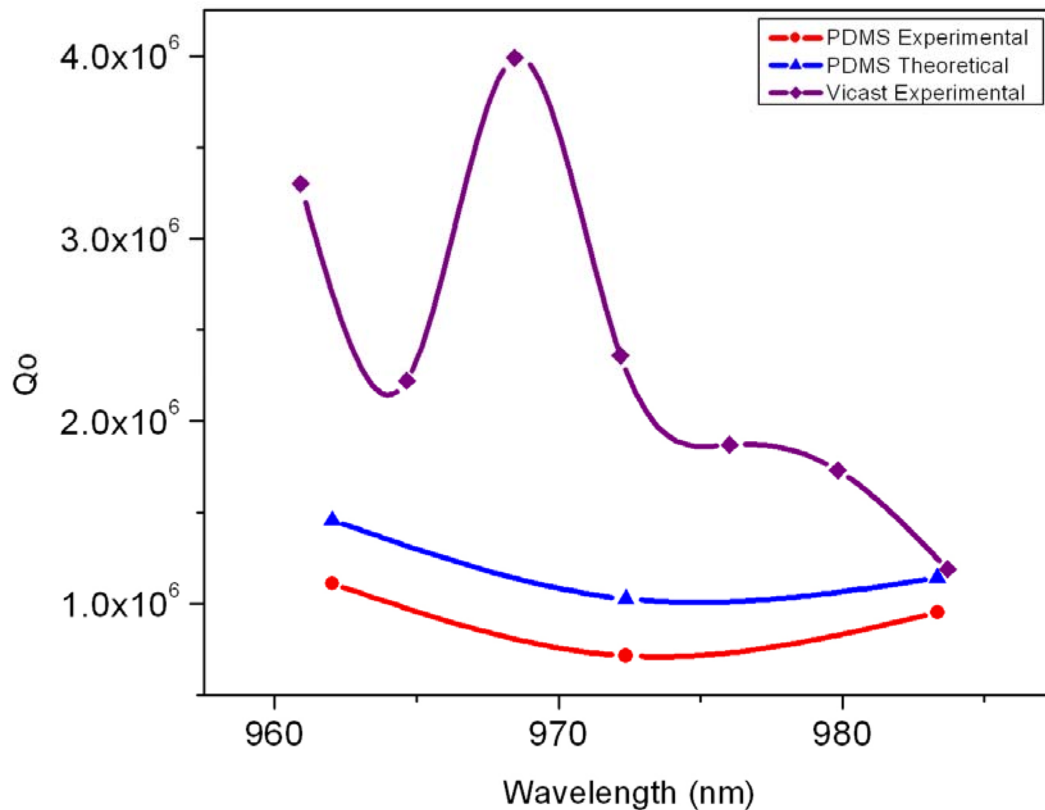

Figure 5-6: Intrinsic Q for PDMS (red circles) and for Vicast (purple squares) replicated microresonators measured in 980 nm band; the theoretical Q in PDMS (blue triangles) is also plotted. Data points are connected by curves as a guide to the eye.

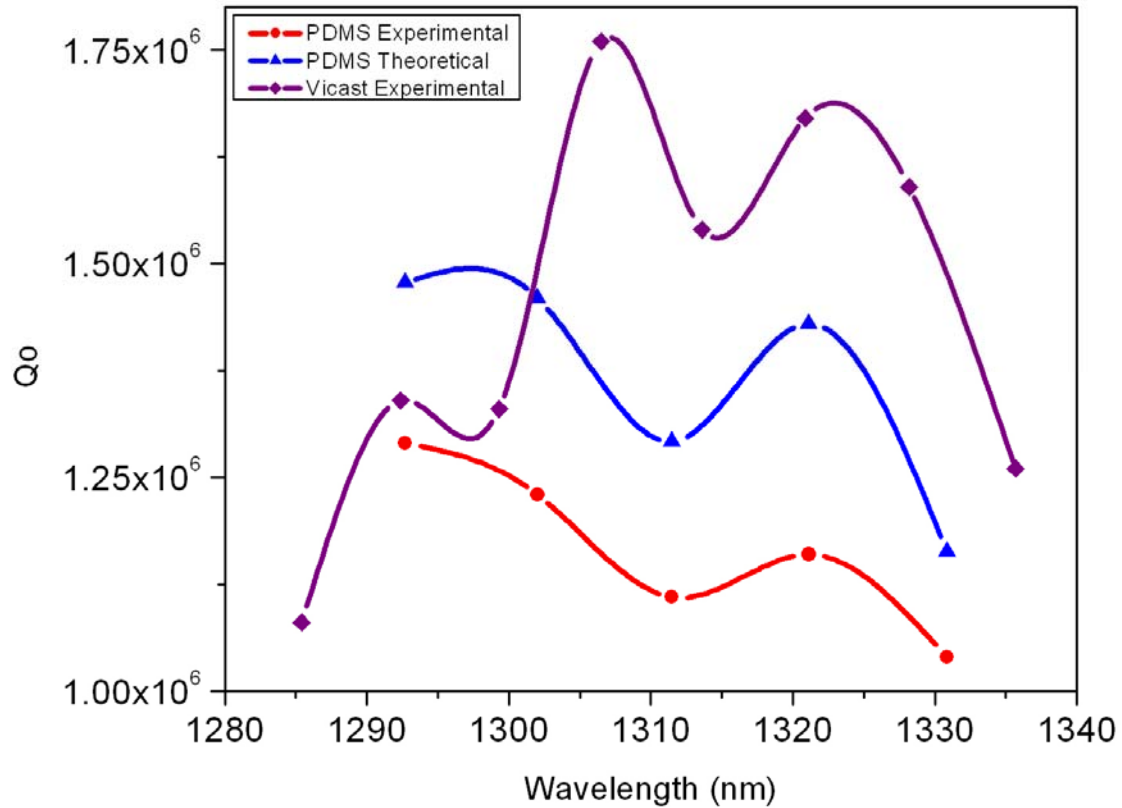

Figure 5-7: Intrinsic Q for PDMS (red circles) and for Vicast (purple squares) replicated microresonators measured in 1300 nm band, the theoretical Q in PDMS (blue triangles) is also plotted. Data points are connected by curves as a guide to the eye.

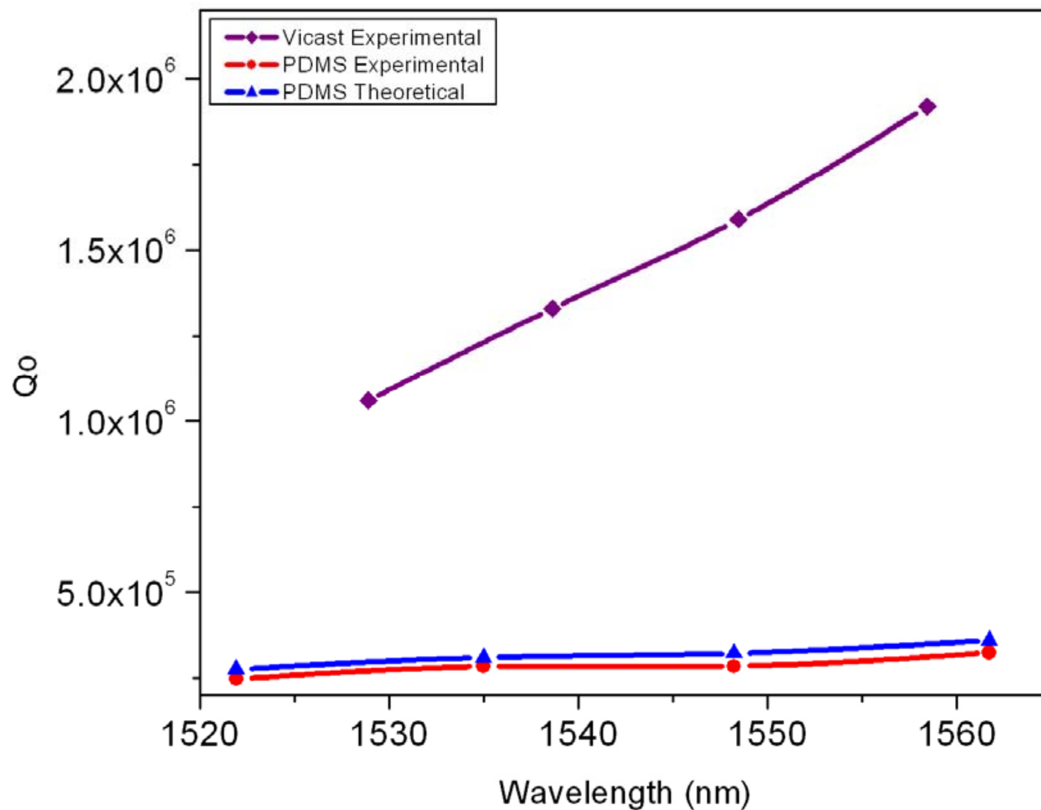

Figure 5-8: Intrinsic Q for PDMS (red circles) and for Vicast (purple squares) replicated microresonators measured in 1550 nm band, the theoretical Q in PDMS (blue triangles) is also plotted. Data points are connected by curves as a guide to the eye.

Chapter 6 - Surface Functionalization of Microtoroid Resonators with Erbium-Doped Sol-Gel

6.1 Introduction

In this chapter the surface functionalization of microtoroid devices using erbium-doped sol-gel films will be discussed. In addition to being integrable with other optical or electric components, they are directly coupled to optical fiber using fiber tapers. Sol-gel films were previously applied in order to surface functionalize silica microsphere resonators. Erbium-doped microlasers are especially interesting because their emission band falls in the important 1.5 μm window used for optical communications. While microsphere resonators are useful experimental tools in the laboratory they are not compatible with other optical or electronic chip based devices. Their properties are also difficult to control during fabrication. However, microtoroid based microlasers on a chip can be fabricated in parallel and their characteristic dimensions easily controlled using wafer-scale processing methods.

6.2 Fabrication

The details of the microtoroid fabrication process were described in Chapter 2, and the sol-gel starting solution was prepared as described in ref. [64]. Once the solution was prepared, it was aged for 10 hours at room temperature, and the silica microtoroids were then immersed in the solution for 3-5 hours. The substrate containing numerous microtoroids was heated in an oven at 160°C for another 10 hours in order to thoroughly

dehydrate the sol-gel. Microtoroids were then re-irradiated with a CO_2 laser (10.6 micron wavelength) in order to reflow and densify the sol-gel films. As described in Chapter 2, CO_2-laser emission is selectively absorbed by the silica layers. The combination of this effect and the relatively high thermal conductivity of silicon (100 times more thermally conductive than silica) results in the selective reflow and densification of sol-gel along the toroid periphery.

More importantly, sol-gel deposited in the central area of the microtoroid was unaffected by this process step. Moreover, the etch rate of sol-gel films in buffered HF acid is a function of densification temperature[65]. As a result, sol-gel deposited everywhere except the densified perimeter of the microtoroid was subsequently selectively removed (Figure 6-1). Microtoroids ranging in diameter from 60 to 85 μm were fabricated and the Er^{3+} concentration in the sol-gel layer was estimated to be around 10^{19} cm^{-3}. An important feature of gain functionalization of the surface is that it puts optical gain only where it is needed, i.e., where the best overlap is possible with the fundamental whispering gallery modes. Figure 3-1 illustrates both a sol-gel functionalized microtoroid and the taper coupling configuration used to both provide optical pumping and to extract laser optical power.

6.3 Characterization

The microlasers were optically pumped using a tunable, single-frequency, external-cavity laser operating in the 980 nm band and having a short-term linewidth less than 300 kHz. During testing, the sample chip was mounted upon a three-axis translator for position control. Two cameras were used to monitor the microtoroid samples and the taper, providing both horizontal and vertical views. The angle of the microtoroid relative to the taper was adjusted using the rotator to align the taper with the equatorial plane of the toroid. An optical spectrum analyzer (OSA) with resolution of 0.5 nm was used to measure the laser emission. A typical laser spectrum is presented in Figure 3-2. Single line emission within the resolution of the OSA was usually observed; however as pump powers increased, it was possible to induce oscillation in other longitudinal modes. To further resolve the single line observed in the OSA scan of Figure 3-2, a high finesse (~5000) Fabry–Perot etalon having a resolution of a few megahertz was also used to analyze the laser spectrum. A single-frequency, tunable, external-cavity laser emitting in the 1500 nm band with a known short term linewidth of 300 kHz was measured as a reference. Both spectra are presented in Figure 3-3. The measured laser output power plotted versus the absorbed pump power is shown in Figure 3-4. The threshold pump power in this data was 34 μW by extrapolation of the linear lasing region. The differential quantum efficiency was measured to be as high as 11% for single-mode, unidirectional operation. It should be noted that the power measurements were taken while microtoroids were in contact with the taper. While this allows for very stable coupling, it prevents the

optimization of the pump and emission coupling efficiencies. As a result, it is possible to further reduce the threshold in a more optimally coupled structure.

6.4 Conclusion

In summary, an erbium-doped microtoroid laser on a chip by use of a sol-gel surface functionalization technique has been demonstrated for the first time. Single-line laser emission and threshold pump powers as low as 34 μW were observed. Lastly, future devices will integrate additional functionality such as dynamic coupling and resonant control as described in Chapter 4 in order to create compact, low threshold laser sources in on-a-chip.

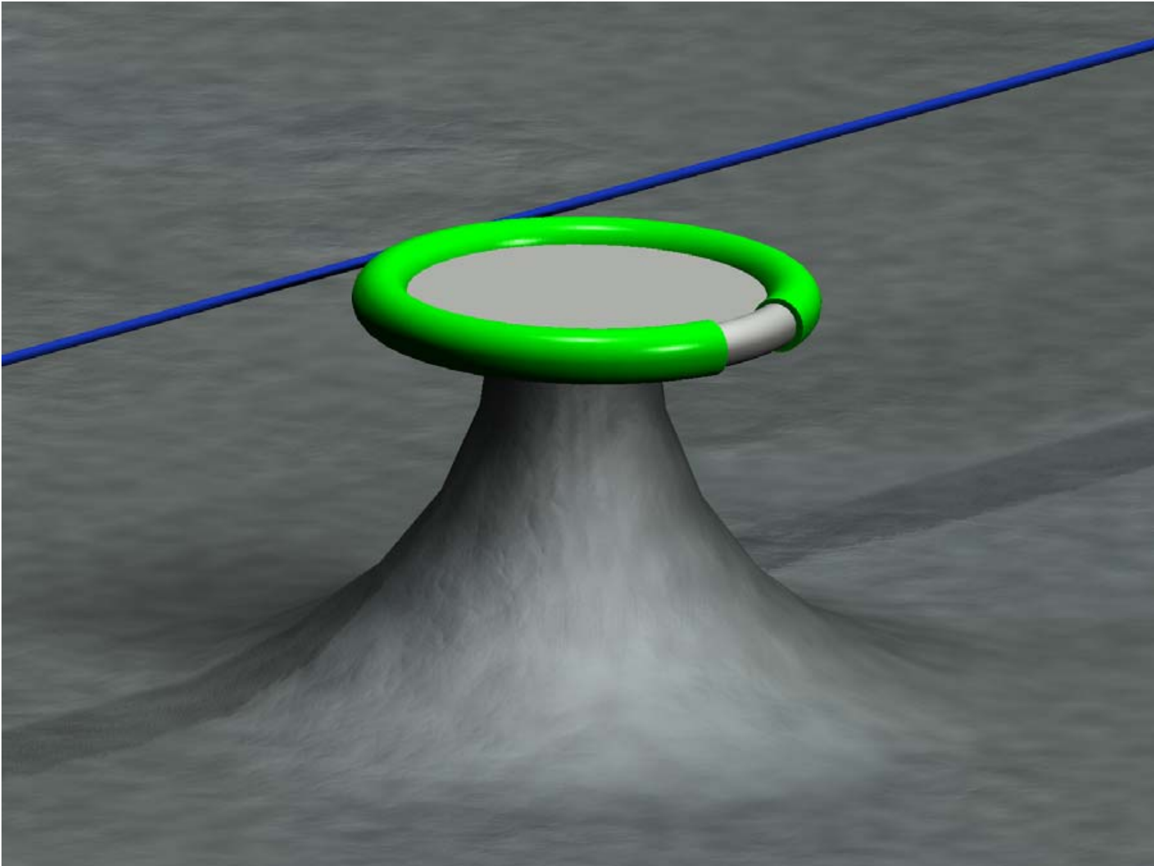

Figure 6-1: Illustration showing a microchip laser consisting of an erbium-doped sol-gel thin film applied to a microtoroid. Also shown is a fiber taper used for both pump coupling and laser emission extraction.

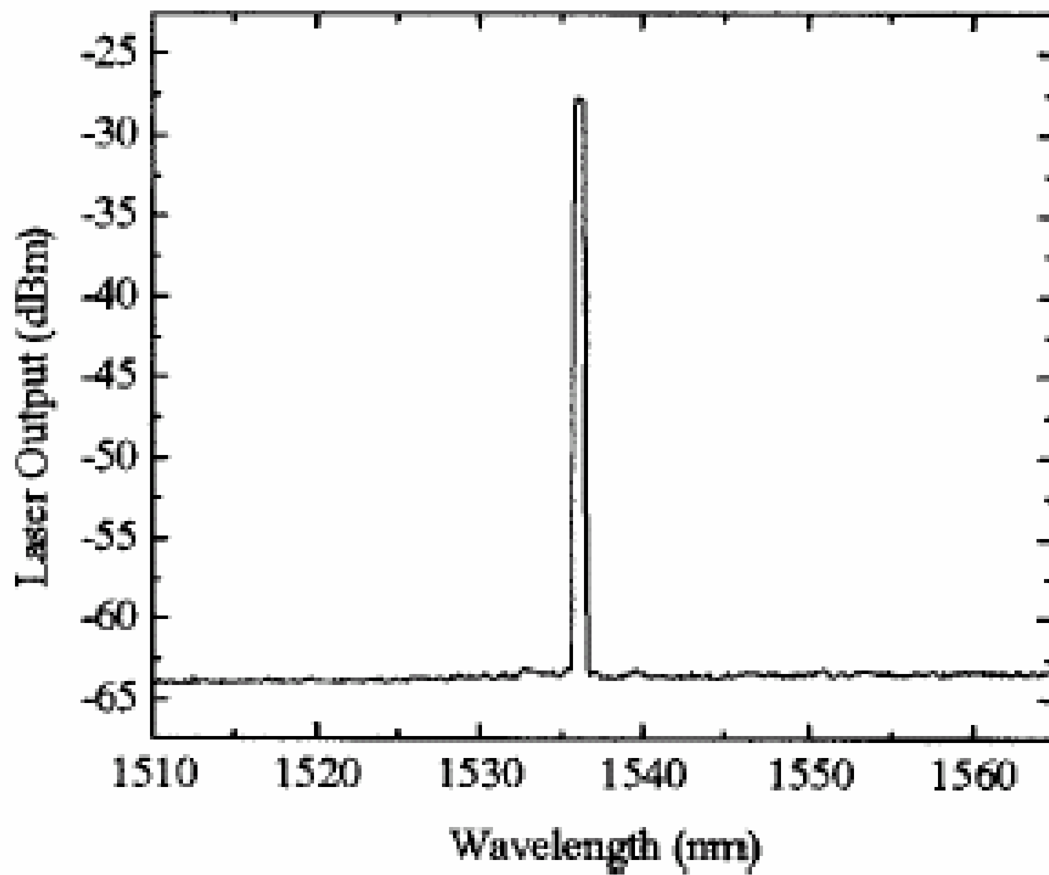

Figure 6-2: Emission spectrum of a microtoroid laser with approximate diameter of 80 μm.

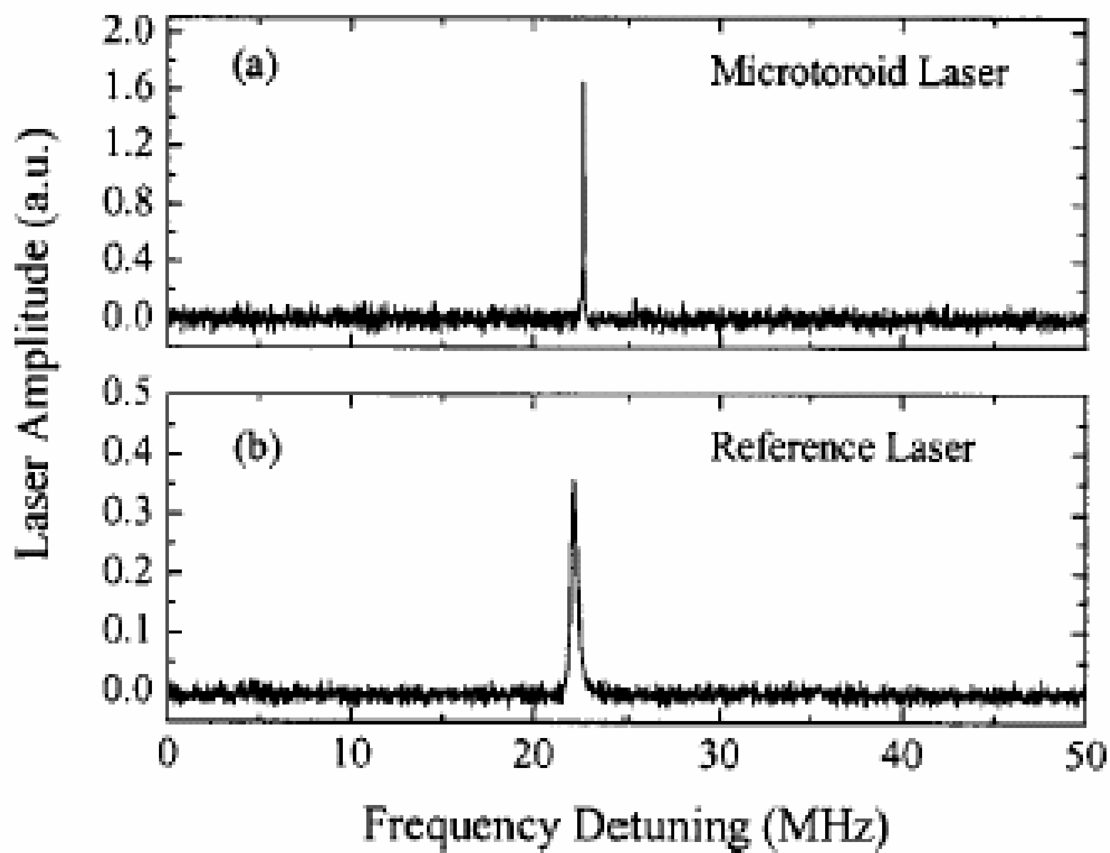

Figure 6-3: (a) Laser emission spectrum from Er-doped sol-gel thin-film coated microtoroid laser. (b) Reference laser emission spectrum from a 1550 nm single-mode laser with short-term linewidth of 300 kHz. Both spectra were measured using a high finesse scanning Fabry–Perot spectrometer.

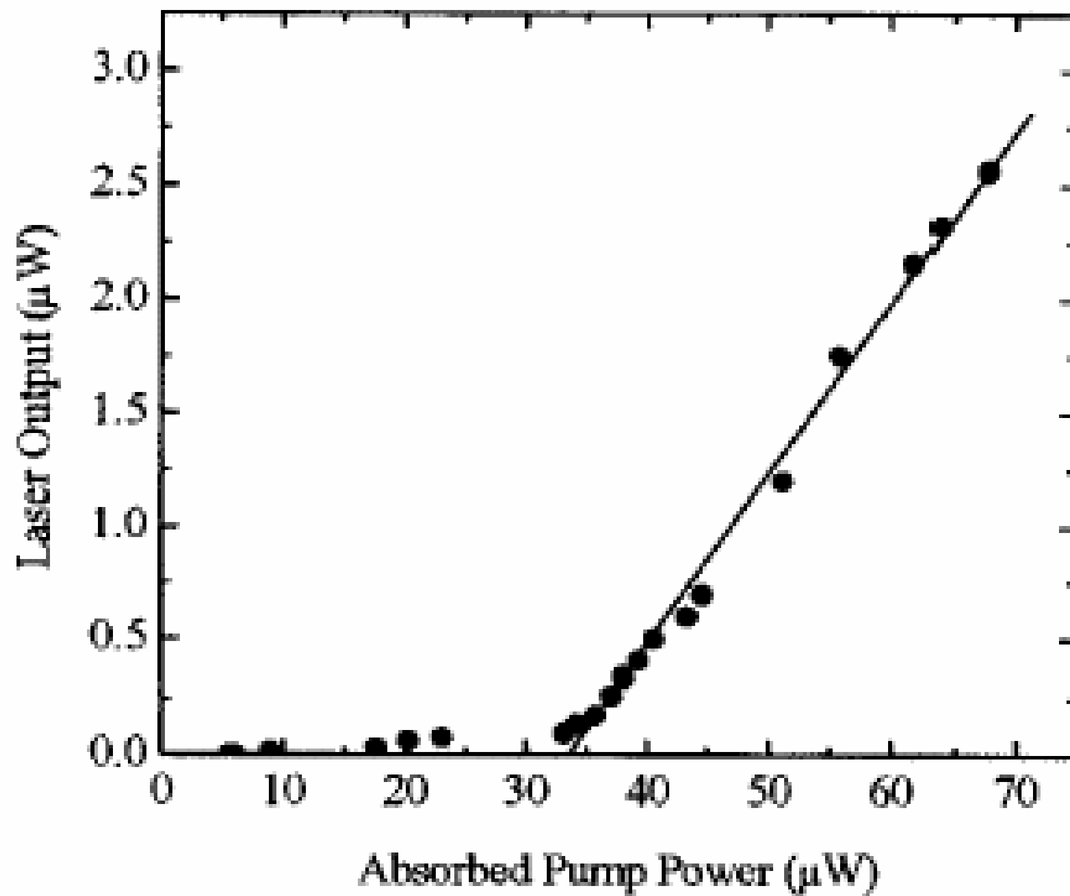

Figure 6-4: Measured laser output power plotted versus absorbed pump power for a microtoroid laser with a diameter of 80 µm.

Chapter 7 - Outlook

Based on the work described thus far in this thesis, it can be safely assumed that planar microtoroid resonators will continue to evolve additional functionality and thereby further applications. The primary motivation behind the continued development of the microtoroid devices lies firmly in the realm of providing the research community a "turn-key" device that can be plugged directly into their experiment so they may have immediate access to the UHQ domain. This would provide a truly enabling experimental tool previously limited to a handful of research groups worldwide that possessed the proper equipment. Moreover, there continues to be a migration in the scientific community towards integrating experiments onto a single chip, such as in the cases of Bose-Einstein condensate experiments[29] and more recently entire nuclear-magnetic-resonance (NMR) systems integrated on a single chip[66]. This movement has already started for biologists as they pursue more complex "labs on-a-chip", and there have already been recent demonstrations of the applications of high-Q microresonators in protein detection[8, 67] and DNA mutation detection[68]. As more experiments become integrated onto a single chip, the range of potential applications for UHQ planar microtoroids will continue to rise.

Bibliography

1. LefevreSeguin, V. and S. Haroche, *Towards cavity-QED experiments with silica microspheres.* Materials Science and Engineering B-Solid State Materials for Advanced Technology, 1997. **48**(1-2): p. 53-58.
2. Vernooy, D.W., et al., *Cavity QED with high-Q whispering gallery modes.* Physical Review A, 1998. **57**(4): p. R2293-R2296.
3. McCall, S.L., et al., *Whispering-Gallery Mode Microdisk Lasers.* Applied Physics Letters, 1992. **60**(3): p. 289-291.
4. Sandoghdar, V., et al., *Very low threshold whispering-gallery-mode microsphere laser.* Physical Review A, 1996. **54**(3): p. R1777-R1780.
5. Treussart, F., et al., *Evidence for intrinsic Kerr bistability of high-Q microsphere resonators in superfluid helium.* European Physical Journal D, 1998. **1**(3): p. 235-238.
6. Spillane, S.M., T.J. Kippenberg, and K.J. Vahala, *Ultralow-threshold Raman laser using a spherical dielectric microcavity.* Nature, 2002. **415**(6872): p. 621-623.
7. Chang, R.K., Campillo, A.J., *Optical Processes in Microcavities*. 1996, Singapore: World Scientific.
8. Vollmer, F., et al., *Protein detection by optical shift of a resonant microcavity.* Applied Physics Letters, 2002. **80**(21): p. 4057-4059.
9. Serpenguzel, A., S. Arnold, and G. Griffel, *Excitation of Resonances of Microspheres on an Optical-Fiber.* Optics Letters, 1995. **20**(7): p. 654-656.

10. Campillo, A.J., J.D. Eversole, and H.B. Lin, *Cavity Quantum Electrodynamic Enhancement Of Stimulated-Emission In Microdroplets.* Physical Review Letters, 1991. **67**(4): p. 437-440.

11. Braginsky, V.B., M.L. Gorodetsky, and V.S. Ilchenko, *Quality-Factor And Nonlinear Properties Of Optical Whispering-Gallery Modes.* Physics Letters A, 1989. **137**(7-8): p. 393-397.

12. Collot, L., et al., *Very High-Q Whispering-Gallery Mode Resonances Observed On Fused-Silica Microspheres.* Europhysics Letters, 1993. **23**(5): p. 327-334.

13. Vernooy, D.W., et al., *High-Q measurements of fused-silica microspheres in the near infrared.* Optics Letters, 1998. **23**(4): p. 247-249.

14. Himeno, A., K. Kato, and T. Miya, *Silica-based planar lightwave circuits.* Ieee Journal Of Selected Topics In Quantum Electronics, 1998. **4**(6): p. 913-924.

15. Michler, P., et al., *Laser emission from quantum dots in microdisk structures.* Applied Physics Letters, 2000. **77**(2): p. 184-186.

16. Adams, A.C., *Dielectric and Polysilicon Film Deposition*, in *VLSI Technology*, S.M. Sze, Editor. 1983, McGraw-Hill, Inc.: New York.

17. Chan, I.W.T., Brown, K. B., Lawson, R. P. W., Robinson, A. M., Ma, Y., Stembicke, D. *Gas Phase Etching of Silicon For MEMS With Xenon Difluoride*. in *IEEE Canadian Conference on Electrical and Computer Engineering*. 1999. Edmonton, Alberta, Canada: IEEE.

18. Winters, H.F., Coburn, J. W., *The etching of silicon with XeF2 vapor.* Applied Physics Letters, 1979. **34**(1): p. 70-73.

19. Seidel, H., Csepregi, L., Heuberger, A., Baumgartel, H., *Anisotropic Etching of Crystalline Silicon in Alkaline Solutions 1: Orientation Dependance and Behavior of Passivation Layers.* Journal of Electrochemical Society, 1990. **137**(11): p. 3612-3626.

20. Reisman, A., Berkenblit, M.,Chan, S. A., Kaufmann, F. B., Green, D. C., *The controlled etching of silicon in catalyzed ethylene-diamine-pyrochatechol-water solutions.* Journal of the Electrochemical Society: Solid State Science and Technology, 1979. **126** (8): p. 1406-1415.

21. Williams, K.R. and R.S. Muller, *Etch rates for micromachining processing.* Journal Of Microelectromechanical Systems, 1996. **5**(4): p. 256-269.

22. Delfino, M. and T.A. Reifsteck, *Laser Activated Flow Of Phosphosilicate Glass In Integrated-Circuit Devices.* Electron Device Letters, 1982. **3**(5): p. 116-118.

23. McLachlan, A.D. and F.P. Meyer, *Temperature-Dependence Of The Extinction Coefficient Of Fused-Silica For Co2-Laser Wavelengths.* Applied Optics, 1987. **26**(9): p. 1728-1731.

24. Sheikbahae, M. and H.S. Kwok, *Controlled Co2-Laser Melting Of Silicon.* Journal Of Applied Physics, 1988. **63**(2): p. 518-524.

25. Knight, J.C., et al., *Phase-matched excitation of whispering-gallery-mode resonances by a fiber taper.* Optics Letters, 1997. **22**(15): p. 1129-1131.

26. Cai, M., O. Painter, and K.J. Vahala, *Observation of critical coupling in a fiber taper to a silica-microsphere whispering-gallery mode system.* Physical Review Letters, 2000. **85**(1): p. 74-77.

27. Gayral, B., et al., *High-Q wet-etched GaAs microdisks containing InAs quantum boxes.* Applied Physics Letters, 1999. **75**(13): p. 1908-1910.

28. Kippenberg, T.J., S.M. Spillane, and K.J. Vahala, *Modal coupling in traveling-wave resonators.* Optics Letters, 2002. **27**(19): p. 1669-1671.

29. Hansel, W., et al., *Bose-Einstein condensation on a microelectronic chip.* Nature, 2001. **413**(6855): p. 498-501.

30. Vahala, K.J., *Optical microcavities.* Nature, 2003. **424**(6950): p. 839-846.

31. Chiba, A., et al., *Resonant frequency control of a microspherical cavity by temperature adjustment.* Japanese Journal Of Applied Physics Part 1-Regular Papers Short Notes & Review Papers, 2004. **43**(9A): p. 6138-6141.

32. Ilchenko, V.S., et al., *Strain-tunable high-Q optical microsphere resonator.* Optics Communications, 1998. **145**(1-6): p. 86-90.

33. Armani, D.K., et al., *Ultra-high-Q toroid microcavity on a chip.* Nature, 2003. **421**(6926): p. 925-928.

34. Spillane, S.M., et al., *Ideality in a fiber-taper-coupled microresonator system for application to cavity quantum electrodynamics.* Physical Review Letters, 2003. **91**(4).

35. Yang, L., D.K. Armani, and K.J. Vahala, *Fiber-coupled erbium microlasers on a chip.* Applied Physics Letters, 2003. **83**(5): p. 825-826.

36. Polman, A., et al., *Ultralow-threshold erbium-implanted toroidal microlaser on silicon.* Applied Physics Letters, 2004. **84**(7): p. 1037-1039.

37. Kippenberg, T.J., et al., *Ultralow-threshold microcavity Raman laser on a microelectronic chip.* Optics Letters, 2004. **29**(11): p. 1224-1226.

38. Rokhsari, H. and K.J. Vahala, *Ultralow loss, high Q, four port resonant couplers for quantum optics and photonics.* Physical Review Letters, 2004. **92**(25).

39. Poon, J.K.S., et al., *Matrix analysis of microring coupled-resonator optical waveguides.* Optics Express, 2004. **12**(1): p. 90-103.

40. Cui, Z. and R.A. Lawes, *A new sacrificial layer process for the fabrication of micromechanical systems.* Journal Of Micromechanics And Microengineering, 1997. **7**(3): p. 128-130.

41. Song, I.H. and P.K. Ajmera, *Use of a photoresist sacrificial layer with SU-8 electroplating mould in MEMS fabrication.* Journal Of Micromechanics And Microengineering, 2003. **13**(6): p. 816-821.

42. Engelmann, G., Ehrmann, O., Leutenbauer, R., Schmitz, H., Reichl, H., *Selectively released microstructures electroplated into thick positive photoresist.* Journal of Micromechanics and Microengineering, 1993. **3**: p. 152-154.

43. Sander, D., et al., *Fabrication Of Metallic Microstructures By Electroplating Using Deep-Etched Silicon Molds.* Journal Of Microelectromechanical Systems, 1995. **4**(2): p. 81-86.

44. Roth, S., et al., *High aspect ration UV photolithography for electroplated structures.* Journal Of Micromechanics And Microengineering, 1999. **9**(2): p. 105-108.

45. Leyendecker, K., et al., *New Microelectrodes For The Investigation Of The Electroforming Of Liga Microstructures.* Electrochimica Acta, 1994. **39**(8-9): p. 1139-1143.

46. Daniau, W., et al., *Fabrication of an electrostatic wobble micromotor using deep-etch UV lithography, nickel electroforming and a titanium sacrificial layer.* Journal Of Micromechanics And Microengineering, 1995. **5**(4): p. 270-275.

47. Fujita, T., K. Maenaka, and M. Maeda, *Design of two-dimensional micromachined gyroscope by using nickel electroplating.* Sensors And Actuators A-Physical, 1998. **66**(1-3): p. 173-177.

48. Pan, C.S. and W.Y. Hsu, *An electro-thermally and laterally driven polysilicon microactuator.* Journal Of Micromechanics And Microengineering, 1997. **7**(1): p. 7-13.

49. Syms, R.R.A., *Long-travel electrothermally driven resonant cantilever microactuators.* Journal Of Micromechanics And Microengineering, 2002. **12**(3): p. 211-218.

50. Kim, E., Y.N. Xia, and G.M. Whitesides, *Polymer Microstructures Formed By Molding In Capillaries.* Nature, 1995. **376**(6541): p. 581-584.

51. Folch, A., et al., *Molding of deep polydimethylsiloxane microstructures for microfluidics and biological applications.* Journal Of Biomechanical Engineering-Transactions Of The Asme, 1999. **121**(1): p. 28-34.

52. Thorsen, T., S.J. Maerkl, and S.R. Quake, *Microfluidic large-scale integration.* Science, 2002. **298**(5593): p. 580-584.

53. Splawn, B.G. and F.E. Lytle, *On-chip absorption measurements using an integrated waveguide.* Analytical And Bioanalytical Chemistry, 2002. **373**(7): p. 519-525.

54. Herlocker, J.A., et al., *Photorefractive polymer composites fabricated by injection molding.* Applied Physics Letters, 2002. **80**(7): p. 1156-1158.

55. Rabiei, P., et al., *Polymer micro-ring filters and modulators.* Journal Of Lightwave Technology, 2002. **20**(11): p. 1968-1975.

56. Bovin, R.J., *Dow Corning, Inc., Midland, Mich. (personal communication, 2003).*

57. Nakai, T., et al., *A siloxane polymer lightwave circuit on ceramic substrate applicable to ultrafast optoelectronic multi-chip-modules.* Optical And Quantum Electronics, 2001. **33**(7-10): p. 1113-1124.

58. Papra, A., et al., *Microfluidic networks made of poly(dimethylsiloxane), Si, and Au coated with polyethylene glycol for patterning proteins onto surfaces.* Langmuir, 2001. **17**(13): p. 4090-4095.

59. Chaudhury, M.K. and G.M. Whitesides, *Direct Measurement Of Interfacial Interactions Between Semispherical Lenses And Flat Sheets Of Poly(Dimethylsiloxane) And Their Chemical Derivatives.* Langmuir, 1991. **7**(5): p. 1013-1025.

60. Kippenberg, T.J., et al., *Fabrication and coupling to planar high-Q silica disk microcavities.* Applied Physics Letters, 2003. **83**(4): p. 797-799.

61. Lu, W., et al., *Use of ionic liquids for pi-conjugated polymer electrochemical devices.* Science, 2002. **297**(5583): p. 983-987.

62. Kaino, T., *Plastic Optical Fibers For Near-Infrared Transmission.* Applied Physics Letters, 1986. **48**(12): p. 757-758.

63. Huang, Y.Y., et al., *Soft lithography replication of polymeric microring optical resonators.* Optics Express, 2003. **11**(20): p. 2452-2458.

64. Yang, L. and K.J. Vahala, *Gain functionalization of silica microresonators.* Optics Letters, 2003. **28**(8): p. 592-594.

65. Zhai, J.W., L.Y. Zhang, and X. Yao, *The etched capacity for sol-gel derived silica-titania composited films.* Journal Of Inorganic Materials, 1999. **14**(1): p. 133-137.

66. Perlo, J., et al., *High-Resolution NMR Spectroscopy with a Portable Single-Sided Sensor.* Science, 2005: p. 1108944.

67. Arnold, S., et al., *Shift of whispering-gallery modes in microspheres by protein adsorption.* Optics Letters, 2003. **28**(4): p. 272-274.

68. Vollmer, F., et al., *Multiplexed DNA quanti. cation by spectroscopic shift of two microsphere cavities.* Biophysical Journal, 2003. **85**(3): p. 1974-1979.

Vita

EDUCATION

- California Institute of Technology-Pasadena, CA June 2005
  Ph.D. Electrical Engineering

- California Institute of Technology-Pasadena, CA June 2003
  M.S. Electrical Engineering (specializing in Microoptics and MEMS)

- University of Illinois at Urbana-Champaign May 2000
  B.S. Electrical Engineering (specializing in Microelectronics and MEMS)

WORK EXPERIENCE

- Graduate Research Assistant (Prof. Kerry Vahala, Caltech)
  October 2000-Present

- MEMS Process Engineer at Integrated Micromachines (Monrovia, CA)
  May-September 2000

- Undergraduate Research Assistant (Prof. Chang Liu, University of Illinois)
  February 1997-May 2000

- Summer Intern at Rockwell Scientific
  May-September 1997 and 1998

DOCTORAL RESEARCH

- "Ultra-high-Q toroid microcavity on a chip"
  D. K. Armani, T. J. Kippenberg, S. M. Spillane and K. J. Vahala
  Nature, vol. 421, pp. 925-929, 27 February 2003. ***(Cover Feature)***

  I was the first to demonstrate an optical microresonator on-a-chip with quality factors in excess of 100-million. Among the many applications of this device, we are currently developing sensitive air and liquid based chemical and biological sensors using this new technology.

PATENTS

- Ultra-high-Q toroid microcavity on a chip (PENDING)

- Replica-molded high-Q polymer microresonators (PENDING)

- Gain functionalization of silica microresonators (PENDING)

TECHNICAL BREADTH

- Worked on developing implantable drug delivery systems, fabricated using biodegradable polymers.
- Written software in C++, Java, and Pascal.
- Familiar with a wide variety of microelectronic fabrication tools, i.e., mask aligners, RIE etching systems, and CVD deposition systems.

PROFESSIONAL ACTIVITES

- Vice-Chairman of the Caltech Graduate Student Council
- Vice-President of the Caltech Astronomy Club
- President of the University of Illinois Turkish Student Association

AWARDS

- First Prize at "The Leading Edge Student Symposium" held as part of the 36th Annual Symposium of the Southern California Chapter of the American Vacuum Society
- Undergraduate Research Achievement Award from the University of Illinois, Department of Electrical Engineering and sponsored by SAIC

PERSONAL INFORMATION

- I am an avid amateur astronomer, dedicated salt-water aquarist, and fluent in Turkish and Armenian.

JOURNAL PUBLICATIONS

- "Microfabrication technology for polycaprolactone, a biodegradable polymer"
  D. K. Armani and C. Liu
  Journal of Micromechanics and Microengineering
  10 (1): 80-84 March 2000.
- "Ultra-high-Q toroid microcavity on a chip"
  D. K. Armani, T. J. Kippenberg, S. M. Spillane and K. J. Vahala
  Nature, Volume 421, 925-929, 27 February 2003. ***(Cover Feature)***
- "Fabrication and coupling to planar high-Q silica disk microcavities"
  T. J. Kippenberg, S. M. Spillane, D. K. Armani, and K. J. Vahala
  Applied Physics Letters, Volume 83, No. 4, 797-799, July 2003.
- "Fiber-coupled Erbium Microlasers on a chip"
  L. Yang, D. K. Armani and K. J. Vahala
  Applied Physics Letters, Volume 83, No. 5, 825-826, August 2003.

- "Replica-molded high-Q polymer microresonators"
  A. L. Martin, D. K. Armani, L. Yang and K. J. Vahala
  Optics Letters, Volume 29, Issue 6, 533-535, March 2004.

- "Ultralow-threshold microcavity Raman laser on a microeletronic chip"
  T. J. Kippenberg, S. M. Spillane, D. K. Armani, and K. J. Vahala
  Optics Letters, Volume 29, Issue 11, June 2004.

- "Electrical thermooptic tuning of ultra-high-Q microtoroid resonators"
  D. K. Armani, B. K. Min, A. L. Martin and K. J. Vahala
  Applied Physics Letters, Volume 85, No. 22, 5439-5441, November 2004.

CONFERENCES PUBLICATIONS

- "Re-configurable fluid circuits by PDMS elastomer micromachining."
  MEMS 99, Orlando, Florida
  D. K. Armani, N. Aluru, C. Liu

- "Microfabrication technology for polycaprolactone, a biodegradable polymer."
  MEMS 2000, Miyazaki, Japan
  D. K. Armani, C. Liu

- "Ultra-High-Q Microavities on-a-Chip: From Nonlinear Optics to Cavity QED"
  (Invited Talk) LEOS 2003, Tuscon, Arizona.
  K. J. Vahala, T. Kippenberg, D. Armani and S. M. Spillane,

- "Micromolding of High Q Toroid Resonators"
  LEOS 2003, Tuscon, Arizona
  A. L. Martin, L. Yang, D. Armani and K. J. Vahala

- "Low-threshold Erbium Fiber-coupled Microlaser on a Chip"
  Frontiers in Optics 2003, Tucson, Arizona
  L. Yang, D. K. Armani and K. J. Vahala

- "Ultra-high-Q toroid microcavities on a Chip" (Invited Talk)
  CLEO/QELS 2003, Baltimore, Maryland
  T. J. Kippenberg, D. K. Armani, S. M. Spillane and K. J. Vahala

- "Ultra-low threshold monolithic micro-Raman laser"
  CLEO/QELS 2003, Baltimore, Maryland
  S. M. Spillane, D. K. Armani, T. J. Kippenberg and K. J. Vahala

- "Micro-molded high-Q polymer resonators for optical loss determination"
  MRS 2005, San Francisco, CA
  A. L. Martin, A. Srinivasan, D. K. Armani, B. Min, K. J. Vahala